Joint-instrument analyses with Gammapy

Master's Thesis in Physics

Presented by

Tim Unbehaun

Date: 03. December 2020

Erlangen Centre for Astroparticle Physics
Friedrich-Alexander-Universität
Erlangen-Nürnberg

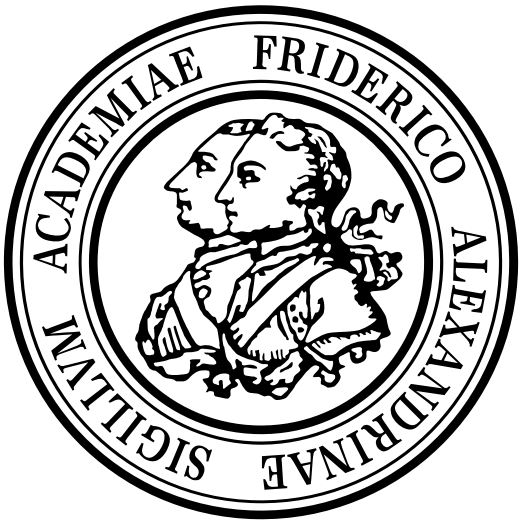

Supervisor: Prof. Dr. Stefan Funk
Co-advisor: Prof. Dr. Christopher van Eldik

Contents

> Space is big. Really big. You won't believe how hugely mindboggling big it really is.
>
> *(Douglas Adams, "The Hitchhiker's Guide to the Galaxy")*

1. Introduction

For as long as there are ancient recordings, humankind tried to figure out the true nature of stars, the Sun and the moon in more or less scientific ways. Until rather recently only the visible light could be used to gather information on stellar objects, some more nearby and others very far away from the Earth. The mystery how stars generate their energy and light was only solved after Albert Einstein's theory of general relativity [Einstein, 1916] helped us to understand gravity and stellar motions in a more fundamental way and after Quantum mechanics were on its way. The young astronomer Cecilia Payne-Gaposchkin found evidence for the high abundance of Hydrogen and Helium in the spectral absorption lines of stars in 1925. In her PhD thesis [Payne, 1925] she classified the results as "almost certainly not real" because they were in contradiction to the current scientific consensus that stars are made of the same materials as the Earth. Her results were confirmed a few years later by Arthur Stanley Eddington leading to the model of nuclear fusion powering the stars. Today stellar physics is able to describe most of the phenomena connected to stars very well. But stars are not the only interesting objects in space and visible light is not the only messenger we can use to learn about them. Various telescopes and observatories have helped to detect light ranging from radio waves to γ-rays coming from rather exotic object classes hosting extreme conditions. Like this we have discovered QUASARs and BLAZARs shining as bright as whole galaxies and Super Novas and Gamma Ray Bursts with enormous explosion energies and many more. Even though we have some ideas how some of these sources are able to accelerate charged particles up to energies in the order of 10^{21} eV [Becker, 2008], there are a lot of open questions, e.g. which kind of charged particles are dominantly accelerated for each source class and which spectral shape do they follow. Until now most analyses on these sources are based on observations by one telescope or detector only considering the energy range or particle type accessible to it. Like this great progress has been made in detecting and characterizing thousands of (extra-)galactic particle accelerators. In order to learn even more about them the next step is to take the whole picture into consideration and to combine the measurements of different instruments. Even though combined analyses of different instruments have been performed before e.g. by taking published flux points of a source in different energy ranges, it seems much more promising to combine the lower level data of the instruments. In this way one can simultaneously fit the spatial morphology and the spectral shape of one source seen by multiple different instruments and calculate the correlation between the free parameters. One can also directly fit physical models predicting γ-ray and neutrino fluxes to the data of the respective instruments and link the physically connected parameters. This is especially interesting because both γ-rays and neutrinos can be produced by the same hadronic interactions at the source leading to a multi-messenger connection. This would mean that if one source is accelerating e.g. protons and other hadronic particles and the γ-ray emission is caused by these particles one would also

expect a flux of neutrinos coming from that source. Even though the neutrino telescope IceCube has successfully measured a diffuse galactic neutrino flux, until now only one neutrino event could be associated with one individual source at the 3σ level. This event had a most likely energy of 290 TeV and was detected in coincidence with a flaring BLAZAR in September 2017 [Williams, 2019]. In order to exploit the multi-messenger connection in such combined analyses one would need publicly available data of the instruments which will be the case for the currently in building phase Cherenkov Telescope Array (CTA) and the next generation neutrino detector KM3NeT. One also needs a suitable software package able to read and analyse data from both instruments which are also currently in development. One example is Gammapy which is an open-source Python package designed for gamma-ray astronomy but also able to analyse data from different instruments (e.g. neutrino data) once the instrument data is available.
In the first part of this thesis a combined analysis of CTA and KM3NeT data with Gammapy will be simulated and constraints on the production mechanisms for leptonic and hadronic emission scenarios will be calculated. While CTA will measure γ-rays in an energy range from 20 GeV up to over 100 TeV, KM3NeT will be sensitive to neutrinos in a range from 100 GeV up to 100 PeV. With its location on the northern Hemisphere it can observe a large fraction of the galactic disc including many interesting galactic sources. This kind of analysis might help in the future to improve the understanding of certain galactic γ-ray sources regarding their acceleration mechanisms.
The second part of this work will be about a combined analysis of H.E.S.S. and *Fermi* LAT data on the Crab nebula also using Gammapy. *Fermi* is a space based γ-ray telescope with an energy range of $\sim$20 MeV to $\sim$1 TeV and H.E.S.S. is a ground based Imaging Air Cherenkov Telescope measuring γ-rays in a range from $\sim$50 GeV to 100 TeV. Both instruments have observed the Crab nebula which is the brightest, steady TeV γ-ray source. It is very well studied and the perfect candidate to test a combined analysis of different instrument data using Gammapy. The goal here is to compare the Gammapy analyses of H.E.S.S. and *Fermi* data to the analyses performed with standard analysis tools and to check for consistency. Once this is ensured the combination of the data will extend the energy ranges of the individual instruments and a physically motivated model can be fitted to the data. Furthermore it is interesting to determine the Crab's extension in different energy bands. It would be the first time that this is done in a consistent way over this extended energy range measured by different instruments.

> We have already discovered the basic laws that govern matter and understand all the normal situations. We don't know how the laws fit together, and what happens under extreme conditions.
>
> *(Stephen W. Hawking)*

2. Studying particle acceleration with high energy γ-rays and neutrinos

This section will give an overview of the connection between high energy γ-rays and neutrinos and their production mechanisms at astrophysical sources. The energies of these particles exceed the energies accessible in particle accelerators at Earth by far. By observing these sources and learning about production and acceleration mechanisms we can test physical models in the limit of very high energies and extreme conditions.

2.1 Multi messenger connection

The Earth is exposed to a continuous flux of charged particles from space, called cosmic rays (CR), in a wide range of energies. This was already discovered by Viktor Hess in 1912 with his balloon flights [Hess, 1912]. He could show that the abundance of ionizing particles increases with increasing distance to the ground, indicating that the flux was not coming from radioactive solids in the ground. Today we believe that galactic and extra-galactic sources are accelerating charged particles to very high energies (up to $\sim 10^{21}$ eV) [Becker (2008, chapter 3.1.1.1)]. Known acceleration mechanism are e.g. the *one-shot acceleration* where a particle gains energy in a continuous way from an ordered field or the *Fermi shock acceleration*. Here particles gain their energy successively when passing a shock front over and over again while being confined in the shock region by magnetic fields (for more detail see e.g. Bustamante et al. (2010)). The CR spectrum measured at Earth is shown in figure 1 (left) and follows a steep power-law. It consists mostly of protons ($\sim$90%) and heavier nuclei where the exact composition is energy dependent. Electrons and positrons only make up for about 1% of the cosmic rays. If we want to learn more about the acceleration mechanisms inside one particular source one cannot simply measure the CR spectrum from the source's direction since charged particles are deflected by the galactic magnetic fields, so they do not point back. This is at least the case for CR with energies $E_{\mathrm{CR}} < Z \cdot 10^{17}$ eV. Above this energy the flux of CR is very low due to its steep power-law spectrum so it is difficult to gather enough statistics on these very high energy events from one source. An alternative way to study (extra-)galactic particle accelerators is to look at neutral particles emitted by them. Even though neutral particles cannot be accelerated directly by electric fields or the Fermi acceleration mechanisms, they are produced in particle interactions of high energy CR in the source's vicinity. Dependent on the kind of the interaction (hadronic or leptonic) high energy neutrinos and/or high energy photons are produced. These neutral particles point back to their sources and by measuring their spectrum we can draw conclusions on the primary particle population. The spectrum of the messenger particles measured at Earth can be seen in figure 1 right.

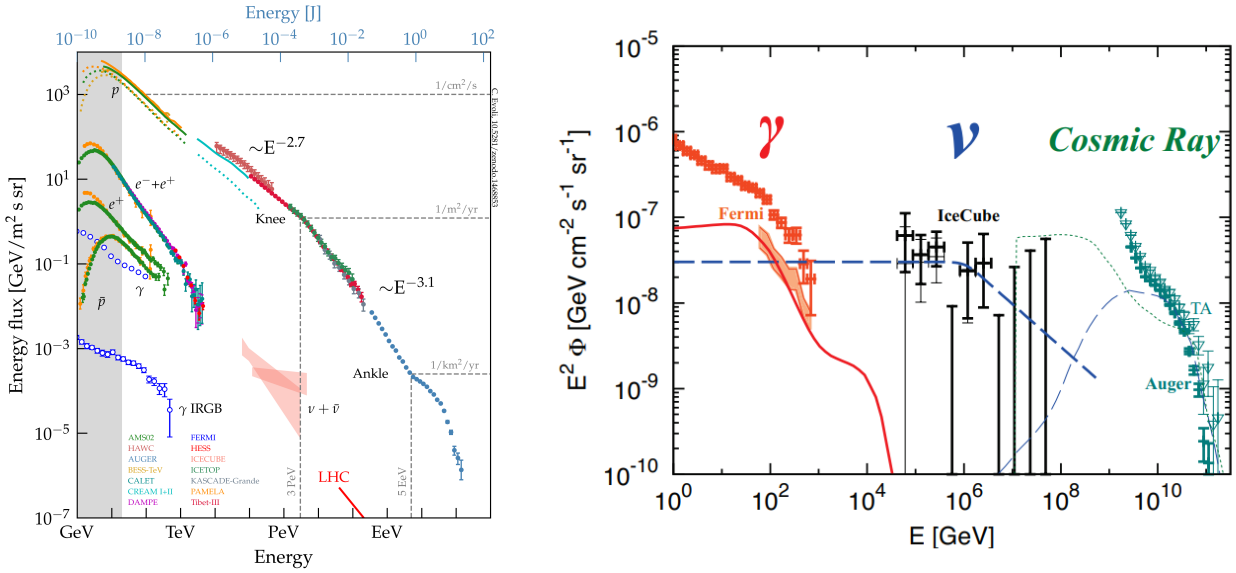

Figure 1: *Left:* Cosmic ray spectrum measured by different experiments (see legend). Also shown is the composition of the spectrum for the lower energies [Evoli, 2018]. *Right:* Spectrum of the multi-messenger particles. The diffuse γ-ray background measured by *Fermi* (red) is compared to the neutrino flux measured with IceCube (black) and the cosmic ray flux (green) measured with the Pierre Auger observatory [Murase and Waxman, 2016].

2.1.1 Leptonic interactions

Typical sources that produce their γ-ray emission to a large extent in leptonic interactions are pulsars and pulsar wind nebulae. Those sources accelerate electrons and positrons to very high energies. These can than emit Synchrotron radiation in possibly present magnetic fields and thus produce γ-rays up to a theoretical maximal energy of $E_\gamma = \kappa \cdot 68\,\mathrm{MeV}$ with $\kappa = 1-3$ [Aharonian et al., 2004]. So the Synchrotron component is not responsible for the high energy γ-rays above 1 GeV. These can be produced when the very high energy e^-/e^+ directly transfer their energy to low energy photons present in so-called *seed photon fields* through the Inverse Compton scattering process (IC). The seed photon fields can be the *Cosmic Microwave Background* (CMB), far-infrared dust emission (FIR), near-infrared stellar emission (NIR) or the Synchrotron photon field (SSC) produced by the same electrons/positrons. The characteristic shape of the Synchrotron and Inverse Compton flux resulting from an electron spectrum can be seen in figure 2 (Top). In contrast to hadronic interactions there are no neutrinos produced in leptonic interactions.

2.1.2 Hadronic interactions

Typical sources which might feature a hadronic γ-ray production are Super Novas and their remnants or Active Galactic Nuclei. In hadronic interaction both photons and neutrinos can be produced. The conventional models consider high energy protons interacting with low energy protons or matter fields in or around the acceleration region. In these interactions π^+, π^-, π^0 are produced with about equal abundances (as well as other interaction products). The neutral pions decay mostly into two photons while the charged ones decay into leptons and their corresponding neutrino

$$\pi^0 \longrightarrow \gamma + \gamma \tag{2.1}$$

$$\pi^\pm \longrightarrow \mu^\pm + \overset{(-)}{\nu}_\mu \longrightarrow e^\pm + \nu_\mu + \bar{\nu}_\mu + \overset{(-)}{\nu}_e \tag{2.2}$$

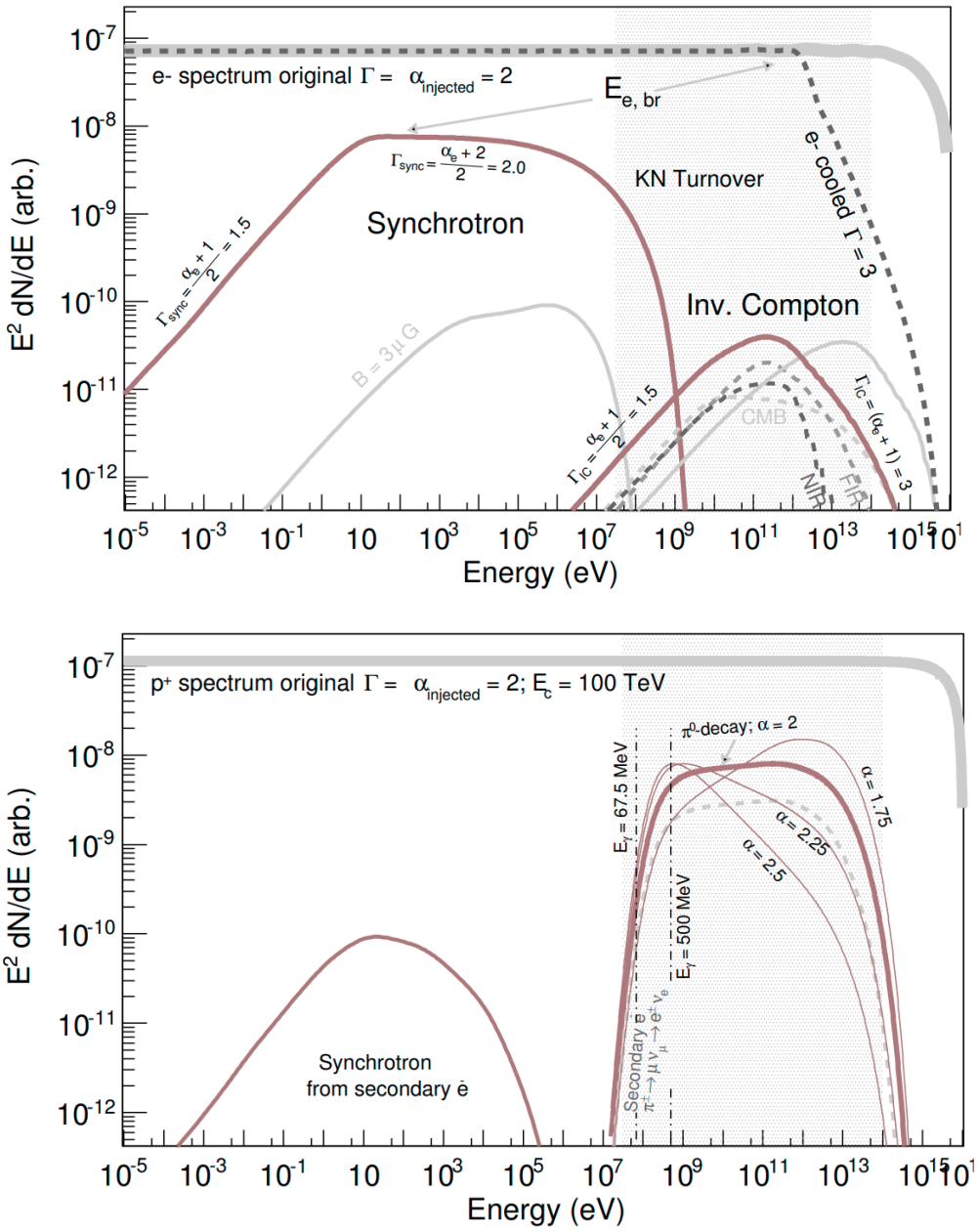

Figure 2: *Top:* Spectral energy distribution of an electron spectrum (light gray) and the resulting Synchrotron and Inverse Compton flux (brown). *Bottom:* Spectral energy distribution of a proton spectrum (light gray) and the resulting γ-ray spectrum from Pion Decay (brown) [Funk, 2015].

For the charged pion decay the electron channel is strongly suppressed because of helicity conservation. In figure 3 the Feynman diagrams for these interactions are shown. The average energy transferred to one pion in a pp-interaction is about $0.2 \cdot E_p$ and is rather independent on the protons energy. The four leptons resulting from a $\pi^{\pm}$ decay will approximately carry the same amount of energy, which means that the neutrinos produced in pp-interactions have an energy $E_\nu \approx E_p/20$ [Becker, 2008]. Similar the two γ-rays will have an energy of $E_\gamma \approx E_p/10$. This means that the shape of the neutrino and γ-ray spectrum is close to the proton spectrum which is just shifted in energy, at least well above the mass scale of the π^0 of 135 MeV. The γ-ray emission from an exemplary proton spectrum can be seen in figure 2 (bottom).

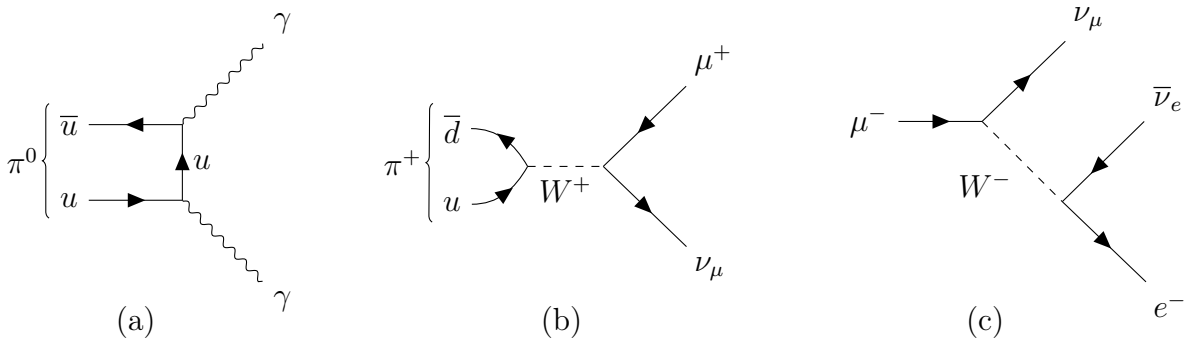

Figure 3: Feynman diagrams of the neutral pion decay (a), the charged pion decay on the example of the π^+ (b) and the muon decay (c).

If we don't distinguish between neutrinos and anit-neutrinos[1] the ratio of $(\nu_e : \nu_\mu : \nu_\tau)$ for pion decay is $(1 : 2 : 0)$ according to equation 2.2. Due to neutrino oscillation the expected ratio at Earth is $(1 : 1 : 1)$ when the source is outside the solar system [Becker, 2008].

2.2 Relevant galactic sources

In the following an overview of the three relevant sources analysed or simulated in the thesis is given: RX J1713.7−3946, Vela X and the Crab nebula.

2.2.1 The Crab nebula

The Crab nebula is the brightest steady source of TeV γ-rays. In 1054 Chinese astronomers reported a bright explosion event not knowing that it corresponded to a core-collapse supernova in the constellation of Taurus about 2 kpc away from Earth. After the supernova a fast rotating neutron star was left behind which powers an outflow of highly relativistic particles with its rotational energy losses. Today's best models assume that this outflow consists of mostly electrons and positrons which get further accelerated in the *termination shock* about 0.5 light years (ly) away from the pulsar. These electrons/positrons can reach energies up to 10^{15} eV filling the area of about 10 ly in diameter after the *termination shock*. They emit Synchrotron radiation in the ambient magnetic fields, producing the low energy part of the spectrum in figure 4 up to ∼1 GeV. The high energy part of the spectrum is produced by Inverse Compton up-scattering of low energy photons by the same electrons/positrons [Abdalla et al., 2019]. This whole system is now called the Crab pulsar wind nebula (PWN) with its morphology (in X-rays) shown in figure 4 (right panel) with the bright pulsar in the center followed by the *termination shock* and the region of non-thermal particle wind.
Detailed multi-wavelength analyses of the spectrum have been performed e.g. by Yuan et al. (2011) and Meyer et al. (2010) fitting a physical model to the electromagnetic emission of the Crab nebula. These studies show that the emission from radio energies up to γ-ray energies can be reasonable well described by the model. There is also a strong evidence for an energy dependent extension of the Crab nebula at γ-ray energies. Fitting the extension in several energy bands which was done by Yeung and Horns (2019) shows that the extension decreases towards higher energies. Since the γ-rays from different energy bands can be associated with primary electrons of different energies, it means that we can learn about the propagation of very high energy (VHE) electrons in the Crab's vicinity.

[1] neutrino detectors like KM3NeT cannot do this

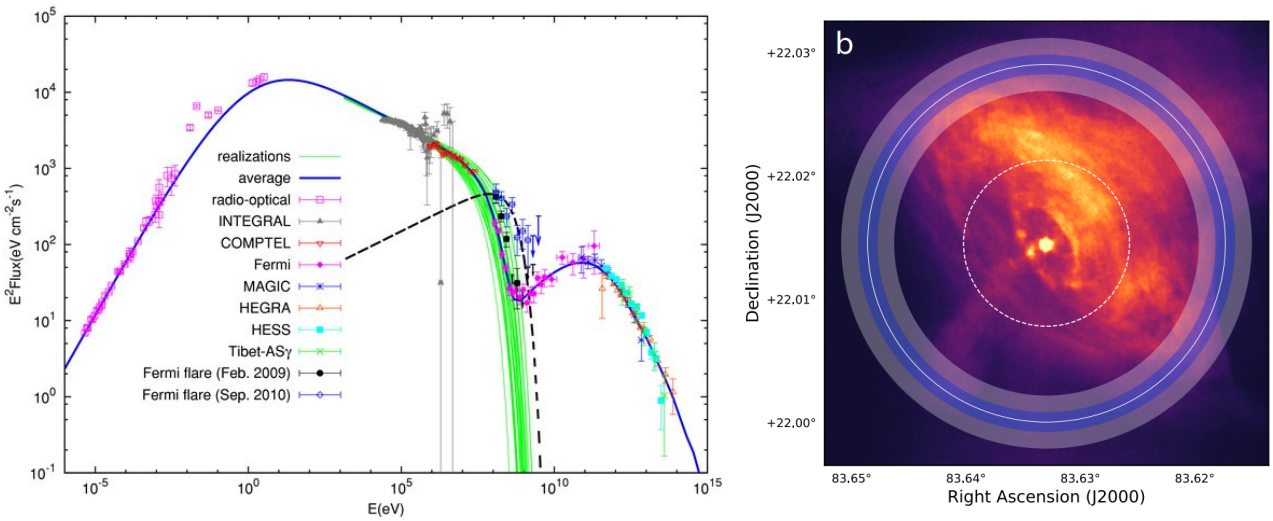

Figure 4: *Left:* Spectral energy distribution of the Crab nebula from radio waves to γ-rays. The lines show fits to the data points measured by the instruments listed in the legend. For details see Yuan et al. (2011). *Right: Chandra* X-ray image (courtesy of M. C. Weisskopf and J. J. Kolodziejczak). The H.E.S.S. extension is shown as solid white circle overlaid on top of shaded annuli indicating the statistical and systematic uncertainties. The *Chandra* extension, corresponding to 39% of the X-ray photons, is given as dashed white circle. Taken from Abdalla et al. (2019).

2.2.2 Vela X

Vela X is one of the nearest pulsar wind nebulae at a distance of about 0.29 kpc [Abramowski et al., 2012] and is associated with the energetic Vela pulsar PSR B0833-45. Similar to the Crab nebula most models assume a leptonic generation of the VHE γ-rays. None the less it is not clear to what extent also protons contribute to the total γ-ray flux from Vela X. In order to put strong constraints of the hadronic fraction it might be helpful to look for (the lack of) neutrinos coming from that source.

2.2.3 RX J1713.7−3946

RX J1713.7−3946 is a young shell-type Super Nova Remnant (SNR) which is located at a distance of about 1 kpc. In its shock front charged particles are accelerated to very high energies which also cause γ-ray emission that we can observe at Earth. The origin of the γ-ray emission extending up to about 100 TeV is still unclear. In the latest H.E.S.S. paper [Abdalla et al., 2018] on RX J1713.7−3946 both leptonic and hadronic models have been fitted to the combination of H.E.S.S. and *Fermi* LAT data where neither model could be accepted unambiguously. However molecular clouds in the vicinity of the source could be an indication for a hadronic production mechanism.

An experiment is a question which science poses to Nature, and a measurement is the recording of Nature's answer

(Max Planck, "The Meaning and Limits of Exact Science")

3. Instruments

The following section gives an overview of the four relevant instruments in this thesis. Beginning with the ground-based Imaging Air Cherenkov telescopes (IACTs) H.E.S.S. and CTA which can detect γ-rays between $\sim$50 GeV and 100 TeV. The lower energy γ-rays in a range from $\sim$20 MeV to $\sim$1 TeV can be detected with the *Fermi* satellite. The currently in building phase next level neutrino detector KM3NeT will be able to detect neutrinos in an energy range from 100 GeV up to 100 PeV.

3.1 Imaging Air Cherenkov Telescopes

IACTs collect the Cherenkov light of particle showers. These air showers are produced by high energy primary particles (γ-rays or CR) when they enter the Earth's atmosphere at an altitude of about 20 km. There are electromagnetic cascades (fig. 5a) consisting of electrons, positrons and γ-rays. The dominant processes are pair production and Bremsstrahlung which happen consecutively until the secondary particles are below a critical energy. The number of secondary particles is proportional to the energy of the primary particle and the altitude of the shower maximum depends logarithmically on the energy of the primary γ-ray ($\sim$10 km AMSL for $E_\gamma = 1$ TeV) [Funk, 2015]. The opening angles of the leptonic interactions are small (typically $< 1°$) and the Molière Radius (radius that contains 90% of the particles) is around 90 m.
There are also hadronic showers induced by protons or heavier nuclei (fig. 5b). In these showers Mesons like pions are produced in hadronic interactions which then decay into two γ-rays or muons and muon neutrinos. The γ-rays or the electrons from the muon decay then produce electromagnetic sub-showers. The hadronic interactions give proton showers larger transverse momentum and make them more irregular. The difference in shape and composition compared to electromagnetic showers can be used to suppress the hadronic background which dominates the γ-ray signal by a factor of up to 10^4.
The Cherenkov light cones are produced when charged particles travel through a dielectric medium faster than the speed of light in that medium. The medium is electrically polarized along the track and is emitting electromagnetic waves that do not interact destructively as it would be the case for slower particles. Figure 5c shows the Cherenkov light pool with an diameter of about 240 m at the ground. However for a typical shower there are only $\sim$100 photons per m^2 and TeV arriving at the ground in good atmospheric conditions [Funk, 2015]. Even though these Cherenkov light flashes are very faint they can still be detected over the night sky background light by high time resolution cameras. Almost all of the Cherenkov photons arrive at the ground within a few nanoseconds, a very short time frame in which only few background photons arrive. The cameras consist of an array of Photo multipliers

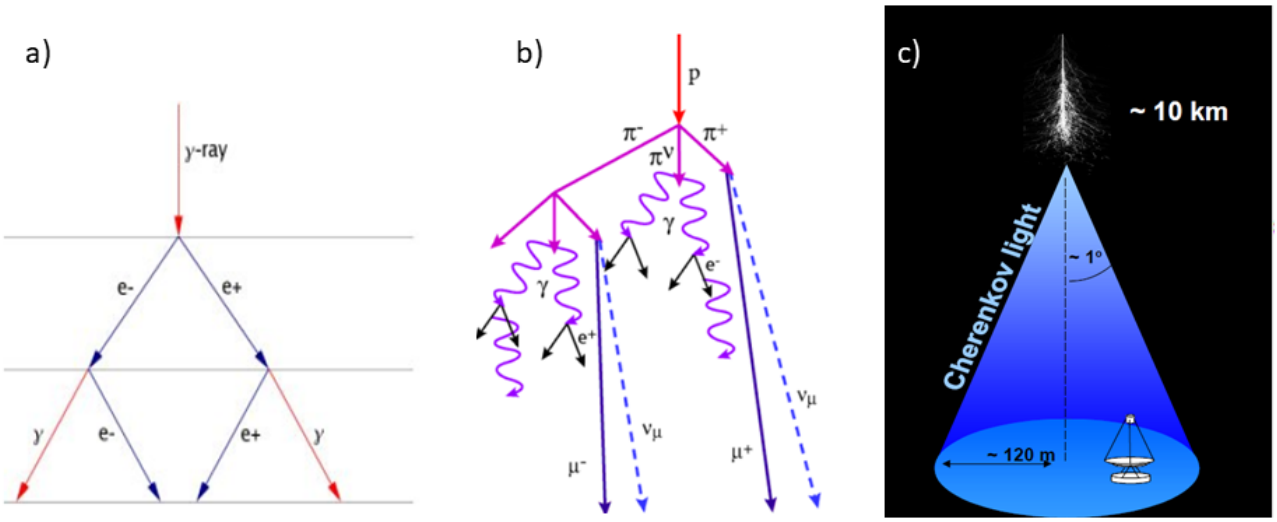

Figure 5: Illustration of **a)** Electromagnetic cascade with pair production and Bremsstrahlung, **b)** Hadronic air shower induced by a proton with electromagnetic sub-showers, **c)** Air shower with the resulting Cherenkov light cone (images from a presentation by Daniela Dorner, 2019).

(PMTs) each representing one pixel. When multiple PMTs surpass a threshold an image of the shower is recorded. With a reconstruction algorithm the energy, direction and shower type can be determined. The reconstruction improves when using a stereoscopic system with multiple telescopes looking at the same shower. This is done in the H.E.S.S. experiment and will also be used in the Cherenkov Telescope Array (CTA).
The advantage of this method is that the big area of the atmosphere can be used to detect the low γ-ray fluxes in the TeV range. The draw back is that IACTs can only operate in dark, moonless nights without clouds. Furthermore since the atmosphere is part of the detector it can not be calibrated directly, instead Monte Carlo simulations are used for that.

3.1.1 H.E.S.S.

The **H**igh **E**nergy **S**tereoscopic **S**ystem (H.E.S.S.)[2] is located in Namibia, near the Gamsberg mountain at an altitude of 1800 m (compare figure 6). Phase I consists of 4 telescopes each with 108 m^2 mirror area positioned at the corners of a square with 120 m side length. All four telescopes were operational in December 2003. In Phase II a bigger telescope with 614 m^2 mirror area was added in the center of the array to improve the angular resolution and measure to even lower energies. It started operation in July 2012. In 2016 the cameras and light collimators of the original HESS-I array have been exchanged. Observations with the new cameras belong to the so-called HESS-IU season.

3.1.2 CTA

The **C**herenkov **T**elescope **A**rray[3] will be the next generation IACT. It will consist of two sites, one at the northern hemisphere in La Palma and one at the southern hemisphere in Chile. Together both sites will have more than 100 telescopes in three different sizes (compare figure 7). There are 70 Small-Sized Telescopes (SSTs) planned with an mirror area of 8 m^2 and 10.5° field of view measuring energies from a few TeV up to 300 TeV. All of the SSTs will be located at the southern observatory. The Medium-Sized Telescopes (MSTs) will be built in different versions.

[2] https://www.mpi-hd.mpg.de/hfm/HESS/
[3] https://www.cta-observatory.org

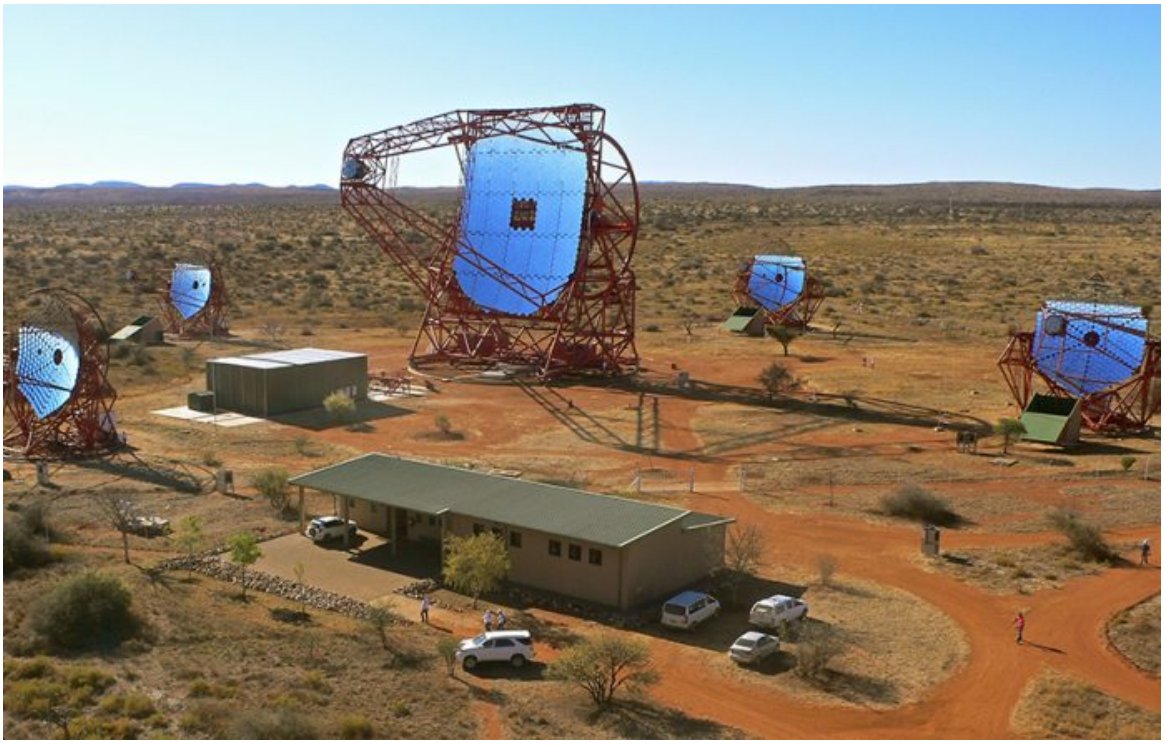

Figure 6: Photo of the five H.E.S.S. telescopes. Credit: H.E.S.S. collaboration.

One will use a modified Davies-Cotton optical design and use FlashCam and NectarCam[4] based on PMTs. The effective mirror area is 88 m^2 and the pixel size corresponds to 0.17°. The alternative version uses the dual mirrored Schwarzschild-Couder optical design for better light focus and imaging details. It only uses 41 m^2 of effective mirror area and its camera based on silicon photo multipliers with >11 000 pixel (0.067° pixel size) is designed to improve the shower reconstruction. Fifteen of the MSTs will be located at the northern observatory and 25 at the southern. Each site will also have four Large-Sized Telescopes (LSTs) with parabolic optical design and 370 m^2 of effective mirror area to measure γ-rays down to 20 GeV. CTA is expected to be ten times more sensitive than existing experiments and offer better angular and energy reconstruction of the events. The measured data will be publicly available which makes combined analyses with other instruments possible. The beginning of the observatory observations is planned for 2022 and the construction project should be completed in 2025.

3.2 *Fermi*

The *Fermi Gamma-ray Space Telescope*[5] was launched on June 11, 2008 by NASA. The satellite is hosting two instruments as can be seen in figure 8 *left*: The Large Area Telescope (LAT) and the Gamma-ray Burst Monitor (GBM), where only the LAT is relevant for this work. The LAT is a pair-conversion telescope with a precision converter-tracker and calorimeter. Since high energy γ-rays cannot be deflected or refracted the detection principle of the LAT is based on the e^+/e^- pair production when γ-rays interact with the satellite. The converter-tracker consists of 16 planes of high-Z material (wolfram) offering an increased cross section for the pair production. The direction of the charged particles is measured with position-sensitive detectors. The calorimeter serves two purposes. First measuring the energy of the particle shower induced by the γ-ray and second imaging the shower development profile which can be used as a background discriminator [Atwood et al., 2009]. Each calorimeter module consists of

[4] https://www.cta-observatory.org/project/technology/mst/
[5] https://fermi.gsfc.nasa.gov/

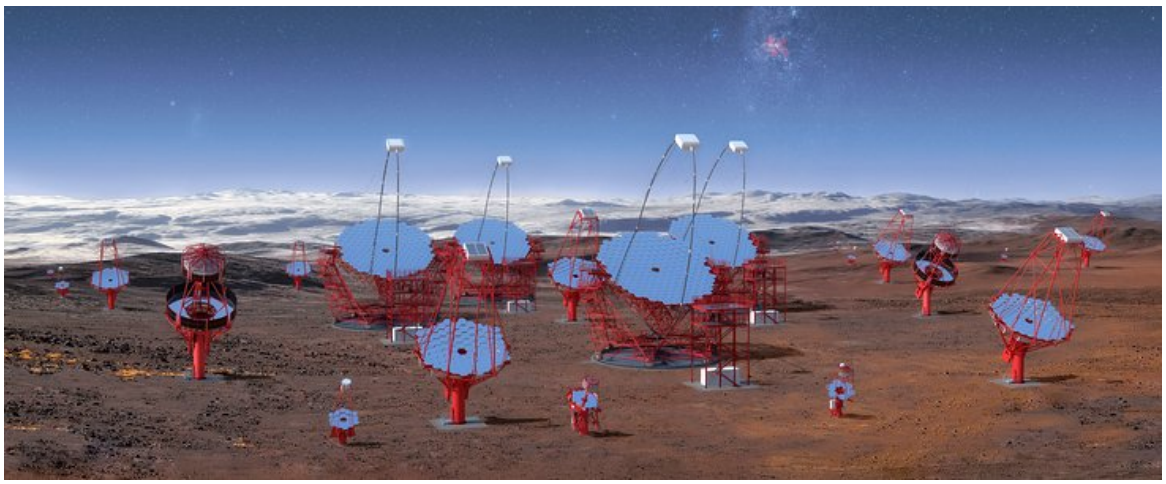

Figure 7: All three telescope classes planned for the southern CTA observatory. Credit: CTA/M-A. Besel/IAC (G.P. Diaz)/ESO

96 CsI(Tl) crystals optically isolated from each other. Furthermore the anticoincidence detector provides charged particle background rejection. There are 89 scintillation plates surrounding the converter-tracker which detect incoming charged particles with an efficiency of 0.9997 averaged over the detector volume. The LAT detector could be calibrated before the launch offering an energy resolution $\Delta E/E$ of +5% - 10%. The angular resolution improves from 3.5° at 100 MeV to $\leq$0.15° at $\geq$ 10 GeV. Figure 8 *right* shows the all-sky map recorded with the LAT. The source catalog 4FGL-DR2 contains 5788 entries and is based on 10 years of LAT observation [Abdollahi et al., 2020]. Since the γ-ray flux is following a steep power-law for most sources the detection area of *Fermi* LAT is not big enough to gather enough statistics above ~300 GeV. It is also not affordable to send larger instruments into space, that is why ground-based detectors are used for the higher energies.

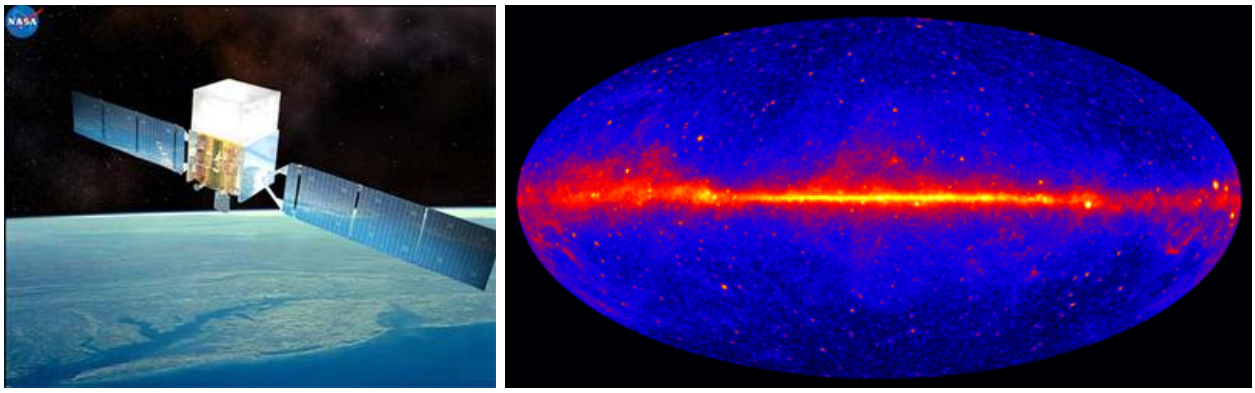

Figure 8: *Left:* An artist's drawing of the *Fermi*-satellite orbiting Earth. The LAT can be seen on top of the GBM (Credits: NASA E/PO, Sonoma State University, Aurore Simonnet). *Right:* Gamma-ray all-sky map for energies greater than 1 GeV based on 5 years of LAT observation (Credit: NASA/DOE/Fermi LAT Collaboration).

3.3 KM3NeT

The IceCube neutrino observatory[6] is detecting high energy neutrinos in the antarctic ice since 2010. It could measure a diffuse astrophysical neutrino flux but only very few neutrinos could

[6] https://icecube.wisc.edu/

be assigned to individual sources, none of them in our galaxy [Williams, 2019]. Because of its location on the south pole it can only observe a limited fraction of the galactic sources through the Earth which is an important filter for the atmospheric muon background.
KM3NeT[7] is a project for the next generation neutrino telescopes located in the Mediterranean Sea. The ARCA (short for Astroparticle Research with Cosmics in the Abyss) telescope will look for neutrinos from distant astrophysical sources such as supernovae, gamma ray bursters or colliding stars. The ORCA telescope will be used to study neutrino properties exploiting neutrinos generated in the Earth's atmosphere. ARCA will be mapping 87% of the sky including most of the galaxy and the galactic center. Because of its location on the northern hemisphere (36°16' N 16°06' E) sources on the southern hemisphere can be observed through the Earth filtering the atmospheric muon background. ARCA phase 2.0 will consist of two detector blocks, each made of 115 KM3NeT vertical detection units which are anchored in 3500 m depth. Each detection unit is about 700 m in height and connects 18 optical sensor modules with about 40 m distance in between (compare figure 10). The detection units will be placed about 100 m apart, instrumenting a volume of about 1 cubic kilometer which is slightly larger than IceCube. The optical sensor modules (DOMs) are glass vessels with 31 photo multiplier tubes looking in all direction to detect the Cherenkov light from the charged particles that are produced in neutrino interactions. The ORCA array will be optimised for the lower neutrino energies necessary for the measurement of the neutrino mass hierarchy and thus instrumented more densely but will also be 250 times smaller than ARCA.
The detection principle of neutrino detectors is based on neutrino interactions with nucleons of the water via deep inelastic scattering. Since neutrinos are only interacting weakly there are charged current (CC) and neutral current (NC) interactions of which the Feynman diagrams are shown in figure 9. The four different scenarios all produce different signals in the detector

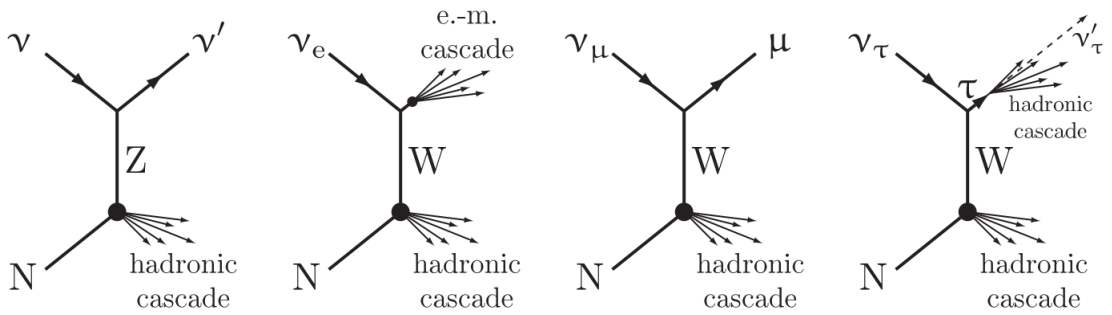

(a) NC (b) CC $e^{\pm}$ (c) CC $\mu^{\pm}$ (d) CC $\tau^{\pm}$

Figure 9: Feynman diagrams of the neutrino interaction channels visible to neutrino telescopes. A neutral current reaction resulting in a hadronic cascade and an invisible outgoing neutrino is shown in (a). Electron neutrinos reacting via the charged current yield an electron that immediately showers and forms an electromagnetic cascade overlaid to the hadronic one (b). Production of muons via CC is shown in (c), whereas (d) shows the reaction of tau neutrinos and the eventual decay of the τ into a hadronic cascade. Taken from Kopper (2010).

which collects the Cherenkov light emitted by the charged particles produced in the interaction (compare figure 10 right panel). The NC interactions happening through the exchange of a Z^0-boson look the same in the detector independent of the incoming neutrino flavour. A hadronic cascade is initiated at the interaction point which is seen by the detector but not containing all the energy of the primary neutrino since it is leaving the detector again with some of its initial energy. CC interactions with the exchange of a $W^{\pm}$-boson produce a lepton of the neutrino

[7] https://www.km3net.org/

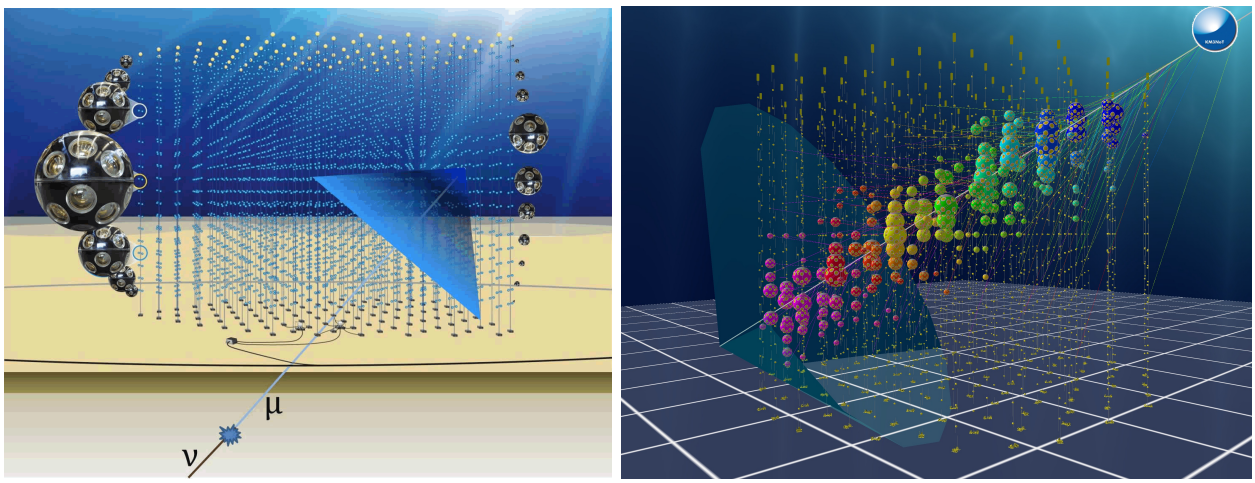

Figure 10: *Left:* Visualization of the KM3NeT array with a zoom on the optical sensors and the Cherenkov light cone from an incident muon event. *Right:* Simulation of an neutrino event seen by the KM3NeT detector. The color denotes the timing information and the size of the DOMs the amount of light registered (Credit: KM3NeT).

flavour in addition to the hadronic cascade. In case of a ν_e the resulting electron will initiate an electromagnetic cascade overlaying the hadronic one. Both cascades contain the whole energy of the incoming neutrino which is good for the energy resolution of such events. A muon produced in a ν_μ interaction can have path lengths in water ranging from a few meters at GeV energies up to a several kilometers at a few TeV. This means that for high energy muons seen by the detector it is very likely that their vertex is outside the detector which increases the effective detector volume over the actually instrumented one but makes it hard to achieve a good energy resolution. Below energies of $\sim$10 TeV the angular resolution of muon tracks is limited by the neutrino interaction kinematics. For higher energies the angle between the neutrino direction and the muon direction becomes very small which allows for the best angular resolution of all the event types because of the long lever arm of the muon tracks. For ν_τ events the initial hadronic cascade is followed by a second one when the tauon decays. Both cascades can be detected separately if the distance between them is large enough. These events are also called *double bang* events [Kopper, 2010]. Based on these detection methods neutrino telescopes can not distinguish between neutrinos and anti-neutrinos. For this analysis only muon neutrinos will be considered since both the angular resolution as well as the effective area for muon events are superior to those of electron or tauon events. Currently ARCA is running in a starting phase with one string. After completion the data will be publicly available with a delay time of two years. The IRFs should be available by next year already.

A mathematical truth is timeless, it does not come into being when we discover it. Yet its discovery is a very real event, it may be an emotion like a great gift from a fairy.

(Erwin Schrödinger)

4. Methodology

4.1 The Gammapy package

Gammapy[8] is an open-source Python package primarily developed for the analysis of IACT data. It is based on existing Python packages like `numpy`, `scipy` and `astropy`. Even though it is a prototype for the CTA science tools it can also be used to analyse data from different instruments if the necessary instrument response functions (IRFs) are given. During the writing of this thesis Gammapy is still in development and the latest stable version (v0.17) is used for all the relevant analyses.
Gammapy features one dimensional spectral analyses, temporal analyses by calculating the light curve and three dimensional analyses with one spectral and two spatial dimensions of the given observations. Only the latter is relevant for this work and will be discussed here. The IRFs, measured counts, background model and source model(s) are all combined in the `MapDataset` class. The information of the reduced data and IRFs is stored in `WcsNDMap` classes. The data is stored in a ND numpy array together with an `WcsGeom` object which holds the information about the pixel coordinates and the axes of the map. For more information on the implementation of the IRFs in Gammapy see section 5.1.1.

There are various built-in spectral and spatial models within Gammapy. The spectral models return a flux $\Phi(E)$ dependent on the energy E and the spectral parameters. Relevant for this thesis are the power-law model parameterizing the flux in the following way

$$\Phi(E) = A \cdot \left(\frac{E}{E_0}\right)^{-\Gamma} \tag{4.1}$$

and the exponential-cutoff power-law model

$$\Phi(E) = A \cdot \left(\frac{E}{E_0}\right)^{-\Gamma} \exp\left[-\left(\frac{E}{E_{\text{cut}}}\right)^{\beta}\right] \tag{4.2}$$

with A the amplitude, E_0 the reference energy, Γ the spectral index, E_{cut} the cutoff energy and β the cutoff exponent. There is also the Log Parabola model

$$\Phi(E) = A \cdot \left(\frac{E}{E_0}\right)^{-\alpha-\beta\log(E/E_0)} \tag{4.3}$$

[8] https://gammapy.org

where β describes the curvature of the model. Also important for this work is the `NaimaSpectralModel` class which takes a NAIMA radiative model as argument and returns the flux predicted by it. For more detail see section 4.5.
The spatial models return the flux dependent on the sky coordinates and other parameters. The simplest model is the Point spatial model where all of the flux is assigned to just one pixel if the source position is also centered on that pixel. Else the flux is re-distributed across the four neighbouring pixels to ensure the center of mass position is conserved. For extended sources one can use the Disk spatial model which distributes the flux in a disk with radius r_0 in a way that the flux inside the disk is constant and outside zero. Or the Gaussian spatial model which distributes the flux according to a Gaussian

$$\Phi(\theta) = N \times \exp\left(-0.5 \cdot \frac{1-\cos\theta}{1-\cos\sigma}\right) \tag{4.4}$$

where N is the normalization, θ is the sky separation to the model center and σ is the extension of the model. Both the Disk and Gaussian model are normalized so that the total flux of the model is conserved. They can also be elongated with an eccentricity and rotation angle.
The spectral and spatial models are combined in the `SkyModel` class which then returns the model flux dependent on the energy and the spatial coordinates.
For the analysis a binned maximum likelihood method is implemented. The source models are evaluated on the geometry of the exposure map which gives a number of predicted counts for each pixel. The energy axis of the exposure map is defined in *true* energy, the spatial axes are the same as for the counts map. The predicted-counts map is then *forward folded* with the Energy Dispersion matrix for the energy dimension and with the Point Spread Function for the spatial dimensions. After that the predicted-counts map is given in *reconstructed* energy which is the same as for the counts map. True and reconstructed energy can differ in e.g. the number of bins per decade so the model can be evaluated in a finer energy binning which increases the precision. The background model is already defined on the counts geometry and simply holds the number of predicted background counts for the live time of the data set. It can be scaled using its `norm` parameter and tilted in the energy dimension. After all models are evaluated the resulting maps are stacked which gives the total number of predicted counts in each pixel for the respective model parameters.
For each `MapDataset` one can set masks, the `mask_safe` defining the safe data range and the `mask_fit` defining the data range used for the Fit. The `Fit` class takes a list of data sets and only considers pixels where both masks are `True`. It offers different fitting backends like "minuit"[9], "sherpa"[10] or "scipy"[11] to maximize the agreement between the model and data by variation of the free model parameters.

4.2 A Binned Maximum Likelihood Analysis

The *test statistic* or TS-value is a measure for the agreement between the experimental data and the model prediction. An ideal model would predict exactly the number of measured counts in each pixel, however a realistic analysis will always show some discrepancies or *residuals* between the measured data and the predicted one. In order to find the model most likely to best describe

[9] https://iminuit.readthedocs.io/en/stable/index.html
[10] https://cxc.cfa.harvard.edu/sherpa4.12/
[11] https://docs.scipy.org/doc/scipy/reference/generated/scipy.optimize.minimize.html

the data, the likelihood $\mathcal{L}(\xi)$ for a set of model parameters ξ is computed in the following way

$$\mathcal{L}(\xi) = \prod_{i=1}^{N} \mathcal{P}(n_i|\nu_i(\xi)) \tag{4.5}$$

with

$$\mathcal{P}(n_i|\nu_i(\xi)) = \frac{\nu_i^{n_i}(\xi)}{n_i!} \cdot \exp(-\nu_i(\xi)) \tag{4.6}$$

being the Poisson probability to measure n_i events given the model prediction $\nu_i(\xi)$ in the pixel i. The TS-value is defined as

$$TS \equiv -2\ln\mathcal{L}(\xi) = -2\sum_{i=1}^{N} \ln\left(\frac{\nu_i^{n_i}(\xi)}{n_i!} \cdot \exp(-\nu_i(\xi))\right) \tag{4.7}$$

If one wants to find the parameter values that fit the measured data best one has to maximize $\mathcal{L}$ or minimize the TS-value [Tanabashi et al. (2018, chapter 39.2.2)][Mohrmann, 2015].
The parameters can be confined into a physically reasonable range using hard boundaries which the parameters can not exceed at all, or by using penalty terms which add contributions to the total TS-value for deviations from some central values ξ^*. While the hard boundaries correspond to a box-potential where the parameter can move freely inside, the so-called *prior* functions can describe any kind of potential. Often times one would use a set of Gaussian-shaped functions which then add contributions to the TS-value in the following way

$$TS = -2\sum_{i=1}^{N} \ln\left(\frac{\nu_i^{n_i}(\xi)}{n_i!} \cdot \exp(-\nu_i(\xi))\right) + \sum_{m} \frac{(\xi_m - \xi_m^*)^2}{\Delta\xi_m^2} \tag{4.8}$$

where one can control the width of the potential for each parameter ξ_m by adjusting $\Delta\xi_m$. This approach can also be used when one needs to constrain quantities during the fit that are not free parameters of the fit itself. One example could be to confine the ratio of two models during the fit.

4.3 Likelihood Ratio Tests and confidence intervals

If one wants to compute the level of agreement of two models M1 and M2 to some measured data one can use the ΔTS-value.

$$\Delta TS = TS_{\mathrm{M1}} - TS_{\mathrm{M2}} = -2\ln(\mathcal{L}_{\mathrm{M1}}/\mathcal{L}_{\mathrm{M2}}) \tag{4.9}$$

Wilk's theorem states that if the two models are nested, e.g. the parameter space of M1 is a subset the parameter space of M2 and the sample size is sufficiently large and no parameter value is close to a physical bound, then the ΔTS-value is χ^2 distributed with k degrees of freedom, where k is the difference in number of free parameters between M1 and M2 [Wilks, 1938],[Mohrmann, 2015]. In this case the square root of the ΔTS-value corresponds to the significance with which M2 is preferred over M1.
If one the conditions above is not full filled one might not want to trust Wilk's theorem but instead use the more general Bayesian approach. Here the probability which indicates how much more likely M2 is compared to M1 can be calculated by solving equation 4.9 for the likelihood ratio.

$$\frac{\mathcal{L}_{M1}}{\mathcal{L}_{M2}} = e^{-\frac{1}{2}\Delta TS} \tag{4.10}$$

In order to obtain confidence intervals for one parameter, a so-called *profile likelihood scan* is carried out. The parameter of interest is fixed to a set of values in a range around its best-fit value and the TS-values are calculated and compared to the TS-value without this constraint. If the ΔTS-values follow a parabola when plotted over the scanned parameter values then it is χ^2-distributed and the confidence intervals follow analogously. If this is not the case a ΔTS-value does not directly correspond to a confidence interval but one can still use equation 4.10 to compute the probability density function (p.d.f) for the parameter values. Then one can look for the parameter values for which the integral over the p.d.f contains e.g. 90% of its area in order to obtain the 90% confidence interval.

4.4 Pseudo Experiments

Knowing the Instrument Response Functions of an instrument one can simulate measured data even if the instrument is not built yet. Like this one can estimate its sensitivity to certain source models. There are two possibilities to do that.
The first is to draw Poisson randomized counts based on the model prediction for each pixel. The drawback of this method is that one needs a sufficiently large number of these *pseudo experiments* in order to average over statistical fluctuations.
The second possibility is to use the so-called *Asimov data set*. Here the counts cube is exactly the predicted counts cube without any randomization. Hence a minimization of the TS-value would will return the input parameters. Cowan et al. (2011) have shown that this data set is a representative data set for the assumed model prediction without the statistical fluctuations of the first method. So it can also be used to estimate the expected sensitivity of the experiment.

4.5 NAIMA Models

NAIMA[12] is a Python package for computation of non-thermal radiation from relativistic particle populations. GAMMAPY has a wrapper class for the NAIMA models, the `NaimaSpectralModel` class which takes a NAIMA radiative model and a distance to the source as arguments and returns the observed flux at Earth based on the particle distribution of the radiative model. Like this the parameters of the primary particle distribution can be fitted directly to an observation using a maximum likelihood method (see section 4.2). For the leptonic emission scenarios NAIMA offers an Inverse Compton (IC) model which calculates the γ-ray emission based on an electron population and seed photon fields (see section 2.1.1) based on Khangulyan et al. (2014). This analytical approximation of IC upscattering of blackbody radiation is accurate within one per cent over a wide range of energies. It is also possible to use a Synchrotron Self Compton (SSC) model which calculates the IC upscattering of the Synchrotron emission from the same electron population. The Synchrotron emission is calculated according to Aharonian et al. (2010). This is particularly interesting e.g. for pulsar wind nebulae as the Crab nebula.
For the hadronic emission scenarios NAIMA offers two Pion Decay (PD) models. The standard one is based on an analytic parametrization of Kafexhiu et al. (2014) but only predicts the γ-ray flux. The other one is based on a parametrization of Kelner et al. (2006). While the NAIMA model also only predicts the γ-ray flux the paper also gives a parametrization for the neutrino and electron flux from proton-proton-interactions. For this thesis a Pion Decay model was implemented in a similar way to the existing one, with the extension to also predict the neutrino flux, including a factor that takes neutrino oscillations on the way from the source to Earth into account. The predicted fluxes for the secondary particles can be seen in figure 11 where also the γ-flux of the NAIMA Pion Decay model is compared to the γ-flux predicted by the Kelner06 model. While the agreement between the models is very good at 100 GeV the

[12] https://naima.readthedocs.io

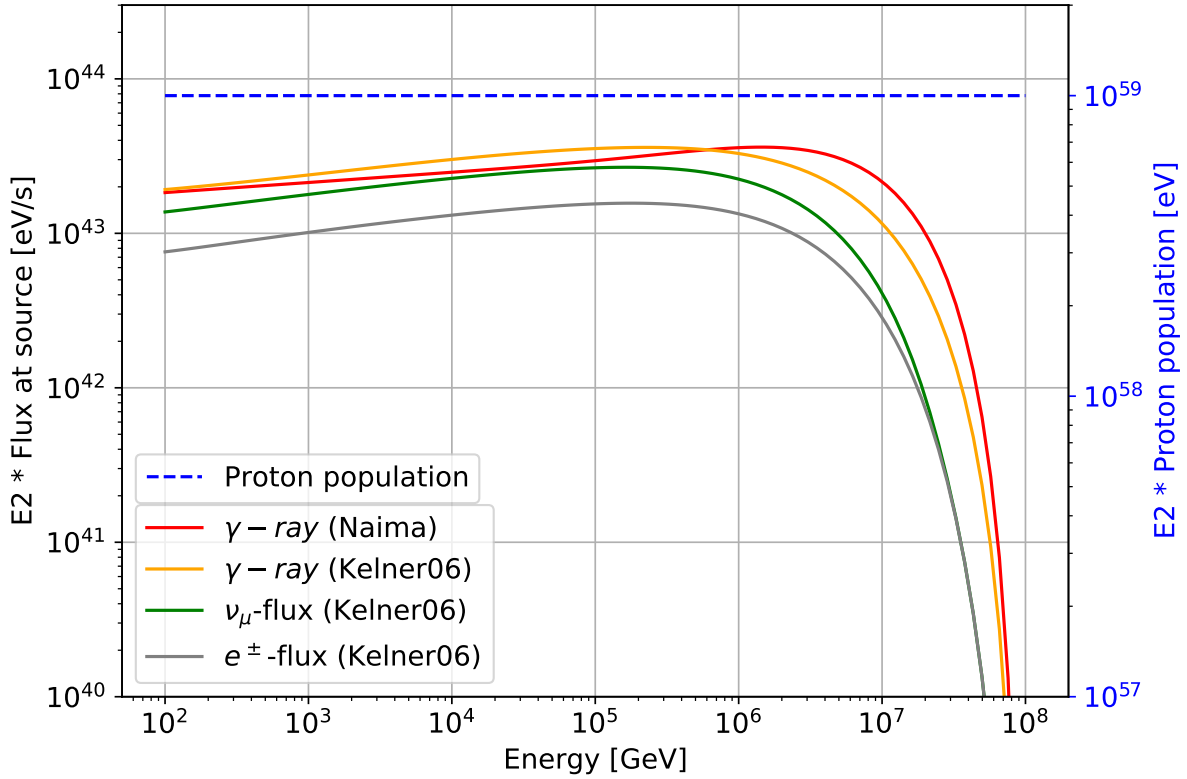

Figure 11: Spectra of secondary particles produced in pp-interactions at the source with the target density being $1/\mathrm{cm}^3$. The blue dashed line indicates the proton spectrum, a power-law with index 2. The red and orange lines show the γ-ray spectra based on Kafexhiu et al. (2014) and Kelner et al. (2006), respectively. The green line shows the muon neutrino flux not considering any oscillation factor. The gray line indicates the electron spectrum which also coincides with the electron neutrino spectrum. The last two are also based on the Kelner06 parametrization.

discrepancy becomes larger at higher energies but for most of the energy range the models agree within 20%. The Pion Decay model from NAIMA additionally gives the option of including the *nuclear enhancement factor* described in their paper which increases the γ-ray flux by $\sim$70%. This is not the case for the Kelner06 model used in this work, however here mostly the ratio between γ-rays and neutrinos is of interest, not so much the absolute normalization of the corresponding proton flux. The ratio of γ-flux to ν_μ-flux is between 1.32 and 1.40 for most of the energy range. Since the model only considers protons up to an energy of 100 PeV there is a cutoff in the neutrino and γ-ray spectra at $\sim$5 PeV and $\sim$10 PeV, respectively.

How insidious Nature is when one is trying to get at it experimentally.

(Albert Einstein, "Letter to Michele Besso")

5. Combined KM3NeT - CTA analysis

To exploit the multi-messenger connection it is very interesting to combine the results of neutrino and γ-ray measurements. Neutrinos and γ-rays are both uncharged so they point back to their sources and the measured flux at Earth can lead to conclusions about the primary particle population at the source as explained in section 2.1. The goal of this combined analysis of neutrino and γ-ray data is to fit a composite model containing a leptonic and hadronic component to the respective fluxes from a source and put constraints on the contributions. All the results in this section are obtained with GAMMAPY version 0.17.
In the first part of this section (5.1) the analysis preparations are presented followed by the *initial* results in section 5.2. In the third part (section 5.3) improvements to the analysis are conducted and the *updated* results are discussed and compared to the initial ones.

5.1 Analysis preparations

In order to perform simulations using GAMMAPY the IRFs of the instruments need to be stored in the correct format. While this is already the case for CTA, the IRFs for KM3NeT/ARCA need to be extracted from Monte-Carlo simulations. Also the background needs to be modeled and data sets need to be generated using the IRFs, background and source models. The details on this procedure will be presented in this subsection.

5.1.1 Instrument response functions for KM3NeT

For the forward modeling process one needs to know how the detector responds to a flux of incoming particles. In order to get this information the propagation of particles in the detector is modeled using Monte-Carlo simulations (MC version 5.1, details on the simulations can be found on the KM3NeT wiki page[13]). These simulations were provided by Tamás Gál from the KM3NeT group at ECAP. The whole simulation contains 200 files each with 10^5 simulated neutrino events following a power-law spectrum (equation 4.1) with an index $\Gamma = 1.4$. GAMMAPY requires the instrument data in the (DL3) common format[14] so the IRFs are extracted from the simulations and stored in FITS files. For the generation of the IRFs the spectrum has been re-weighted to a power-law with index 2.5 which is a typical index for a galactic γ-ray source and the following quality cuts have been applied:

- Likelihood > 60 (quality of event reconstruction)
- Beta0 < 0.1 (curvature of the likelihood profile)
- $E_{reco} > 100\,\text{GeV}$

[13] https://wiki.km3net.de/index.php/Simulations#MC_Productions
[14] https://gamma-astro-data-formats.readthedocs.io/en/latest/index.html

The first two quality cuts are standard cuts based on the KM3NeT wiki and remove badly reconstructed events. The last one is valid since the atmospheric background is heavily dominating below 100 GeV and it does also remove poorly reconstructed events further improving the IRFs (for details on the distribution of events with respect to the used quantities see Appendix C). Note that the quality cuts are not optimized for a particular source spectrum and background model combination which could enhance the sensitivity of the analysis but is beyond this work.

5.1.1.1 Effective area

The effective area combines the detection efficiency of the detector with an observable area. It depends on the energy of the incoming particle as well as on its direction. If the effective area is multiplied with the live time one gets the exposure in units of [m^2s]. This can be multiplied with a model flux density in units of [1/(TeV m^2 s)] to get the predicted number of events in an energy interval.
For the KM3NeT detector one can calculate the effective area from the simulations. GAMMAPY expects the effective area in a two dimensional array binned in true energy E_{true} and zenith angle θ. Therefore the simulated events are binned in energy (10^2- 10^8 GeV, logarithmic binning, 8 bins/decade, 48 bins in total) and in $\cos\theta$ (from -1 to 1, linear, 20 bins) where $\theta = 0°$ refers to down-going events coming from above the detector and $\theta = 180°$ refers to up-going events that traveled through the Earth. Since the events are generated isotropically, a linear binning in $\cos\theta$ ensures that every bin contains the same amount of solid angle and thus approximately the same statistics in events.
The actual effective area content in each bin can be calculated using the generation weight w2 for each of the simulated events contained in the bin edges E_1, E_2 and $\cos\theta_1, \cos\theta_2$

$$A_{eff} = \frac{1-\gamma}{F \cdot (\cos\theta_2 - \cos\theta_1)({E_2}^{1-\gamma} - {E_1}^{1-\gamma}) \cdot N_{tot}} \sum_i E_i^{-\gamma} \cdot \text{w2}_i \tag{5.1}$$

$F = 365 \cdot 24 \cdot 3600$ is a factor to get from years to seconds, γ is the index of the assumed spectrum (1.4 unless re-weighted) and $N_{tot} = 200 \cdot 10^5$ is the number of total events. The generation weight w2 contains information about the generation time and area, the interaction probability and the transmission probability through the Earth. The effective area is scaled by a factor of two to account for the two "building blocks" of KM3NeT/ARCA.
The resulting matrix can be seen in figure 12 and the slices for different zenith angle bins in figure 13.
In general one can see that the effective area of the detector is rising with increasing energy. This is a result of the increasing cross section of neutrino interactions for higher energies. For the low energies the effective area does not depend strongly on the direction of the events, however for the higher energies above 10 PeV the cross sections becomes so large that the Earth becomes opaque to these neutrinos which causes the drop in effective area. The calculated effective area is compared with the reference from the Letter of Intent (LoI) [Adrián-Martínez et al., 2016] in figure 13. One can see that for the medium energies the agreement of the "Average" curve with the "LoI" curve is good, while for the low and high energies the difference is increasing. This is because the quality cut of $E_{\text{reco}} > 100$ GeV removes events especially in that region as can be seen in figure 42 in the appendix. Not applying these quality cuts would not increase the sensitivity of the detector because all the events reconstructed to energies below 100 GeV would for example also worsen the energy dispersion.

5.1.1.2 Energy dispersion

The imperfect energy reconstruction of the detector also needs to be modeled in the forward modeling process. This can be done with the energy dispersion generated from simulations.

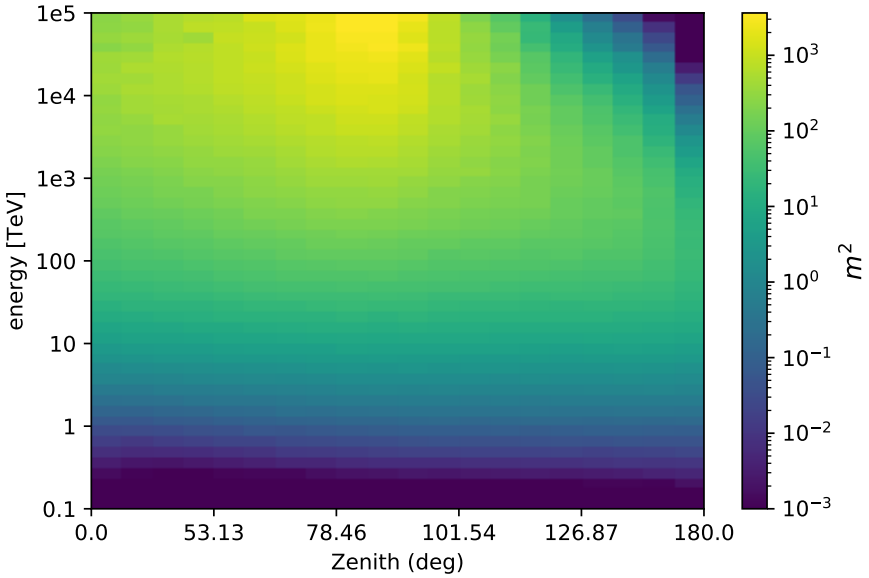

Figure 12: Effective area of KM3NeT/ARCA (scaled for two building blocks) for ν_μ calculated according to equation 5.1.

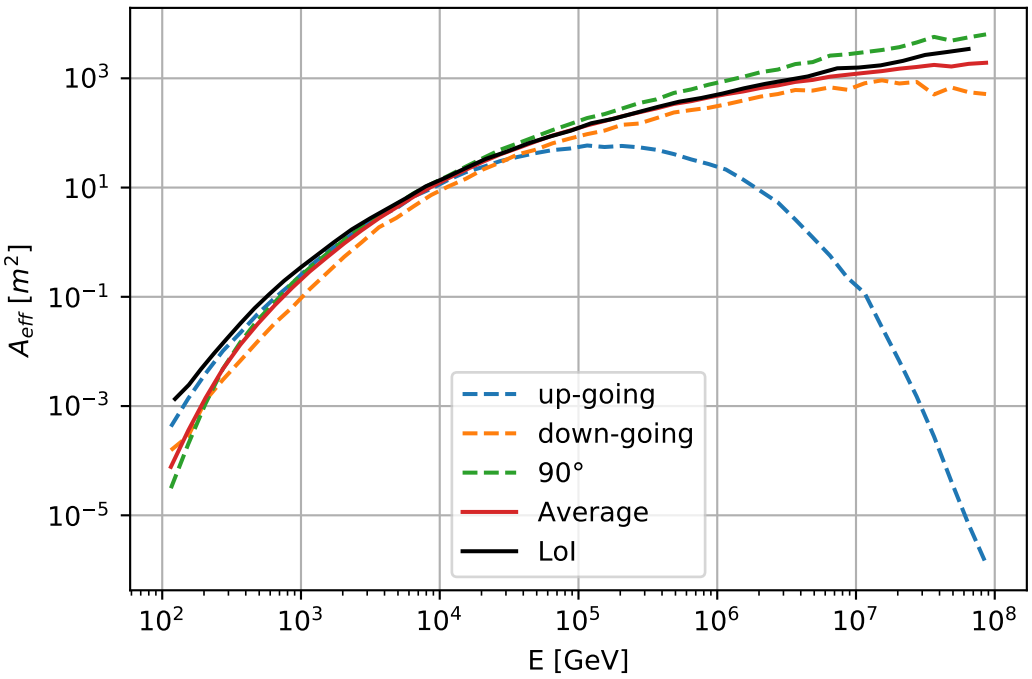

Figure 13: Effective area of ARCA (two blocks) for ν_μ calculated according to equation 5.1 shown for different zenith angle bins. The dashed blue "up-going" curve shows the effective area of the bin between 154° and 180°, "down-going" (orange) shows the bin between 0° and 26°, "90 deg" (green) shows the average of the two central bins ranging from 84° over 90° to 96°. The "Average" curve (red) shows the mean value averaged over all zenith angle bins which can be compared to the effective area from the Letter of Intent [Adrián-Martínez et al., 2016] (black).

Because of the detection principle of muon-neutrinos (described in section 3.3) one can only estimate the energy of the muon which can be quite different from the original neutrino energy. Especially for the higher energies the muons can travel a longer distance outside the detector. In the detector these muons look like muons from lower energy neutrinos because the energy they loose outside the detector can not be measured. For the simulated events one knows the true neutrino energy and the reconstructed muon energy. So one can calculate the probability $R(i, j)$ of an event from a true energy bin i to be reconstructed in an energy bin j. GAMMAPY expects the energy dispersion as a 3-dimensional matrix binned in the true energy E_{true}, the reconstructed energy E_{reco} and the zenith angle θ. The quantity stored in this matrix is the probability $\frac{dP}{d\mu}$, the PDF for the energy migration $\mu = \frac{E_{\text{reco}}}{E_{\text{true}}}$.
This can be calculated by summing all events in the bin ΔE_{true}, $\Delta\theta$ and $\Delta\mu$ and normalizing along the migration axis so that

$$\int_0^\infty \frac{dP}{d\mu} d\mu = 1 \tag{5.2}$$

In order to get the the probability $R(i, j)$ one has to integrate over the true energy

$$R(i, j) = \frac{\int_{\Delta E_{\text{true}}} R(i, E_{\text{true}})\ dE_{\text{true}}}{\Delta E_{\text{true}}} \tag{5.3}$$

where

$$R(i, E_{\text{true}}) = \int_{\mu(\Delta E_{\text{reco}})} \frac{dP}{d\mu}\ d\mu \tag{5.4}$$

and ΔE_{true} and ΔE_{reco} are the widths of the true and reconstructed energy bins, respectively. The energy reconstruction of the simulated events used in this work is compared to the energy reconstruction published in the LoI [Adrián-Martínez et al., 2016] to validate the calculated energy dispersion. This is done using the ratio of reconstructed muon energy to the true muon energy when entering the detector for muon energies between 10 TeV and 100 PeV (compare figure 14). The slight difference between the two histograms is caused by the different event

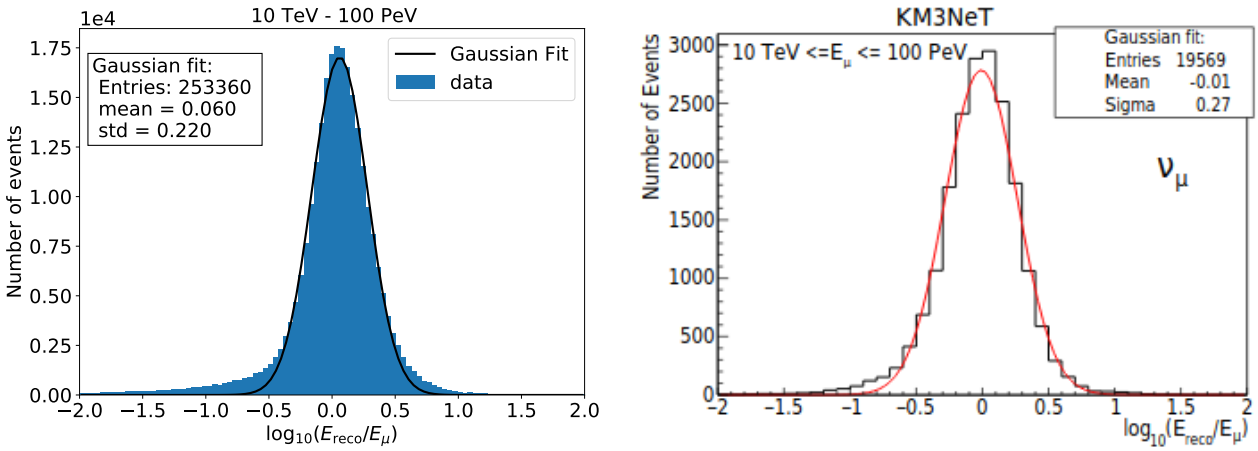

Figure 14: Energy Migration of the true muon energy E_μ when entering the detector and the reconstructed energy E_{reco} for muon energies between 10 TeV and 100 PeV. The parameters of the Gaussian fit are indicated in the figure. *Left:* For the MC events used in this work. *Right:* Comparison to the LoI [Adrián-Martínez et al., 2016]

reconstruction and possibly different quality cuts. The energy dispersion matrix calculated for GAMMAPY is binned in 24 logarithmic E_{true} bins between 10^2 and 10^8 GeV, in nine zenith angle bins (linear in $\cos\theta$) and in 56 logarithmic migration bins between 10^{-5} and 10^2. The resulting

matrix for $\theta = 90°$ can be seen in figure 15. A perfect energy reconstruction would result in a diagonal matrix so the more smeared out the matrix is the worse the energy reconstruction.

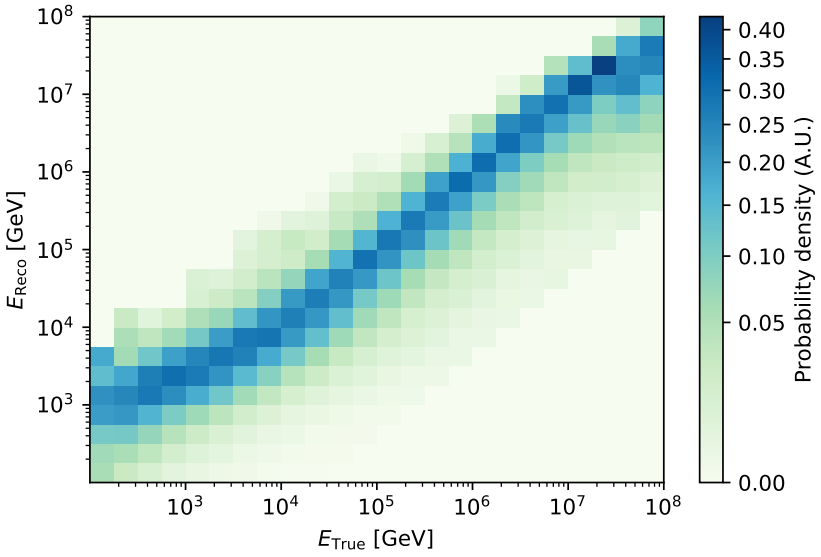

Figure 15: Energy dispersion matrix at 90° zenith angle.

5.1.1.3 Point Spread Function

The Point Spread Function (PSF) describes how the instrument would image a point source. Because of the imperfect spatial reconstruction there is a finite probability $dP/d\Omega(r)$ to find an event in a solid angle $d\Omega$ at an offset r from the source position. This quantity is stored in a matrix for the same E_{true} and $\cos\theta$ bins also used for the energy dispersion. The radial binning is chosen linear in r from 0 to 8° with 100 bins.
The angle between the MC direction $\vec{a}$ and the reconstructed direction $\vec{b}$, both given in Cartesian coordinates, is calculated using the scalar product

$$r = \arccos\left(\frac{\vec{a}\cdot\vec{b}}{|a||b|}\right) \tag{5.5}$$

The events are filled in the radial bins for each energy and zenith angle bin and normalized along the r-axis to get the probability. Figure 16 shows the distribution of r for different neutrino energies. As expected the angular resolution becomes better at higher energies. When comparing the distribution to the one published in the LoI (figure 16 right) it is a lot broader at low energies but becomes narrower at high energies. This has two main reasons, the first one is that the simulations used in this work have a new reconstruction algorithm which offers improved angular reconstruction at high energies. The second reason is that the quality cuts which were applied to the events in order to obtain these distributions are different.

5.1.2 Background models for KM3NeT

As discussed in section 3.3 KM3NeT will detect neutrinos based on the Cherenkov light emitted by muons which are produced in muon-neutrino interactions. Since both muon-neutrinos and muons are produced in hadronic air showers there are two background contributions, the atmospheric neutrinos and the atmospheric muons, when detecting cosmic neutrinos. The

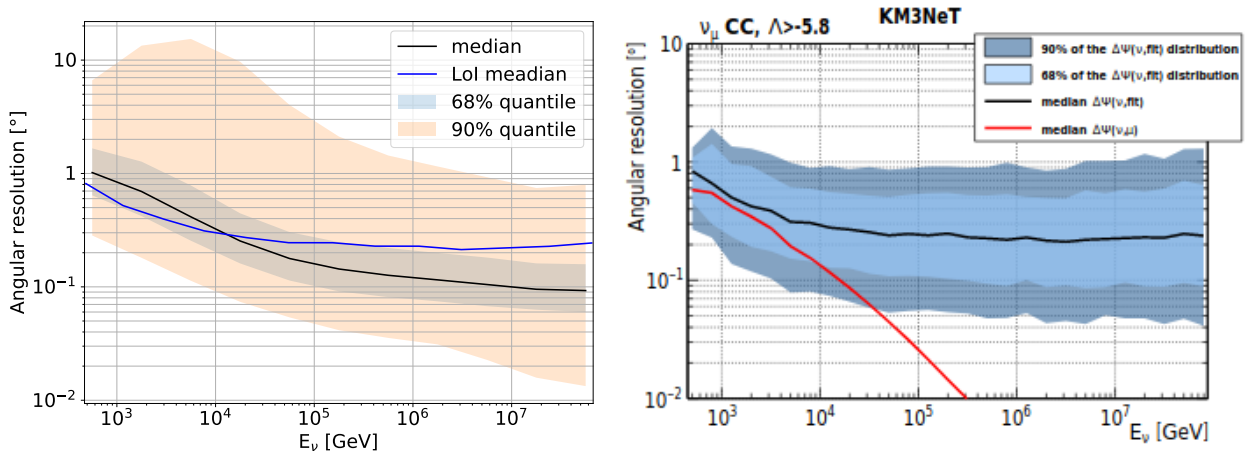

Figure 16: Angular resolution of the KM3NeT/ARCA detector after the quality cuts, which is the angle between the true and reconstructed neutrino direction. *Left:* Median, 68% and 90% quantile of the angular distribution for the MC events used in this work. The blue line indicates the median of the right panel. *Right:* Comparison to the angular resolution given in the LoI [Adrián-Martínez et al., 2016].

spectra of both backgrounds are connected to the cosmic ray spectrum causing the background fluxes to strongly decrease with energy. While the atmospheric muon background is dominating below zenith angles of ∼80° it is strongly suppressed for larger zenith angles since muons cannot reach the detector in their short lifetime then. The generation of both background models will be discussed in this section. Note however that the atmospheric muon background is not considered for all the initial results.

5.1.2.1 Atmospheric neutrino background

The atmospheric background neutrino flux coming from cosmic ray induced air showers with hadronic interactions can be divided in a conventional part and a prompt part. The conventional part originates from the decay of charges pions and kaons and dominates below 1 PeV. The prompt part comes from the decay of heavier mesons typically containing a charm quark. In this work both parts are considered and calculated with the `ppflux` library developed by Clancy James and Thomas Heid[15]. Similar to the LoI the flux is based on the conventional component from Honda et al. (2007) and the prompt component from Enberg et al. (2008). Comparing to the background prediction used in the LoI (see figure 17) we find a 30 - 40% lower flux below 100 TeV when averaging over all zenith angles. When just looking at the maximum background flux at 90° zenith angle the predicted flux matches the prediction from the LoI very well at low energies but exceeds it by a factor of two at 100 TeV. One likely possibility is that the `ppflux` library does not consider the knee in the cosmic ray spectrum and thus over predicts the flux at high energies. For this analysis the difference in the high energy regime will not matter too much since the fluxes there are very low and hardly influence the sensitivity. This is mainly true for this analysis since the sources are simulated with an exponential cutoff to their spectra well below 100 TeV.
The background flux prediction is evaluated in the same energy and zenith angle binning as the effective area and multiplied with it to get background event rates. These can be seen in figure 18 for different zenith angles and energies and for different cuts on the reconstruction likelihood. While the atmospheric neutrino flux is of course unaffected by the quality cuts the

[15] https://wiki.km3net.de/index.php/HE_Astrophysics/ARCA_High_Energy_Analysis/AfterLoI#Atmospheric_neutrino_models

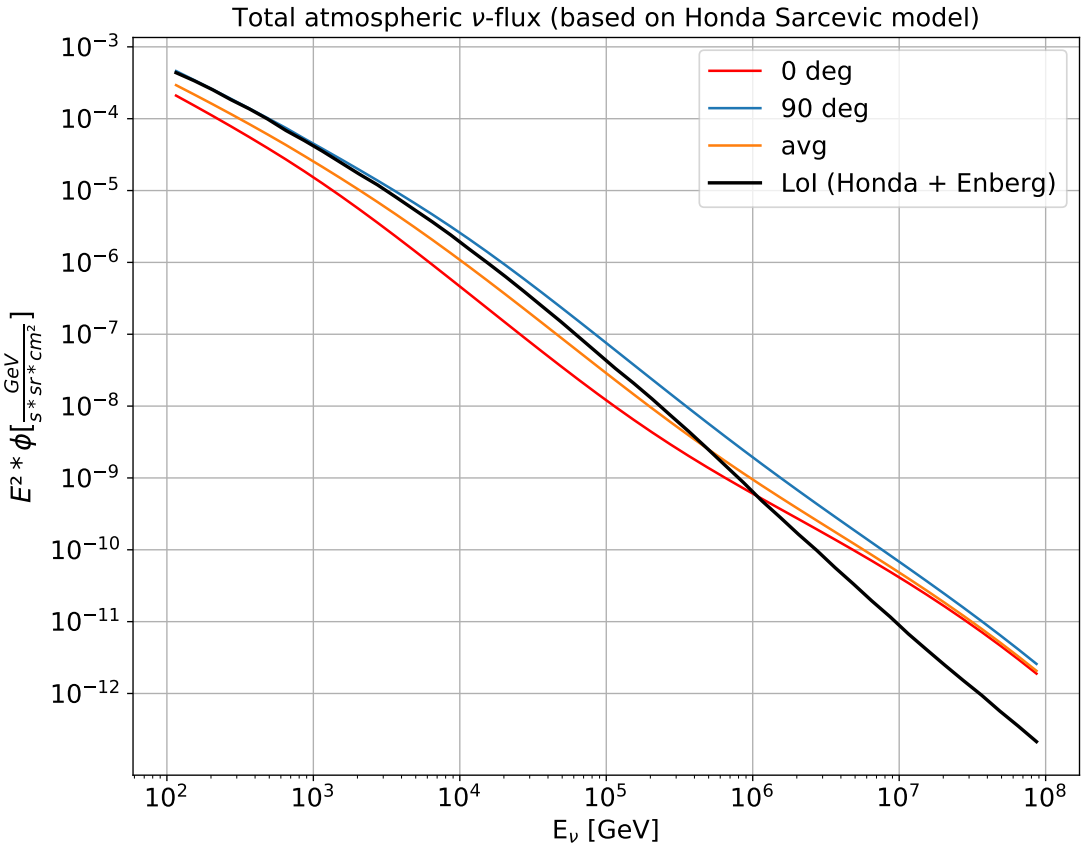

Figure 17: Conventional plus prompt atmospheric background prediction for different zenith angles. In black the comparison to the total background flux used in the LoI [Adrián-Martínez et al., 2016].

effective area is not which means that the difference in the rates for different quality cuts results from the difference in the effective area.
The matrix with the rates is stored in a FITS file which can be read in with the GAMMAPY `Background2D` class. The background model maps are generated with the `make_map_background_irf` function which essentially calculates background counts for a given geometry, pointing position and live time. This is done by multiplying the predicted background rates for each pixel with its energy and solid angle content and with the live time . This map is convoluted with the energy dispersion at the respective pointing position before given to the `BackgoundModel` class. This step is necessary because the background model is not forward folded with the IRFs in the analysis. Since the background flux is rather constant on the scale of the angular resolution of KM3NeT it is not necessary to apply the PSF to the background model map.

5.1.2.2 Atmospheric muon background

For this analysis the sources are only modeled for zenith angles larger that 80° where no more muons should reach the detector. However also muons coming from above can be falsely reconstructed as coming from below. The selection cuts used in this work are not sufficient to filter these events to a negligible amount as can be seen in figure 18. Unfortunately this was only realized after all the initial results were obtained while completely neglecting this background.

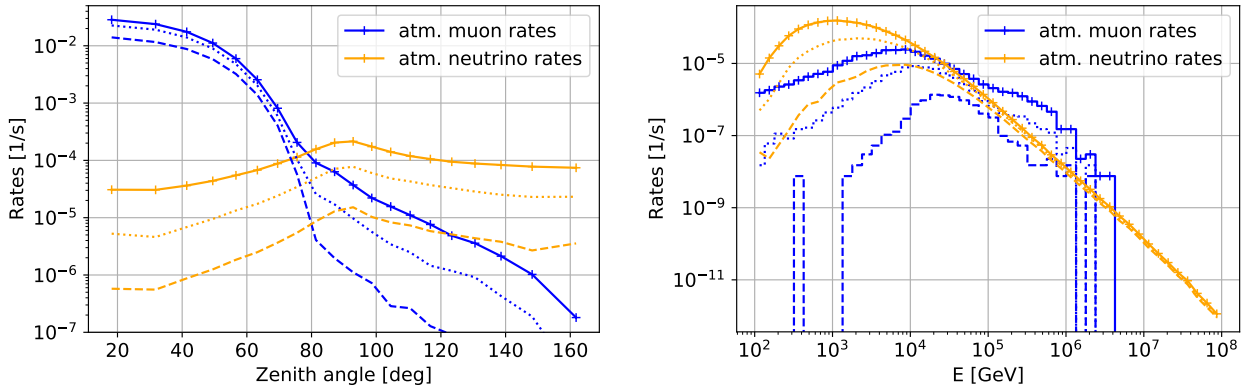

Figure 18: Rates for the atmospheric muon component (blue) compared to the rates of the atmospheric neutrino component (orange) in dependence of the zenith angle (*Left*) and of the energy (*Right*). The solid lines show the rates for the standard quality cuts with $likelihood > 60$, the dotted lines with $likelihood > 120$ and the dashed lines for $likelihood > 200$. The other cuts remained unchanged.

The rates of atmospheric muons passing the quality cuts is calculated using Monte-Carlo simulations of atmospheric muons (MC version 5.2) also provided by Tamás Gál. The events passing the quality cuts are filled into a histogram dependent on energy and zenith angle with the same binning as the effective area matrix. In order to obtain the rates the entries in the histogram are divided by the simulated live time of 4.21 years. In figure 18 one can see these rates for different cuts on the reconstruction likelihood which were attempted to suppress this background for large zenith angles even further. However the atmospheric neutrinos rates hence the effective area also decreases comparably at least for energies below 10 TeV. This is why the standard quality cuts are not changed but instead an energy dependent cut on the likelihood will be added for the updates results. For the export to a FITS file each entry of the atmospheric muon rates histogram is divided by its energy and solid angle content because the `make_map_background_irf` function will multiply the rates with these quantities of the pixels of the analysis geometry.

5.1.3 Instrument response functions for CTA

The CTA IRFs are already available in the right format and can be directly loaded with Gammapy. While the initial results are obtained using the IRFs from the first CTA data challenge[16] (1-dc), one improvement towards the updated results is the usage of the latest CTA IRFs which are publicly available here[17]. Since the production of these IRFs is not part of this thesis they will not be discussed in detail here. Note that there are (small) differences between the two sets of IRFs but they only influence the results obtained in this work to a minor extent. The latest CTA IRFs are shown exemplarily in figure 19. One can see that the effective area of CTA is orders of magnitude higher compared to KM3NeT. Also the spatial and energy reconstruction are significantly better. This explains the much higher sensitivity of CTA compared to KM3NeT which is no surprise as it is much "easier" to detect γ-rays than it is to detect neutrinos.

[16] https://forge.in2p3.fr/projects/data-challenge-1-dc-1/wiki
[17] https://www.cta-observatory.org/science/cta-performance/

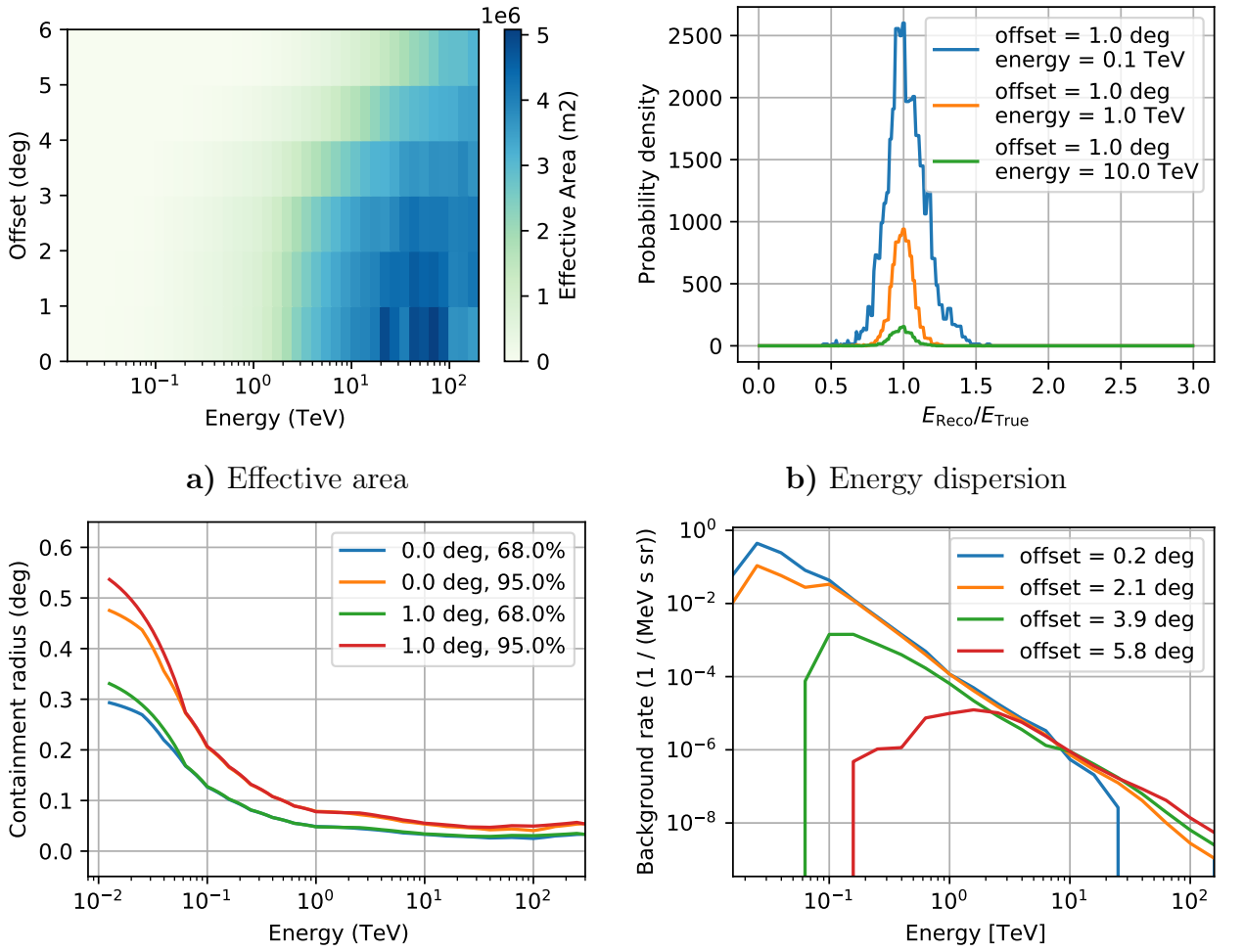

a) Effective area

b) Energy dispersion

c) Point spread function

d) Background model

Figure 19: Summary plots of the new CTA IRFs for the south array at an zenith angle of 20° optimized for 50 hours of observation time.

5.1.4 Generation of the data sets

The procedure of generating the KM3NeT data sets is the following. The zenith angles under which each source is visible from the KM3NeT/ARCA position are calculated using the ASTROPY.COORDINATES package and filled into five zenith angle bins ranging from 80° (or the minimal zenith angle if larger) to the maximal zenith angle from the source. With this method only source positions below 80° are considered where the atmospheric muon background is strongly suppressed. For each of the five bins an observation is created with the live time set according to the zenith angle histogram and the respective IRFs. The analysis geometry for the data sets was chosen like this:

- Region of interest (RoI): $30 \times 30\,\mathrm{deg}^2$
- Spatial bin size: 0.1 deg
- E_{reco}-axis: 0.1 TeV - 1 PeV (4 bins/decade)
- E_{true}-axis: 0.1 TeV - 10 PeV (16 bins/decade)

Different energy as well as spatial bin sizes have been tested to estimate their influence on the sensitivity which does not change much if the bin sizes are further decreased. The atmospheric neutrino background fluxes are multiplied with the exposure and convoluted with the energy dispersion matrix to get the background rates used in the analysis. While for the initial results the atmospheric muon rates were neglected they are added to the atmospheric neutrino rates

for the updated results. Then the five data sets from the five observations are stacked up which essentially means that a single data set is produced where the exposure, counts and background rates of the individual data sets are added and the energy dispersions and PSFs are averaged.

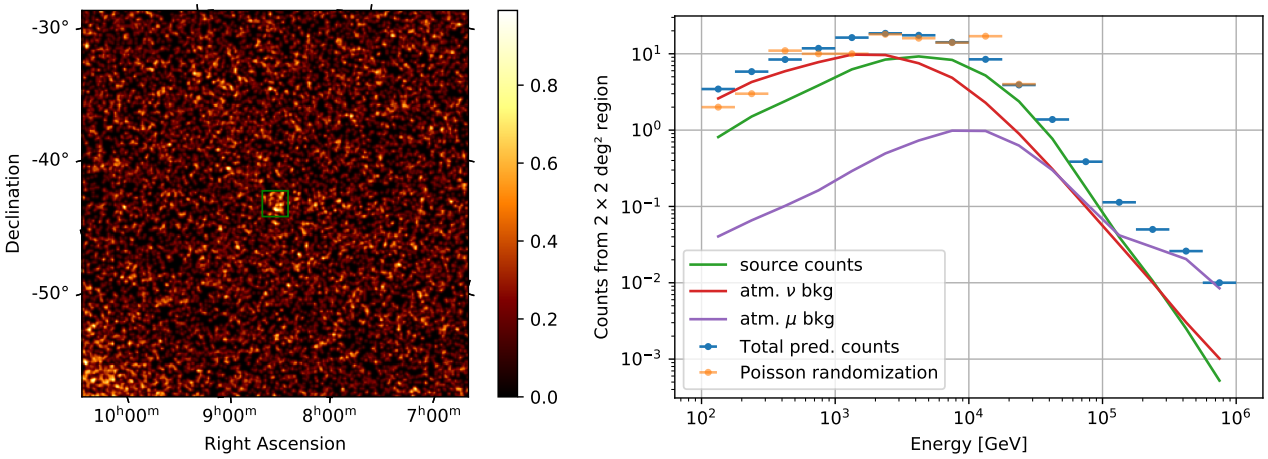

Figure 20: *Left:* Exemplary counts map of a KM3NeT data set for Vela X with 10 years of observation time. The counts are Poisson randomized based on the model prediction for Vela X, summed over all energies and smoothed with a 0.1° Gaussian. The green rectangle shows a 2×2 deg^2 region from which the counts spectra are extracted. *Right:* Counts spectra extracted from a 2×2 deg^2 region. The orange points show the counts from the realisation shown in the left panel. The blue points and solid lines show the total model prediction and for each component separately.

An exemplary KM3NeT data set is shown in figure 20 where a typical source model for Vela X (compare figure 22) gives the counts prediction for 10 years of observation time. In the sky map one can see the slight clustering of events around the source position and in the counts spectra that the source flux is only barely exceeding the background counts and only in a limited energy range. One can also see that for energies above ∼40 TeV the source prediction drops below one event and as a result there are no counts drawn inside the source region above 32 TeV for this particular example.
For the initial results the CTA data sets are generated by loading the observations simulated in the 1-dc. As the simulated live time is not matching the desired live time for the simulations of this thesis, the exposure and background normalisation are scaled accordingly. The draw back of this method is that the offset under which the sources are simulated for the runs of the 1-dc are not always optimal since the sources of interest in this thesis were not the main objectives for the 1-dc. So for the new IRFs four observations are simulated with four different pointing positions each with an offset of 1° with respect to the source position (±1° in longitude and ±1° in latitude). The CTA data sets are then generated in a similar way to the KM3NeT data sets using the generated observations containing the live time and IRFs and an analysis geometry which is chosen the following:

- ROI: $6 \times 6\,\mathrm{deg}^2$
- Spatial bin size: 0.02 deg
- E_{reco}-axis: 0.1 TeV - 154 TeV (16 bins/decade)
- E_{true}-axis: 0.1 TeV - 154 TeV (16 bins/decade)

The data sets do not have any energy dependent mask but all regions with an offset to the pointing position larger than 4° are excluded. The four data sets are also stacked up in the end resulting in one single data set. Similar to figure 20 an exemplary CTA data set of Vela X can be seen in figure 21. Because of the higher statistics, the better angular resolution and

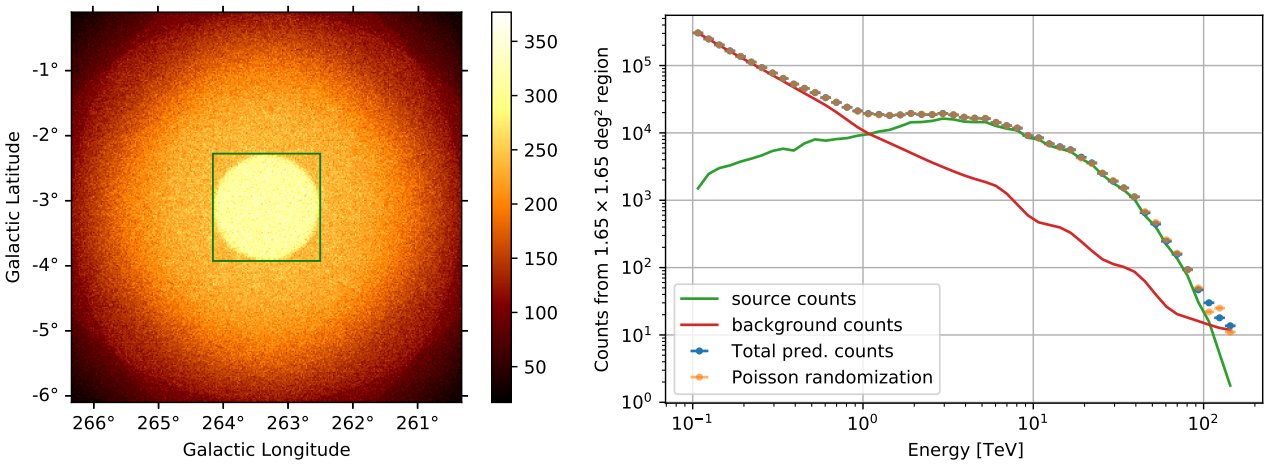

Figure 21: *Left:* Exemplary counts map of a CTA data set for Vela X with 200 hours of observation time. The counts are Poisson randomized based on the model prediction for Vela X, summed over all energies and smoothed with a 5 mdeg Gaussian. The green rectangle shows a 1.65×1.65 deg^2 region from which the counts spectra are extracted. *Right:* Counts spectra extracted from a 1.65×1.65 deg^2 region. The orange points show the counts from the realisation shown in the left panel. The blue points and solid lines show the total model prediction and for each component separately.

the smaller RoI one can clearly see the extension of the source model in the sky map. There are only very few background counts in the edges because the background rates decrease with increasing offset but more importantly only one data set can contribute in each corner because of the offset mask. For the CTA data sets there is only one background component which is dominating the spectrum of Vela X below 1 TeV.

5.2 Initial results

These initial results are based on a KM3NeT sensitivity obtained with the standard, not optimized quality cuts mentioned in section 5.1.1 and by **not** including the atmospheric muon background. This sensitivity is calculated in the following section and is compared to the published KM3NeT sensitivity according to Aiello et al. (2019).

5.2.1 Estimation of KM3NeT sensitivity

In order to compare the discovery potential of the generated neutrino data sets to a published paper, a similar approach was taken as in Aiello et al. (2019). For the sources HESS J1614−518, Vela Jr, Vela X, RX J1713.7−3946 and the galactic center spatial and spectral models are used based on γ-ray observations assuming 100% hadronic production. The spatial models are `DiskSpatialModels` giving a constant flux inside a disk with radius r_0 and the spectral models are `ExpCutoffPowerLawSpectralModels` (except HESS J1614−518 (1)) parameterized according to equation 4.2. The expected flux Φ_ν of each source can be seen in figure 22 in comparison with the expected background flux in a 1 deg^2 region. The model parameters are listed in table 1. To estimate the sensitivity the Asimov approach is taken where the measured counts in each pixel is taken to be the mean prediction for that pixel based on the background and source model. For different observation times between 1 and 20 years the flux normalization is calculated needed to get a TS-value ($\mathrm{TS} = -2\log\mathcal{L}$) $TS1$ so that $\Delta\mathrm{TS} = TS0 - TS1$ is 9 (corresponding to 3σ). The TS-value for the nullhypothesis $TS0$ is calculated based on the assumption that all counts are due to the background.

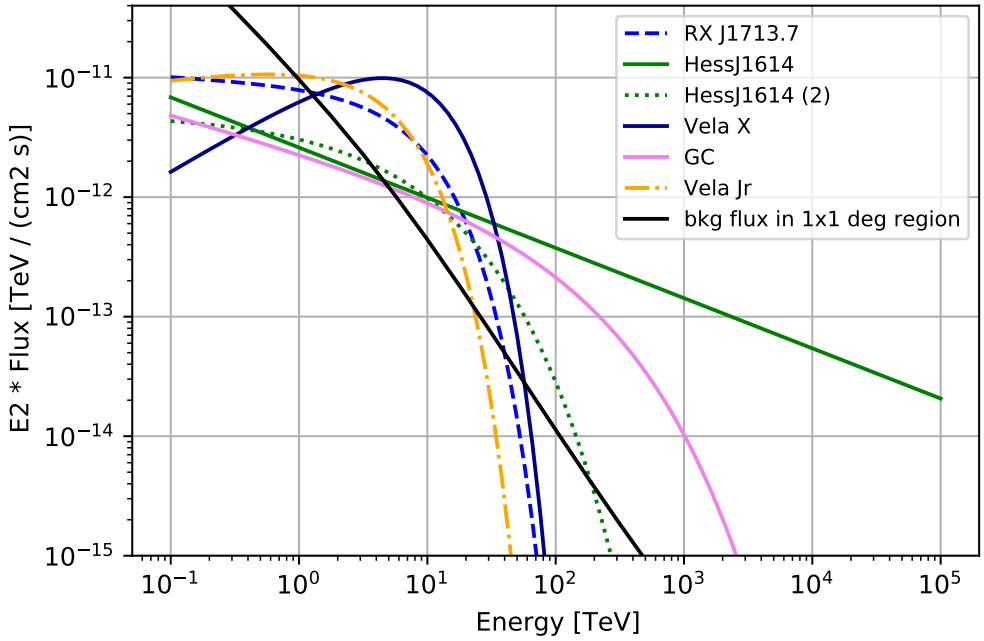

Figure 22: Spectral models of the sources used in the sensitivity study (the same as in [Aiello et al., 2019]). The parameters of the models can be found in table 1. In black the total atmospheric background flux expected in a 1×1 degree region at 103.5° zenith angle.

Table 1: Model parameters for the sources investigated for the sensitivity study. The parameters are taken from Aiello et al. (2019, table 1). The flux is parameterised according to equation 4.2 with $E_0 = 1\,\mathrm{TeV}$.

Source	radius [°]	A [$10^{-11}\mathrm{TeV}^{-1}\mathrm{s}^{-1}\mathrm{cm}^{-2}$]	Γ	E_{cut} [TeV]	β
RX J1713.7−3946	0.6	0.89	2.06	8.04	1
Vela X	0.8	0.72	1.36	7	1
Vela Jr	1	1.30	1.87	4.5	1
HESS J1614−518 (1)	0.42	0.26	2.42	–	–
HESS J1614−518 (2)	0.42	0.51	2	3.71	0.5
Galactic Center	0.45	0.25	2.3	85.53	0.5

The dashed lines in figure 23 show the discovery potentials calculated in this work. E.g. Vela X could be discovered at the 3σ confidence level in ∼2 years if the γ-ray flux is produced 100 % hadronically. In case the true neutrino flux arriving at Earth is just 50 % of Φ_ν Vela X could still be discovered in ∼5 years. Comparing to the solid lines from Aiello et al. (2019) one sees that a higher flux is needed to achieve the $3\,\sigma$ in the same observation time for all sources with an cutoff to their spectral models. For the one source without a cutoff (HESS J1614−518 (1)) the discovery potential is actually higher than in the paper. Excluding this exception the shape of the curves is very similar but they are shifted along the x-axis by a factor of ∼0.75. This means that the sensitivity of the GAMMAPY data sets can be obtained with a more sophisticated

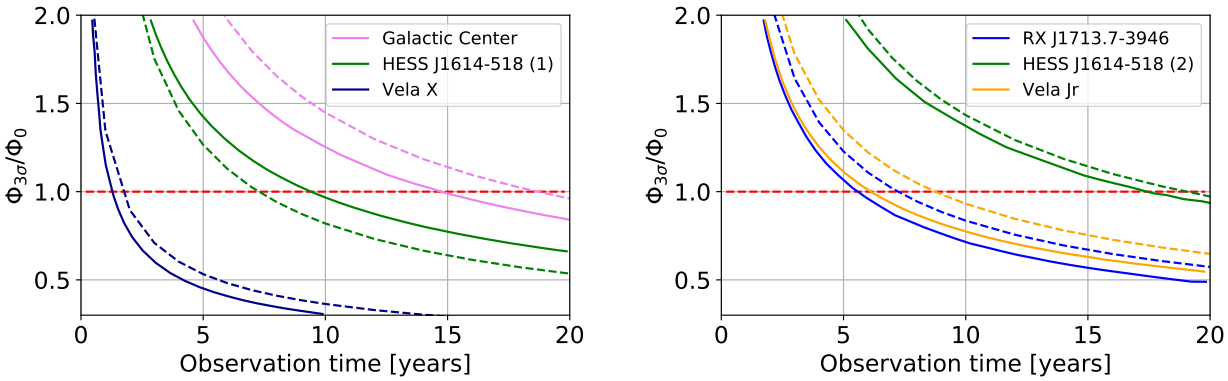

Figure 23: Ratio of the 3 sigma discovery potential $\Phi_{3\sigma}$ to the expected neutrino flux Φ_ν of each source assuming 100% hadronic production. The dashed lines show the discovery potentials calculated in this work, the solid lines show the discovery potential from Aiello et al. (2019). *Left:* For the galactic center, Vela X and HESS J1614−518 without a cutoff to its spectrum. *Right:* For Vela Jr, RX J1713.7−3946 and HESS J1614−518 with a cutoff.

analysis already after 75% of the observation time.
The main difference between the analyses in Aiello et al. (2019) and this analysis is the usage of an unbinned likelihood analysis in the paper which is more sensitive in this low statistic case. They also used more sophisticated quality cuts optimized for each source spectrum as well as a Random Decision Forest algorithm to reduce the background. In contrast to the background model used here they additionally consider the atmospheric muon background. Since they achieve a higher sensitivity this shows that the muon background can be filtered to a large extent using appropriate cuts. The reason why HESS J1614−518 (1) has a higher discovery potential is most likely due to the different event reconstruction used in this work which gets better towards higher energies (compare figure 16).
This sensitivity estimation shows that the GAMMAPY analysis in this form is not able to reproduce the published KM3NeT sensitivity in the same observation time. However it can still be used to simulate a KM3NeT analysis when scaling the observation times accordingly. For the results presented in this thesis the KM3NeT data sets are simulated with 2.5, 5 and 10 years of observation time which means that one can obtain similar results in a shorter time span by optimizing the analysis.

5.2.2 Test of a combined analysis on the Crab nebula

In this section an Injection-Recovery-Test is performed for such a combined analysis using the Crab nebula as source. It should confirm that the combined fitting of one γ-ray data set together with a neutrino data set is performed correctly within GAMMAPY. The KM3NeT data set is generated as described in section 5.1.4 with an observation time of 10 years, where the Crab nebula is visible below 80° zenith angle for only 48% of this time. The CTA data set is generated using 14 observations simulated in the galactic plane survey of the 1st-Data-Challenge, where the Crab nebula is observed under a relatively large offset of 4.8°. The safe energy range is calculated based on the energy dispersion bias being below 10% which is only the case above 1 TeV for these observations. Without doubt there will be much more and higher quality CTA data of the Crab nebula when KM3NeT has operated for 10 years but even these seven hours of γ-ray data is producing flux points with much higher significance than the KM3NeT data set. The model assumed in this analysis is a Pion Decay Kelner06 model (compare section 4.5) with a Log Parabola proton spectrum such that the γ-ray prediction of the model is matching the

H.E.S.S. flux points:

$$\Phi(E) = \Phi_0 \cdot \left(\frac{E}{E_0}\right)^{-\alpha-\beta\log(E/E_0)} \tag{5.6}$$

with the amplitude $\Phi_0 = 2.66 \cdot 10^{38}\,1/\text{eV}$, the reference energy $E_0 = 1\,\text{TeV}$, the index $\alpha = 2.1$ and the curvature $\beta = 0.113$. The γ-ray and neutrino prediction and the H.E.S.S. flux points are shown in figure 24. This of course assumes a 100% hadronic production of all the γ-rays coming from the Crab nebula which is not what one would expect from a pulsar wind nebula. However this is just supposed to be a test case if one measures neutrino excess from a source.

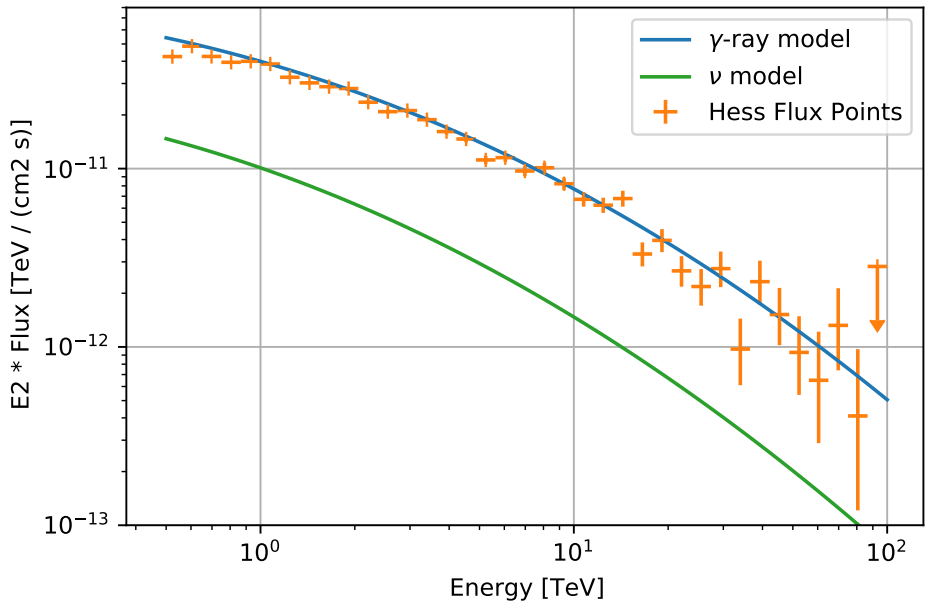

Figure 24: Input models for the Injection-Recovery-Test. The H.E.S.S. flux points (orange) are taken from the H.E.S.S. + *Fermi* analysis on the Crab presented later in this work using selected observations from all three H.E.S.S. periods. The blue and green lines show the spectra of the γ-ray and neutrino model used for the test, respectively.

The counts for both data sets are set to Poisson randomized values based on the predicted counts using the `fake` method of the data sets. The Fit of the input model to the randomized counts is shown in figure 25 and yields very consistent results to the input model. Outside the combined energy range from 1-100 TeV the fit is solely based on the neutrino data. In order to see how much each data set is contributing to the fit in the combined energy range the ΔTS-value in each energy bin is calculated for the two data sets separately. Here $TS1$ is the TS-value with the best-fit source model and $TS0$ with the source model amplitude equal to zero. The square root of the difference of these values can be seen in the right panel of figure 25 which shows that the CTA data set dominates the fit. As a conclusion one can say that a combined analysis with GAMMAPY is possible and the input model can be recovered. However in reality is does not make much sense to include the neutrino data in the fit if one just wants to fit a spectrum since this will always be dominated by the γ-ray data. But the same γ-ray data can also be explained by a leptonic production mechanism e.g. an Inverse Compton model. The goal of the next section is to estimate how much the neutrino data can help to distinguish between a hadronic and leptonic production mechanism of the γ-ray data.

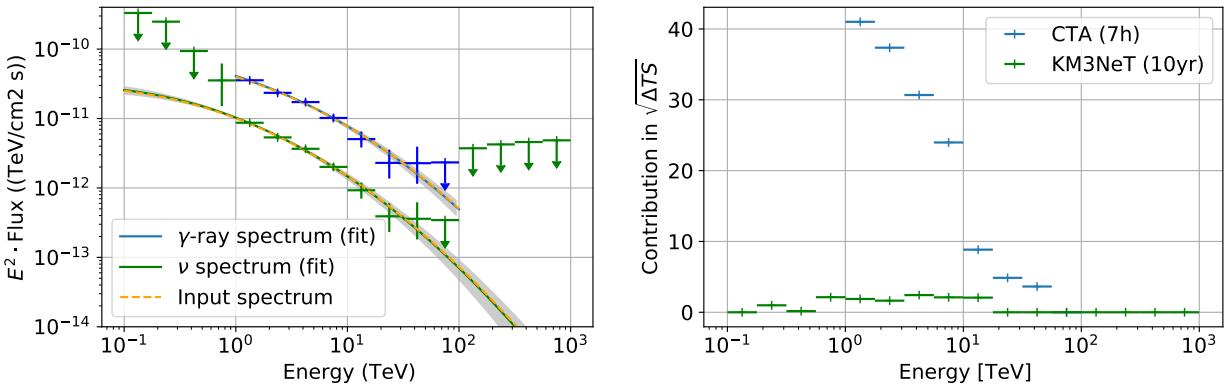

Figure 25: *Left:* The fitted spectra and flux points of the combined fit, in blue for the γ-rays and in green for the neutrinos. The orange dashed lines show the input models for the respective cases. A flux point is indicated as upper limit if its significance is smaller than 2σ. *Right:* The $\sqrt{\Delta TS}$-value for each flux point calculated separately for the CTA and KM3NeT data sets (blue and orange points respectively). This shows how much each data set is contributing to the fit in each of the energy bins.

5.2.3 Limits on the hadronic contribution

In this section a combined analysis will be used to estimate the possibility to differentiate between a hadronic and leptonic production scenario for the two sources Vela X and RX J1713.7−3946. While Vela X is a pulsar wind nebula similar to the Crab and leptonic models of the γ-ray production are preferred, the possibility of a small hadronic contribution to the γ-ray flux is not unreasonable. For the young supernova remnant RX J1713.7−3946 there is an still ongoing debate about the origin of the γ-radiation. In any case the two scenarios of 100% leptonic and 100% hadronic production are modeled for both sources and the exclusion probabilities for the disfavored case are calculated.

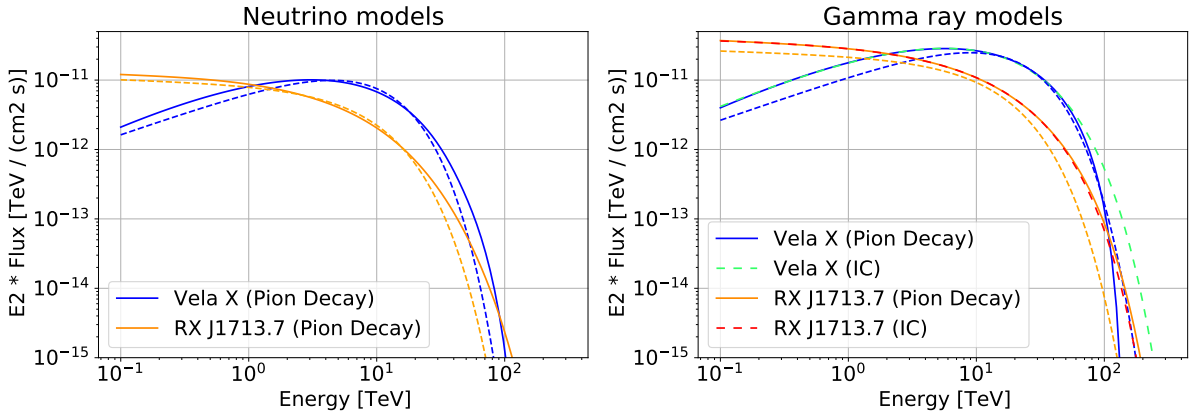

Figure 26: *Left:* The solid lines show the neutrino prediction of the Pion Decay Kelner06 models for the sources Vela X and RX J1713.7−3946. They have been fitted to the dashed lines which show the expected neutrino spectra from figure 22. *Right:* The solid blue and orange lines show the γ-ray prediction of the same Pion Decay Kelner06 models from the left panel. The dashed lines of the same color show the spectra used to model Vela X and RX J1713.7−3946 in the CTA 1-dc for comparison. The dashed lines in bright green and red show the Inverse Compton models which are fitted to the Pion Decay models. The parameters of the electron/proton spectrum can be found in table 2.

The input models for the two sources are shown in figure 26, where the neutrino prediction of an exponential-cutoff power-law (equation 4.2) proton spectrum has been fitted to the neutrino models used in Aiello et al. (2019). One can see that the Pion Decay models can not quite reproduce the curvature of the cutoffs. The γ-ray prediction of these models is also in the same range as the models used in the CTA first data challenge (1-dc) to model the two sources. For the leptonic scenario an Inverse Compton model with an exponential-cutoff power-law electron spectrum scattering on the CMB is fitted to the Pion Decay model. The parameters for the electron and proton populations can be found in table 2. Even though these models are not as realistic as models which are directly based on γ-ray observations it is good enough in the context of this work. The important points for this analysis are to have a realistic neutrino flux expected for 100% hadronic γ-ray production at the source and two γ-ray models that are so similar that CTA alone can not distinguish between them with large significance. The spatial models are the same used in the sensitivity study in section 5.2.1 for the neutrino models. This is a big simplification for the CTA data sets which are expected to resolve also the spatial shape of these sources. However this study is rather insensitive to the spatial models of the CTA data set because with the observation times assumed here the detection significance is high enough. All the parameters of the models can be found in table 2.

Table 2: Model parameters for the electron/proton particle distributions used for this study. The flux is parameterised according to equation 4.2 with $E_0 = 1\,\mathrm{TeV}$.

Source (model)	radius [°]	A [eV^{-1}]	Γ	E_{cut} [TeV]	β
RX J1713.7−3946 (electron)	0.6	$3.784 \cdot 10^{35}$	3.04	71.66	1.597
RX J1713.7−3946 (proton)	0.6	$2.623 \cdot 10^{37}$	2.143	131.2	2.003
Vela X (electron)	0.8	$2.455 \cdot 10^{32}$	1.334	37.05	1.156
Vela X (proton)	0.8	$3.027 \cdot 10^{34}$	1.004	151.7	91.8

The KM3NeT data sets were generated as explained in section 5.1.4 with observation times of 2.5, 5 and 10 years. The CTA data sets were generated from observations simulated in the CTA 1-dc (45 on Vela X, 114 on RX J1713.7−3946) with the exposure and background model normalization rescaled according to 50, 100 and 200 hours of observation time. The energy range of the data sets is set from 100 GeV to 100 TeV with 8 bins per decade. The true energy axis has twice as many bins and a background oversampling factor of 2 is used. The region of interest (RoI) is chosen with 6×6 square degrees and 0.02 degree spatial binning.
For each source two scenarios are tested, one where the counts of both data sets are set to a 100% hadronic scenario where the γ-ray and neutrino counts are given by the Pion Decay model plus background. In the other scenario assuming 100% leptonic production the γ-ray counts are given by the Inverse Compton model plus background and the neutrino counts are only background counts. For both scenarios 100 Poisson randomized realizations are drawn based on the input models. For each of the 100 data sets the profile likelihood scan of the hadronic contribution f is performed. This is done by assigning both the Pion Decay and the Inverse Compton model to the data set and setting the amplitude A_{Pion} to $A_{0,\,\mathrm{Pion}} \cdot f$ where $A_{0,\,\mathrm{Pion}}$ is the amplitude of the input model and the amplitude of the Inverse Compton model A_{IC} to $A_{0,\,\mathrm{IC}} \cdot (1 - f)$. The $TS0$ values are calculated for 20 linear spaced values of f in the range from 0 to 1 for both data sets. The figures 27 and 28 show the ΔTS-values averaged over the 100 realizations where the $TS1$ value is calculated for the models equal to the input models. The

90% confidence intervals on the hadronic contribution are calculated as described in section 4.3 for the three cases indicated in the figures.
The interpretation of the figures could be that for the hadronic scenario of Vela X the contribution of hadronic γ-ray production can be constrained to over 72% with 90% confidence assuming 100 h of CTA data and 5 y of KM3NeT data. In the leptonic case f could be constrained to

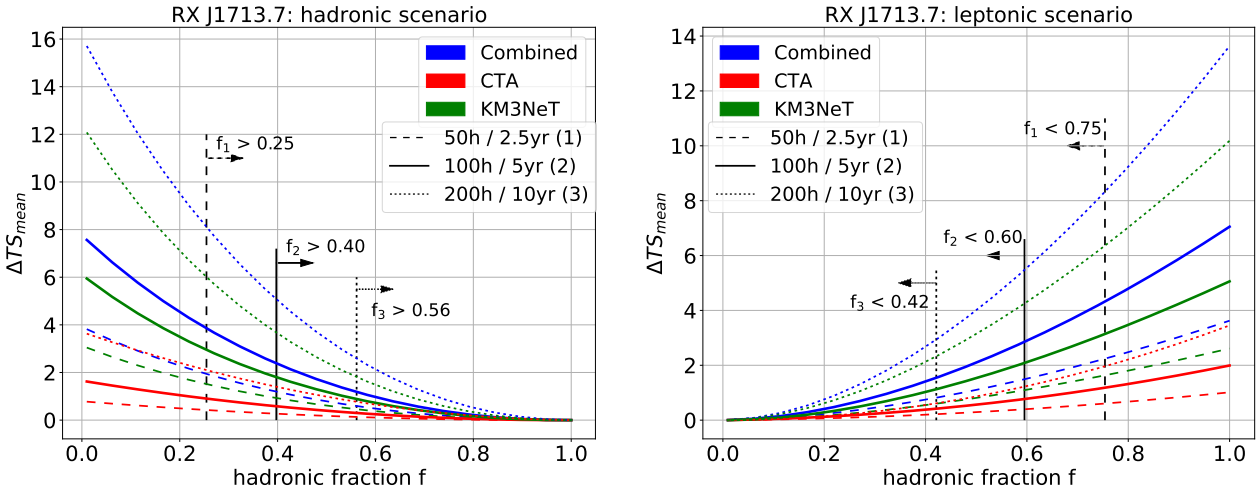

Figure 27: Profile likelihood scan for the source RX J1713.7−3946. The scanned parameter is the hadronic contribution f which is basically the normalization of the Pion Decay component. ΔTS_{mean} is the mean ΔTS-value averaged over 100 Poisson based realizations of the input model. The red and blue curves show the contributions of the CTA and KM3NeT data sets to the combined curve (blue), respectively. The different line styles denote different observation times used to crease the pseudo experiments, where scenario (1) is 50 hours of CTA observation together with 2.5 years of KM3NeT observation, scenario (2) is 100 hours and 5 years and scenario (3) is 200 hours and 10 years. The black bashed lines and arrows indicate the 90% confidence intervals (calculated according to section 4.3) of the hadronic contribution for the different scenarios. The exact intervals can also be found in table 4. *Left:* The input model is 100% hadronic which means that the counts of both data sets are given by the Pion Decay model plus the background component. *Right:* The input model is 100% leptonic which means that the counts of the CTA data set are based on the IC model plus background and the counts of the KM3NeT data set are only due to the background model.

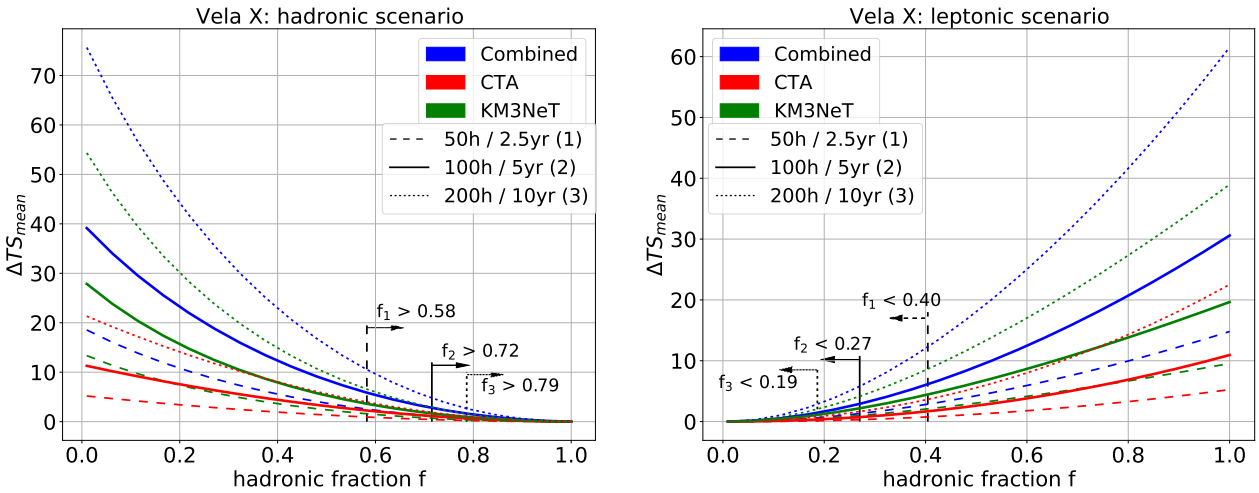

Figure 28: Profile likelihood scan for the source Vela X. For details see figure 27.

below 27% given these observation times. For RX J1713.7−3946 these limits are weaker with above 40% and below 60% for the hadronic and leptonic scenarios, respectively. From the ΔTS curves one can see that the neutrino data sets are contributing most to these limits because their curve is rising more quickly.

One problem with the interpretation of these results is that the models were not optimized for each step during the scan. This means that the slope of the CTA curves are mostly given by the quality of the pre-fit of the IC model to the PD model. If the Pion Decay and Inverse Compton models would give exactly the same prediction in each energy bin the ΔTS curve of the CTA data sets would be flat since one could not distinguish between the models just using the γ-ray data. The optimization of both models at the same time was also attempted but caused some problems to the fit because of the almost perfect degeneracy between the models. Since f is not a direct parameter in the fit one needs a work around to effectively scan the hadronic contribution while giving both models as much freedom as possible. Two possible solutions will be described in the updated results.

5.3 Updated results

Compared to the initial results the following improvements of the analysis have been implemented. First the new CTA IRFs are used here together with the corresponding generation of CTA data sets as described in section 5.1.4. However this is not expected to have a big impact on the analysis itself. For the KM3NeT data sets the atmospheric muon background component is added and a simple optimization of the quality cuts was attempted. For both sources Vela X and RX J1713.7−3946 the spectral models used for this analysis are now directly fitted to the latest H.E.S.S. flux points. But the main difference is that both models are optimized during the scan of the hadronic contribution.

5.3.1 Optimization of quality cuts for the muon background

Because the atmospheric muon background consists of falsely reconstructed events a separation of signal events to background events is attempted using the reconstruction likelihood which is a measure of the goodness of reconstruction for each event. Looking at the distributions in figure 29 one can see that for large zenith angles the likelihood for falsely reconstructed muons is decreasing. This is the case because only few events are reconstructed in a completely different direction with high likelihood. For the neutrinos the distribution is only weakly dependent on the zenith angle. In order to cut most muon events while keeping as many neutrino events as possible four different cuts on the likelihood dependent on the zenith angle θ have been investigated with respect to the resulting point source sensitivity. The cuts (illustrated in figure 29) are applied in addition to the standard ones from section 5.1.1 and follow the linear equation

$$\text{likelihood}(\theta) > A - 140 \cdot \theta \tag{5.7}$$

where A was chosen to be 330, 380, 430 and 530 for the cuts 1, 2, 3 and 4, respectively. The first cut is only removing additional events up to a zenith angle of ∼105° while the fourth cut removes almost all muon events but also about 80% of the neutrino events. The discovery potential of KM3NeT with each of these cuts is calculated as described in section 5.2.1 and compared to the discovery potentials without the muon background in figure 30. As expected the sensitivity of KM3NeT decreased when including the additional background model. The quality cut resulting in the best sensitivity is dependent on the source and decreases the sensitivity by 10 - 15 % compared to the sensitivities without the muon background. For Vela X and RX J1713.7−3946 the best results are obtained with the least strong cut 1 which will also be used in the following

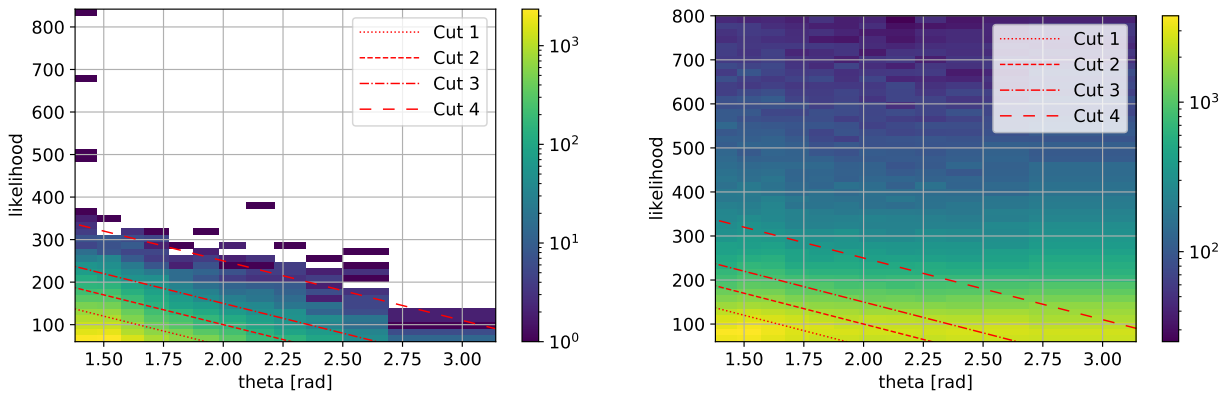

Figure 29: 2D histograms of the reconstruction likelihood vs the zenith angles for muon simulations (*Left*) and neutrino simulations (*Right*) after the standard quality cuts (comp. sec. 5.1.1) are applied. The red lines indicate the zenith angle dependent cuts on the likelihood that were attempted to suppress the muon background.

sections.
One problem with the stronger cuts is that they also cut away a large fraction of the neutrinos which are used to generate the IRFs. This means that especially for low zenith angles where the cuts are the strongest and the highest energies where the statistic gets worse there are more and more null entries in the histograms of the IRFs. These cause discontinuities in the IRFs and unexpected behaviour which might also be a reason why the sensitivity becomes much worse for the fourth cut. In order to also test these stronger cuts effectively one would either need more simulations or smooth the IRFs.

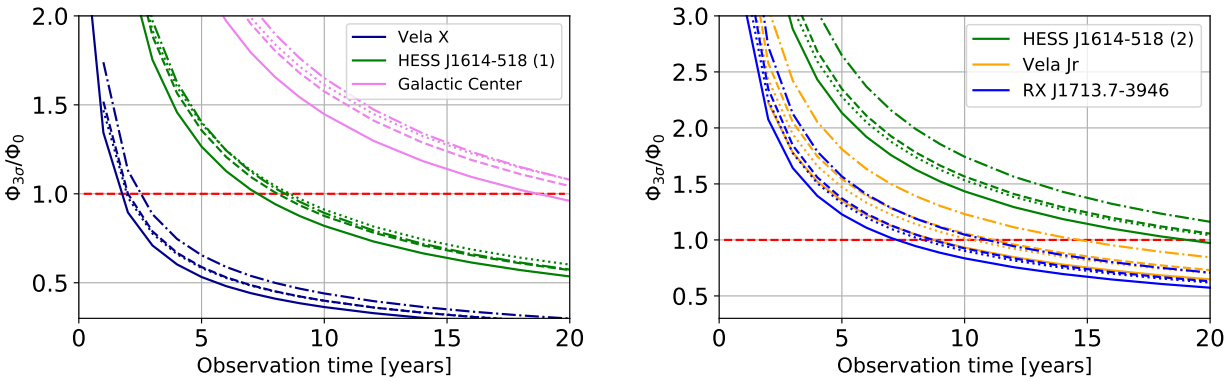

Figure 30: Ratio of the 3 sigma discovery potentials $\Phi_{3\sigma}$ to the expected neutrino fluxes Φ_ν for the different quality cuts. The solid lines show the comparison without the muon background (dashed lines in figure 23). The results for the cuts 1 (dotted), 2 (dashed) and 3 (dash-dotted) are shown while the result for the cut 4 is not shown because it is much worse compared to the other cuts and would require a larger y-scale.

In KM3NeT analyses a special Boosted Decision Tree (BDT) training is employed for each source spectrum based on more reconstruction parameters. For some spectra the rejection of muon background can be good enough that the discovery potential almost matches the one calculated without the atmospheric muon background (Kay Graf, private communication). However this requires dedicated BDT training which is beyond the scope of this thesis. Based on the discovery potentials calculated here it is possible to achieve similar detection significances using a more sophisticated analysis in just 62% of the observation time simulated in this work for Vela X. For

RX J1713.7−3946 one needs 66% less observation time to obtain the same results in a KM3NeT analysis. This should be taken into account when interpreting the results from section 5.3.3.

5.3.2 Generation of new models

For more realistic spectral models of Vela X and RX J1713.7−3946 a Pion Decay model (Kelner06) and an Inverse Compton model (NAIMA) are fitted to the latest H.E.S.S. flux points of each of the sources. An exponential-cutoff power-law model (compare equation 4.2) is assumed for the proton/electron spectra but in contrast to the models used in section 5.2.3 the cutoff strength β is fixed at 1. This is because the ultra hard cutoff of the proton spectrum causes discontinuities in the variation of the γ-spectrum when smoothly varying the cutoff energy. This is an artifact caused by the numerical integration over the proton energies which leaves the γ-flux unchanged when varying the cutoff energy in a certain interval. This is not a problem as long as the cutoff energy is not a free parameter in the fit. However if it is the likelihood landscape is no longer smooth which causes problems for the fit. The best-fit γ-ray spectra for both sources can be seen in figure 31 and the corresponding parameters can be found in table 3. Note that in order for the proton spectrum to produce the hard cutoff in

Table 3: Model parameters for the electron/proton particle distributions fitted to the H.E.S.S. flux points. The flux is parameterised according to equation 4.2 with $E_0 = 1\,\mathrm{TeV}$.

Source (model)	radius [°]	A [eV^{-1}]	Γ	E_{cut} [TeV]	β
RX J1713.7−3946 (electron)	0.6	$1.56 \cdot 10^{35}$	2.74	49.3	1
RX J1713.7−3946 (proton)	0.6	$1.48 \cdot 10^{37}$	2.00	112.3	1
Vela X (electron)	0.8	$2.21 \cdot 10^{31}$	0.577	23.7	1
Vela X (proton)	0.8	$1.00 \cdot 10^{28}$	-3.37	19.0	1

the γ-ray spectrum it needs a very hard index of -3.37 (compare equation 4.2). This causes the spectrum to increase up to an energy of ∼70 TeV, far above the cutoff energy of 19 TeV. Above 100 TeV the exponential-cutoff term dominates and the spectrum shows a hard cutoff. Even though such a proton spectrum would need roughly a thousand times more energy than the corresponding electron spectrum to produce the same γ-spectrum and is physically highly unlikely, the corresponding Pion Decay model can describe the H.E.S.S. flux points almost equally good as the Inverse Compton model. For RX J1713.7−3946 the Inverse Compton model is also able to describe the H.E.S.S. data a little bit better than the Pion Decay model however the parameters are more in the expected range. The spatial models do not change compared to the sections before.

5.3.3 Improved scan of the hadronic contribution

There are two main options of scanning the hadronic contribution while simultaneously fitting both spectral models. The first one is to freeze the amplitude A of either model to a fraction of its best-fit value A_0, obtained from a fit when excluding the other model. For each value of the hadronic contribution f in the range from 0 to 1 the amplitude is frozen to the value $A = f \cdot A_0$. For the optimization at each value of f the other model's parameters should also be set to the best-fit values with the amplitude $A' = (1 - f) \cdot A'_0$. One also needs to set bounds for the free parameters, especially for the index and cutoff energy. The reason behind this is that

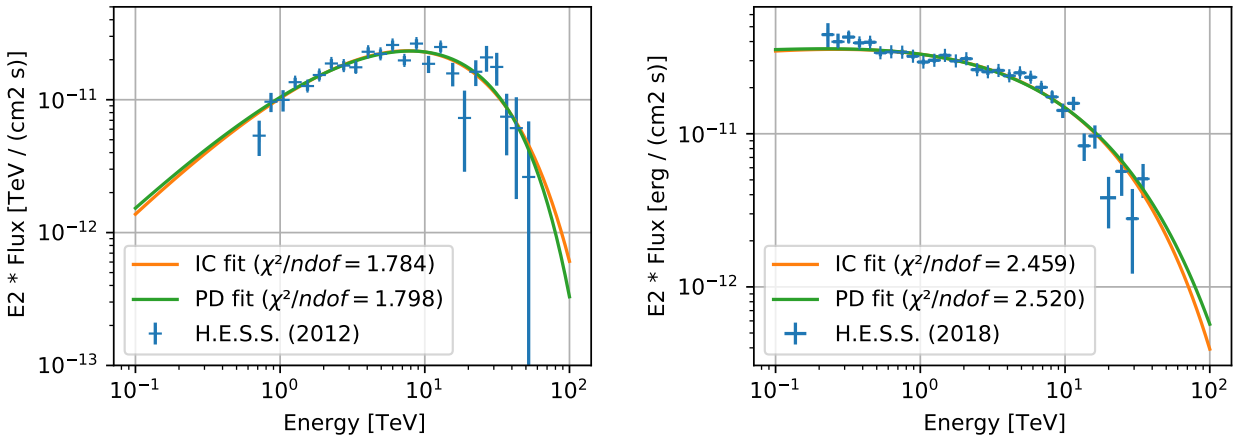

Figure 31: *Left:* H.E.S.S. flux points from Abramowski et al. (2012) and the best-fit Inverse Compton (orange) and Pion Decay (green) model for Vela X. In the legend the χ^2-value divided by the number of degrees of freedom is shown as a measure for the goodness of the fit. *Right:* Same plot for RX J1713.7−3946 with the H.E.S.S. flux points from Abdalla et al. (2018).

the contribution of a model can be entirely suppressed by fitting a very soft index or very low cutoff energy.

However this method has some problems. Since the protons and electrons at one energy produce γ-rays in a wide range of energies one has only very limited control over the γ-ray spectrum by fixing the primary particle spectrum's amplitude at one energy. This enables the fit to strongly prefer the input spectrum independent on the value of f. When the amplitude of the PD model is fixed corresponding to $f = 0.2$ in the hadronic scenario it is very well possible that the integral over the fitted models corresponds to 60 % hadronic contribution to the overall γ-ray flux. Because of this it is hard to scan the values of f for the opposite scenario where the TS-values become higher compared to the input scenario. In order to improve this method it is advisable to chose the reference energy E_0 of the models in a range that affects the γ-ray flux around 1 TeV the most. For the Inverse Compton model (only CMB as seed photon field) this energy should be chosen around 17 TeV while for the Pion Decay model (Kelner06) the proton energies mattering the most are between 30 - 200 TeV. It is in principle possible to calculate reasonable ΔTS-curves with this method however the result strongly depends on the bounds for each free parameter. It also depends on whether one scans the IC amplitude or the PD amplitude because the corresponding model effectively looses one degree of freedom since its amplitude is frozen.

For these reasons an alternative approach based on prior functions is used here. The hadronic contribution of the models is calculated based on the integrals I over the γ-ray flux $\phi(E)$

$$I = \int_{0.1\,\mathrm{TeV}}^{100\,\mathrm{TeV}} \phi(E)\, dE \tag{5.8}$$

The value of the hadronic contribution f follows as

$$f = \frac{I_{\mathrm{PD}}}{I_{\mathrm{PD}} + I_{\mathrm{IC}}} \tag{5.9}$$

For the fit one can add a penalty term to the TS-value based on deviations of f from the value f_{scan} one wants to scan. In this work a Gaussian potential has been chosen which leads to a

total TS-value of

$$\mathrm{TS}_{total} = \mathrm{TS} + S \cdot \frac{(f - f_{san})^2}{\Delta f^2} \tag{5.10}$$

The combination of the scaling factor S and the uncertainty Δf allows for different variations from the scan value f_{scan}. For the results presented here $S = 1$ and $\Delta f = 1\%$ is chosen. The spectral parameters of both models can be left free in this approach and no bounds for the parameters are needed. During the scans the cutoff strength β is also left free however limited in a range of [0.5,2] because of the problem with hard cutoffs discussed in section 5.3.2.

In the following part the results for three test scenarios will be compared with each other. In *Scenario 1* only knowledge of the CTA data is assumed and different combinations of the models are scanned using the prior function described above. For each value of f_{scan} both models are optimized and the ΔTS values show how well CTA can differentiate between hadronic and leptonic emission scenarios by itself.
In *Scenario 2* a scan is performed on KM3NeT data under the knowledge of the CTA spectrum including its uncertainties. This is implemented in a way that the PD model is fitted to the CTA data including an error estimation. The parameters P_{CTA} of the best-fit proton spectrum are used to calculate the neutrino flux prediction. A prior function is added to the TS-value of the KM3NeT data set for all parameters P in $[A, \Gamma, E_{\mathrm{cut}}, \beta]$:

$$\mathrm{TS}_{total} = \mathrm{TS} + \sum_{P} \frac{(P - P_{\mathrm{CTA}})^2}{(\Delta P_{\mathrm{CTA}})^2} \tag{5.11}$$

In order to perform the scan over different hadronic contributions the value A_{CTA} of the best-fit amplitude and the corresponding uncertainty are scaled by f. This method allows for small variations of the neutrino spectrum within the uncertainty of the CTA spectrum. Note that for $f = 0$ one cannot scale the error to 0 but instead a negligible small error is used.
For *Scenario 3* the prior functions of the KM3NeT data set are removed and the scan is performed including the CTA data set. Similar to scenario 1 the scan is performed using the prior function on f while both models are optimized for both data sets simultaneously. This scenario corresponds to the combined fit where the low level data from both instruments is available.
For the results presented here 100 Poisson randomizations are drawn for three different emission scenarios, a completely leptonic scenario, a completely hadronic scenario and a mixed scenario where the counts are based on 50% PD model and 50% IC model. For each of the realizations both models are individually fitted to the CTA data, first using the `scipy` backend implemented in Gammapy which seems to find lower minima compared to the `minuit` backend in most of the cases. However it does not respect parameter bounds and cannot estimate the errors of the parameters. That is why in a second step the minima are validated and the errors are estimated using the `minuit` backend with the starting parameters from the first optimization. The three scans for the three different scenarios are performed with the `minuit` optimizer which was found to be more stable once the starting parameters are set close to the minimum. The resulting profile likelihood scans can be seen in figure 32 for the sources RX J1713.7−3946 and Vela X. The ΔTS-values of each of the three test scenarios are averaged over the 100 realizations and do not include the contribution of the prior function. For each of the averaged ΔTS-values the corresponding hadronic fraction is calculated with equation 5.9 using the averaged integrals corresponding to that ΔTS-value. The 90% confidence intervals are obtained by integrating $\exp(-\Delta TS/2)$ as described in section 4.3. The distribution of ΔTS-values can be seen for the hadronic emission scenario for Vela X showing that for some realizations the ΔTS-value exceeds 70 while for others it remains below 25. The distributions for the other cases were also checked

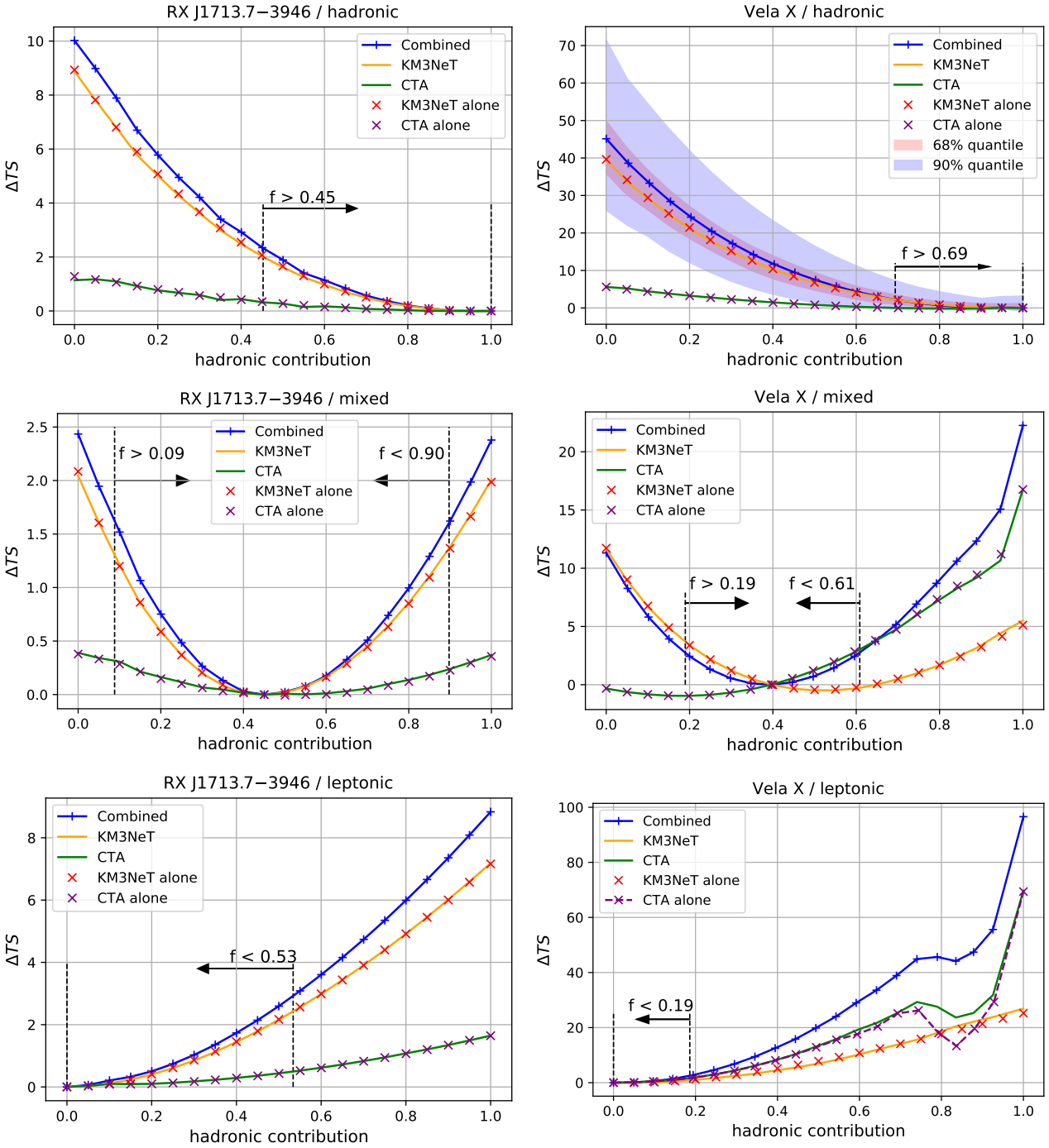

Figure 32: Profile likelihood scans of the hadronic contribution with the 90% confidence intervals indicated as dashed vertical lines. On the left hand side the results for RX J1713.7−3946 can be seen for the emission scenarios 100% hadronic, 50% hadronic/50% leptonic (mixed) and 100% leptonic with 200 hours of CTA data and 10 years of KM3NeT data. The same results are shown for Vela X on the right hand side. The solid blue lines show the averaged ΔTS-value for the combined fit where the markers indicate the scanned values (scenario 3). The solid orange and green lines show the contribution of the KM3NeT and CTA data set to the combined ΔTS-value, respectively. The red and purple markers show the ΔTS-values obtained for the scenarios 2 and 1 ,KM3NeT alone (knowing the CTA spectrum) and CTA alone. For the hadronic case of Vela X the distribution of the "combined" ΔTS-values is additionally shown as 68% and 90% quantiles.

for smoothness and outliers but are not reported here since they are not used for the calculation of the confidence intervals.
One can see that for all scans except the leptonic scenario of Vela X the ΔTS values of the scenarios 1 and 2 agree very well with the respective contribution to the combined ΔTS value. This means that in most of the cases the combined fit would not give any different limits on the hadronic contribution compared to the manual summation of the separate scans. Note however that the Pion Decay models and also the values of hadronic contribution at each step of the scan vary slightly between the separate scans. This means that simply adding them is not fully consistent. In future analyses one might also fit the spatial component of the models which can also be used by CTA to discriminate between the emission scenarios in some cases. By using the combined fit one ensures consistency in each scan step between all free model components. For the leptonic scenario of Vela X the CTA data set contributes more to the ΔTS values than the KM3NeT data set. This is in contrast to all the other scans but can simply be explained by the fact that the Pion Decay model is not able to describe the counts which are based on the Inverse Compton model very well. Especially when scanning the CTA data set alone the fit finds combinations of the two models around a hadronic contribution of 0.8 which are clearly preferred to the input models but still have the right ratio to each other. This is a sign that the fit is working well and not just remaining at its starting parameters but finding different minima. For this case the influence of the prior function on the fit was tested by scaling the factor S in equation 5.10 in front of the prior function. For a factor $S = 4$ the scan changed mainly for the higher ΔTS-values, shifting the dip at $f = 0.8$ slightly to the left and resulting in a 90% confidence limit of $f < 0.17$. For smaller S equal to 0.25 and 0.1 the fit did not produce the smooth dip at 0.8 but instead a sharper dip at 0.95. The influence of the prior function needs to be investigated further and probably adjusted for each set of observations in order to obtain the maximally optimized result. However as far as tested here the prior function only influences the limits within a 2% margin, even less for the more parabolic curves. For RX J1713.7$-$3946 the γ-ray components of the two models are able to imitate each other better compared to the models of Vela X. This results in lower contributions from the CTA data set and stresses the benefit of including KM3NeT data.
Since the scans are only performed for 200 hours of CTA data and 10 years of KM3NeT data the ΔTS curves are scaled by a factor of 1/2 and 1/4 in order to calculate the limits for the other observation times. Previous tests have shown that this is valid and can be justified since the IRFs remain the same where only the exposure is scaled by the same factor. The limits are compared to the limits obtained in the initial results in table 4. For all cases except the leptonic scenario of Vela X the limits for the updated results are not as strong. This has two main reasons. The first is that the KM3NeT sensitivity is lower compared to the initial results because of the inclusion of the muon background. The second reason is the usage of new models which are optimized during each scan step which is lowering the ΔTS value of the CTA data sets. For the leptonic emission scenario of Vela X the Pion Decay model is simply not able to describe the Inverse Compton counts which is reasonable because the actual emission scenario of Vela X is probably mainly leptonic and both models are based on the latest H.E.S.S. data now. For the initial results the Inverse Compton model was also based on a hadronic parametrization of the γ-ray flux which made it easier for the PD model to describe the IC counts.
Note when interpreting these results that similar ΔTS-curves for KM3NeT can be achieved in just 62% (for Vela X) and 66% (for RX J1713.7$-$3946) of the observation time simulated here by assuming the published KM3NeT sensitivity. The ΔTS curves for CTA also depend on the models used in this analysis. They could be further lowered by giving the primary particle spectra more freedom or adjusting the prior function which helps the fit to find the best minimum in some cases. On the other hand the ΔTS-values might also be increased by including the spatial component of the models in the fit. More sophisticated models could make

predictions on the morphology of the source dependent on the primary particle distribution. CTA might be sensitive to the different morphologies caused by different cooling of different particles. First simulations on resolving the morphology of the Crab nebula performed by Mestre et al. (2019) yield promising results for the characterisation of the γ-ray emission. Independent on the exact setup of the analysis one can conclude that the combination of CTA and KM3NeT data will be a promising approach to discriminate between hadronic and leptonic emission scenarios for galactic γ-ray sources.

Table 4: Summary table of the 90% confidence intervals of the hadronic contribution for the sources RX J1713.7−3946 and Vela X. The intervals obtained in this section (updated results) and for comparison also the intervals for the initial results (section 5.2.3) are given in per cent. Observation time [1] corresponds to 50 hours of CTA data and 2.5 years of KM3NeT data. The observations times [2] and [3] correspond to 100 h / 5 yrs and 200 h / 10 yrs, respectively.

Source (scenario) [observation time]			90% confidence intervals [%]	
			updated results	initial results
RX J1713.7−3946	(leptonic)	[1]	0 - 82.0	0 - 75.4
		[2]	0 - 71.4	0 - 59.5
		[3]	0 - 53.4	0 - 42.1
	(mixed)	[1]	5.7 - 93.8	–
		[2]	6.6 - 92.6	–
		[3]	8.8 - 89.7	–
	(hadronic)	[1]	19.6 - 100	25.5 - 100
		[2]	30.3 - 100	39.7 - 100
		[3]	45.3 - 100	56.1 - 100
Vela X	(leptonic)	[1]	0 - 36.4	0 - 40.4
		[2]	0 - 25.9	0 - 27.0
		[3]	0 - 18.6	0 - 18.6
	(mixed)	[1]	4.9 - 78.3	–
		[2]	11.6 - 69.6	–
		[3]	19.0 - 60.9	–
	(hadronic)	[1]	46.3 - 100	58.2 - 100
		[2]	59.4 - 100	71.5 - 100
		[3]	69.4 - 100	78.6 - 100

Discovery follows discovery, each both raising and answering questions, each ending a long search, and each providing the new instruments for a new search.

(J. Robert Oppenheimer, "Prospects in the Arts and Sciences")

6. Combined analysis of H.E.S.S. and *Fermi* on the Crab nebula

As described in section 2.2.1 the Crab nebula is the brightest steady TeV γ-ray source and thus best suited to study its spectrum and morphology in detail. In order to model the spectral energy distribution (SED) previous works have already combined the flux points of different instruments to fit a physical model to it [Yuan et al., 2011], [Meyer et al., 2010]. In this work a new analysis method is tested which combines the latest low-level γ-ray data measured by *Fermi* and H.E.S.S. in a Gammapy 3D analysis. One advantage of this method is that it ensures consistency between the analyses of different instruments e.g. that the flux is coming from the same region. Also the extension of the Crab has been determined by different instruments in different energy bands using however different analysis methods [Yeung and Horns, 2019]. This can also be done in a more consistent way using Gammapy. The goal of this section is the proof of concept for a combined analysis at the likelihood level of H.E.S.S. and *Fermi* data. A SSC model (sec. 4.5) as well as the energy dependent morphology will be fitted to the data of the two instruments.
First the *Fermi* and H.E.S.S. data will be analysed separately and compared with the standard analysis tool to check for consistency with the Gammapy analysis. Then the data sets will be combined. Additional details about the analysis can also be found on the HESS confluence page[18].

6.1 H.E.S.S. data and comparison to the HAP analysis

In order to only use observations with good data quality for this analysis the following selection cuts have been applied [L. Mohrmann (private communication)]

- Zenith $\leq 55^\circ$
- Offset $\leq 1^\circ$
- No outliers in tracking and star pointing

For the HESS-I data set this additional cuts are applied

- Run ID $> 20\,000$
- Do not use runs taken during mirror replacement campaign
- Do not use runs that were rejected for the Crab extension measurement (unless they were rejected due to the stricter offset cut)

[18] https://hess-confluence.desy.de/confluence/pages/viewpage.action?pageId=122388494

For the HESS-IU data set the runs 135270, 135271 and 142760 were rejected in addition because they show unstable trigger rates. The run lists themselves can be found in Appendix A and the cumulative live time for each season is listed in table 5.

Table 5: Number of the runs and the corresponding live time for the run lists for the three H.E.S.S. seasons. Note that the live time is not corrected for the dead time.

	number of runs	live time [h]
HESS-I	64	28.8
HESS-II	50	21.4
HESS-IU	62	28.0

The data only includes CT 1-4 because there is no background model computed for the combination with CT5, yet. For the event reconstruction the ImPACT algorithm [Parsons and Hinton, 2014] is used which offers a better spatial resolution compared to the traditional reconstruction based on the *Hillas* parameters [Hillas, 1985]. For each of the runs a low energy threshold is determined by choosing the maximum of the energy dispersion bias threshold or the background model rate threshold. The first one is set to the energy where the average reconstructed energy of the events is 10% above their true energy. This is more and more the case for low energy events since only those are detected where the reconstruction algorithm systematically over predicts the energy. The energy dispersion bias is calculated at an offset of 1.5° which is the maximal offset of the spatial mask used in this analysis. The second threshold value is connected to the background model used in the 3D analysis. The background model predicts the rate of hadronic events passing the reconstruction which depends on energy, zenith angle and offset in the camera. It is generated by averaging over measured rates when excluding known sources. The background rates should increase with decreasing energy but because of the energy threshold of IACTs there is a maximum in the background rates spectrum below which the model can become invalid. So the background model rate threshold is the energy at which the maximum is located. For more details on the threshold computation and 3D background model generation see Mohrmann et al. (2019).
From the H.E.S.S. location the Crab can only be observed under relatively large zenith angles of $\theta \geq 44°$. This increases the lowest threshold for runs in this analysis to 0.487 TeV. In Gammapy version 0.17 the energy thresholds are not considered when stacking the IRFs of the data sets. Stacking data sets means that all the individual data sets are combined into one single data set where the exposure, counts and background rates of the individual data sets are added and the energy dispersions and PSFs are averaged (for more details see the Gammapy documentation[19]). Because of this only runs with an energy threshold in the same energy bin are stacked together. Not stacking runs at all and doing a *joint*-analysis would limit the systematics introduced by the stacking process but result in very long computing times for the *joint*-Fit. For this analysis the *semi-stacked*-analysis is chosen where the runs are stacked with the same energy threshold and a *joint*-analysis is done with these data sets. This gives 6 stacked data sets with $[56, 49, 42, 15, 8, 6]$ runs ($[7, 46, 35, 12, 8, 6]$ when excluding HESS-IU runs) being stacked for the thresholds $[0.487, 0.562, 0.649, 0.750, 0.866, 1.000]$ TeV.
Before the runs are stacked the normalization and spectral tilt of the background model is fitted for each run. For that a circular region with $r = 0.3°$ around the Crab's position is excluded and the background model is fitted to the remaining counts.
The spatial analysis geometry is 5×5 degrees with a bin size of 0.01 degrees per axis. The energy

[19] https://docs.gammapy.org/0.17/api/gammapy.datasets.MapDataset.html#gammapy.datasets.MapDataset.stack

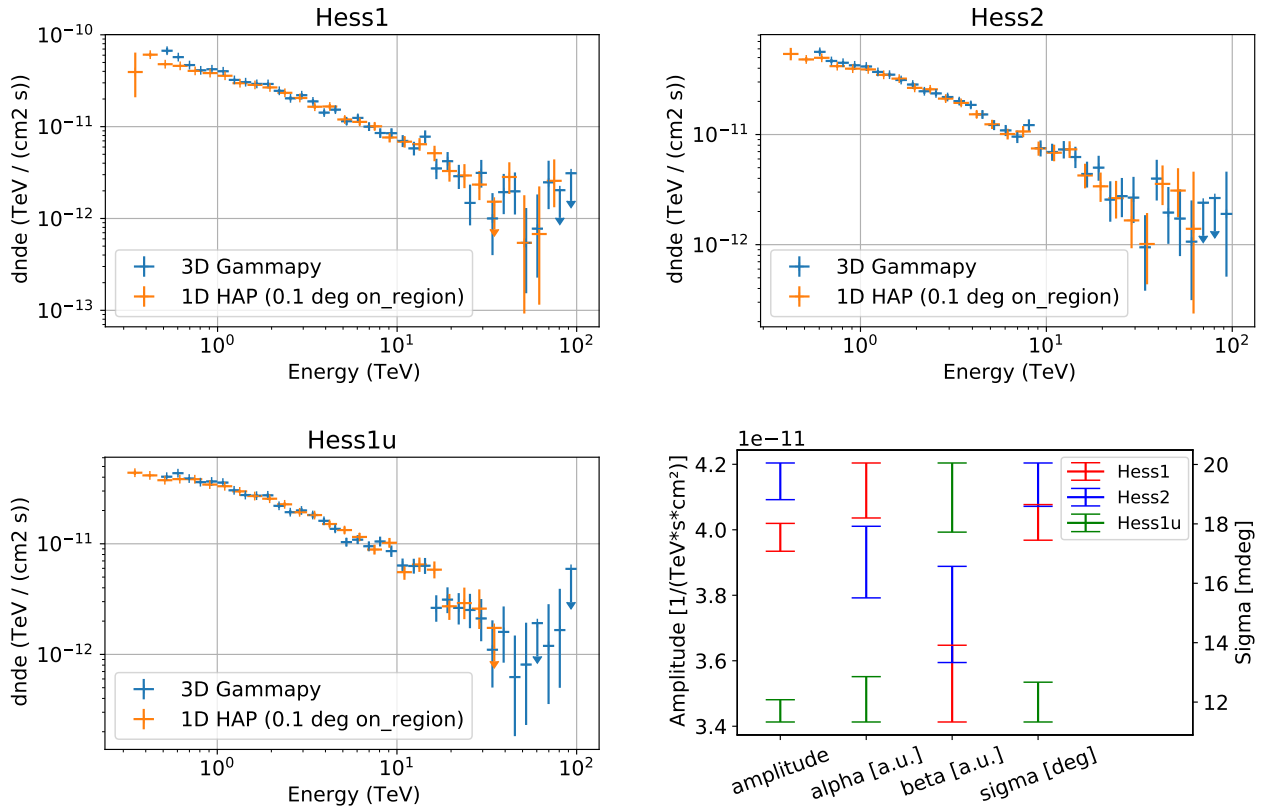

Figure 33: Results of the analysis of the separate seasons. In the first three panels the flux points of the 3D GAMMAPY analysis (blue) are compared with the flux points of the 1D HAP analysis (orange) using an on-region of 0.1 degree instead of the standard point source on-region of 0.07 degree. The fourth panel shows the best-fit parameters of the LogParabola spectral model (amplitude, alpha and beta) (eq. 4.3) and the sigma of the Gaussian spatial model (eq. 4.4).

axis is logarithmic binned between 0.1 and 100 TeV with 16 bins per decade. A *background oversampling* factor of 2 has been chosen which means that the background model is evaluated at 32 points per decade and interpolated to the energy axis grid. For each of the HESS seasons a separate analysis is done and compared with a 1D analysis performed with the HAP analysis chain by Lars Mohrmann. The source model is a 3D model with a Gaussian spatial model and a LogParabola spectral model (eq. 4.3). The results are shown in figure 33. While the spectra of the HESS-I and HESS-II period are relatively compatible the difference to the HESS-IU period is quite significant. This discrepancy is also reported by Zorn (2019) and can also be seen in the HAP analysis. For the GAMMAPY analysis the flux of the HESS-IU data sets is only at 76 % and 88 % compared to the pre-HESS-IU data sets at 0.6 TeV and 1 TeV. Above ∼3 TeV this discrepancy becomes smaller and the fluxes agree more or less between the seasons. This leads to a smaller amplitude and index for the HESS-IU spectrum but higher curvature compared to the other spectra. But not only the spectrum differs significantly between HESS-IU data and pre-HESS-IU data. Also the fitted extension of the Crab is significantly smaller for the HESS-IU data set. The correlation between the extension and the spectral parameters has been checked and is very small. This points towards some not yet understood systematic uncertainties in the IRFs of the HESS-IU season. For the combined analysis with *Fermi* data two sets of H.E.S.S. data are produced, one including HESS-IU data and an other one just including HESS-I and HESS-II data.

The other discrepancy visible in the comparison of GAMMAPY flux points and HAP flux points is

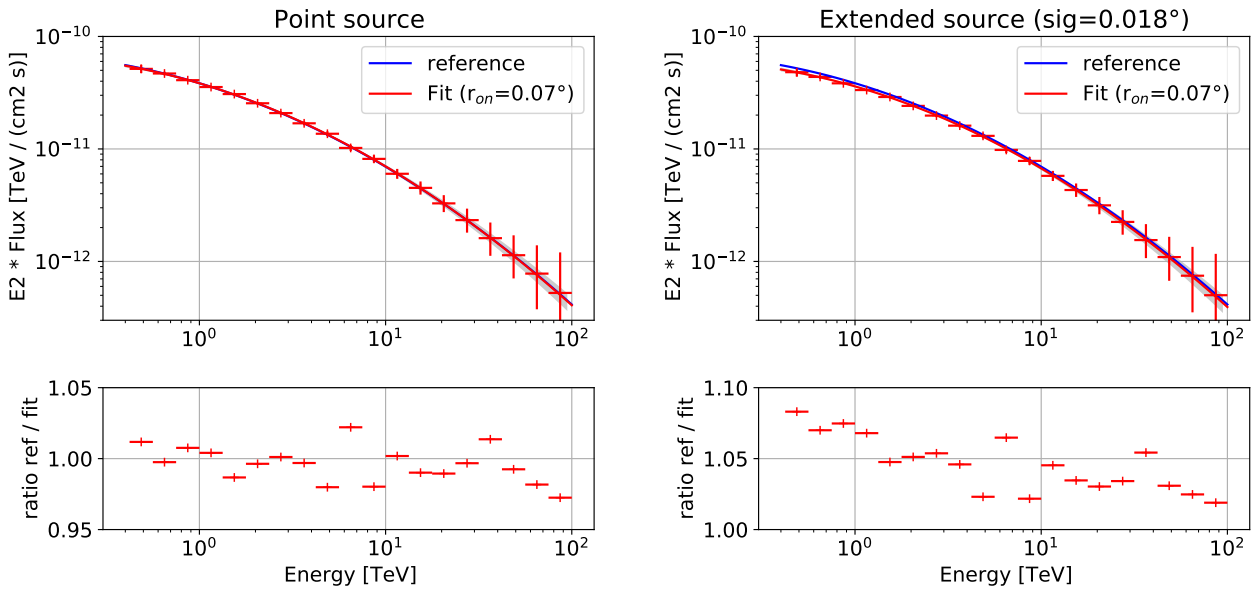

Figure 34: *Left:* Recovered spectrum (red) of a 1D reflected regions analysis with 0.07° on-region of the Crab simulated as point source compared to the input spectrum (blue). The lower panel shows the ratio of the reference spectrum to each flux point. *Right:* The same for the Crab simulated as extended source with a sigma of 0.018°.

that the flux points calculated with HAP tend to be lower at low energies. This discrepancy gets even larger when using the standard on-region for point sources in the ImPACT configuration of 0.07°. Since the Crab is extended the containment correction is not accounting for all the on-counts cut by the small on-region. To show that a simulation was performed on Asimov data sets generated with the Crab spectrum as point source and as extended source with a sigma of 0.018°. The analysis was then done as 1D analysis with reflected regions and an on-region of 0.07°, similar to a HAP analysis. In figure 34 one can see that the flux can be almost perfectly recovered for the point source but for an extended source the containment correction fails and the actual input flux is between 6 % - 9 % above the recovered one. The containment correction in GAMMAPY simply calculates the ratio of PSF containment inside to outside the on-region, while in HAP dedicated point like IRFs are used. However the same effect could be shown inside the HAP analysis, that increasing the on-region from 0.07° to 0.1° also raises the flux points at the low energies. The simulation within GAMMAPY also showed that 0.1° might not be quite enough to account for all the flux. This might also explain why the difference between HAP and GAMMAPY is more prominent for the HESS-I and HESS-II data than for the HESS-IU data where the Crab extension is a lot smaller. The remaining difference of the flux points is probably due to the different background estimation (3D background model [Mohrmann et al., 2019] vs. reflected regions estimation [Berge, D. et al., 2007]) and the different energy thresholds used for each run.

The SED obtained only using data from the HESS-I and HESS-II seasons is compared to other instruments in figure 35. One can see that the shape of the spectrum agrees well with the other instruments. This is particularly interesting because the last dedicated spectral analysis from H.E.S.S. of the Crab nebula published in 2006 [Aharonian, F. et al., 2006] indicated a cutoff above ∼20 TeV. The last flux point was well below other measurements at that time, e.g. by HEGRA [Aharonian et al., 2004]. Even though the flux point at that energy is still strangely low the high energy part of the spectrum agrees very well with recent measurements from Tibet [Amenomori et al., 2019] and HAWC [Abeysekara et al., 2019] now. For the lower energies there is a visible difference to the HEGRA flux points and also to the MAGIC [MAGIC Collaboration

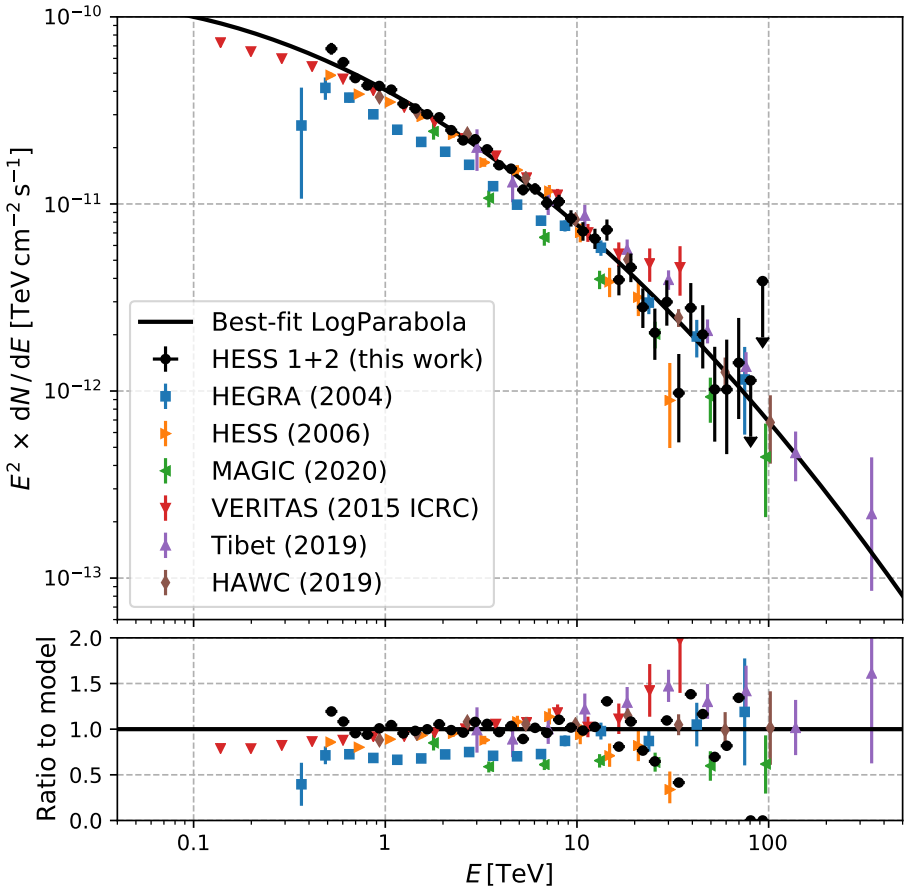

Figure 35: Comparison of the SED obtained in this work (black) using only HESS-I and HESS-II runs with the SEDs reported from other instruments. In blue the points from HEGRA [Aharonian et al., 2004], in orange the points from HESS published in 2006 [Aharonian, F. et al., 2006], in green the points from MAGIC [MAGIC Collaboration et al., 2020], in red from VERITAS [Meagher et al., 2015], in purple from Tibet [Amenomori et al., 2019] and the flux points from HAWC in brown [Abeysekara et al., 2019]. The lower panel shows the ratio of the flux points to the Log Parabola spectrum fitted to the HESS 1+2 data (parameters can be found in table 6).

et al., 2020] flux points while the agreement with VERITAS [Meagher et al., 2015] is very good. This might be because of different energy calibrations and the resulting shift in energy between the instruments.

6.2 *Fermi* data and comparison to the Fermipy analysis

For the *Fermi*-LAT analysis 11.5 years of LAT P8R3 Source data are used. The events are divided into four different PSF classes dependent on the reconstruction quality of each event. The analysis is phase resolved meaning that only the off-pulse data is analysed. The generation of the counts cubes and IRFs is done with Fermipy[20] by Manuel Meyer and read in with Gammapy resulting in four data sets of *Fermi* LAT data. The energy range goes from 1 GeV to 3.16 TeV which results in a small overlap with the H.E.S.S. energy range beginning at ∼0.5 TeV. There are eight bins per decade for the energy axis and a spatial bin size of 0.025°. In order to make the Gammapy analysis more similar to the Fermipy analysis which also includes known sources outside the RoI leaking inside it, the RoI in Gammapy is increased to 10×10 degrees

[20] https://fermi.gsfc.nasa.gov/ssc/data/analysis/software/

masking the edges outside the actual 6×6 degree RoI. Since the FERMIPY analysis is adding an energy bin below and above the energy range to the energy dispersion, also the energy range for the GAMMAPY analysis is extended below 1 GeV to account for lower energy events being reconstructed above 1 GeV. The models of the known sources inside the RoI are fixed to the FERMIPY best-fit values. Including these source models makes the analysis slower but helps to fit the background models properly which in turn also influence the Crab model. During the fit only the Crab's LogParabola model as well as the galactic diffuse background and the isotropic background are left free. The resulting best-fit spectrum and flux points can be seen in figure 36 which are fully consistent with the result from the FERMIPY analysis.

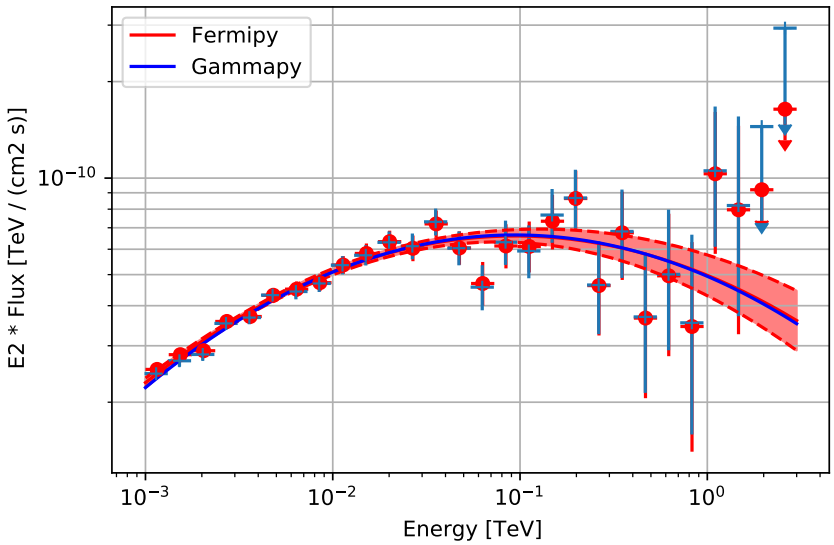

Figure 36: Spectrum and flux points from the FERMIPY analysis (red) compared to the spectrum and flux points of the GAMMAPY analysis.

6.3 Combined analysis

Having cross checked the H.E.S.S. and *Fermi* analysis the next step is to combine the 4 *Fermi* data sets and the 6 H.E.S.S. data sets into a combined fit. Previous analyses have shown that it can be helpful to allow for a relative energy scale between the two instruments. This is also implemented here in the following way. Two different spectral models are assigned to the *Fermi* and H.E.S.S. data sets where all the parameters are linked. The flux of the H.E.S.S. model is calculated at $E_{\mathrm{HESS}} = s \cdot E$ to allow for an energy shift of the model. Using a LogParabola spectral model (eq. 4.3) the best-fit energy scale factor $s = 0.89 \pm 0.01$ is obtained. This means that the H.E.S.S. data best matches the same spectral model than the *Fermi* data when evaluated at 11 % lower energy which is effectively a down shift of the H.E.S.S. flux points in the combined fit. For the Self-Synchrotron-Compton (SSC) model the best-fit energy scale factor $s = 1.024 \pm 0.004$ ($s = 1.086 \pm 0.004$ when including HESS-IU data). This can be explained by the different shapes of the models where the H.E.S.S. flux points seem to be more compatible to the *Fermi* flux points using the SSC model. The best-fit model can be seen in figure 37 where also the contributions due to upscattering of CMB and Synchrotron photons are shown. Only the combination of both is able to describe the data quite well while fitting a relatively small energy scale between the instruments. The resulting electron spectrum can be seen in figure 39 for the case of only HESS-I+II data and for the case of HESS data from all seasons. It is

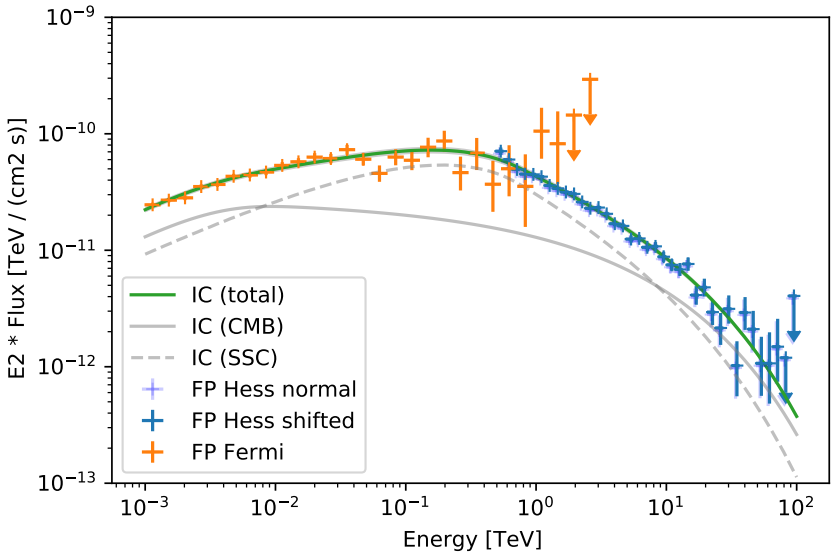

Figure 37: The green line shows the best-fit Inverse Compton model fitted to the *Fermi* and H.E.S.S. (only seasons 1+2) data sets. The solid gray line indicates the contribution due to upscattering of CMB photons where as the dashed gray lines indicates the contribution from Synchrotron photons. The orange flux points are from the single analysis of the *Fermi* data (same as in fig. 36) and the transparent blue flux points are from the single analysis of HESS-I+II data (same as in fig. 35). The solid blue flux points are the transparent blue flux points plotted at $E \cdot 1.024$.

modeled as a *Exponential-Cutoff Broken Power-Law*. The two electron spectra for the two cases look similar but quite different to the spectra from Meyer et al. (2010). This is because the fit does not include data below 1 GeV, so the Synchrotron part of the Crab's spectrum is not considered. However the flux predicted from the synchrotron component of the SSC model needs to match the observed synchrotron flux.

This can be seen in figure 38 where the synchrotron flux prediction of the best-fit electron spectrum is shown for a constant 125 μG B-field at the source. While the IC prediction matches the flux points really well the synchrotron flux does not. This is not really surprising since only data from the IC energy range was fitted. Of course a physical model of the Crab's emission also needs to describe the synchrotron flux properly. This can be achieved by including the synchrotron data in the fit. One possibility is to do a regular χ^2-fit of the model to the flux points. This was done similar to Meyer et al. (2010) with a 10 % systematic uncertainty added to each flux point quadratically. Also the four flux points contributing to the bump just above 10^{12} Hz have been neglected since they are elevated due to the dust in the nebula. And while the B-field in the *Fermi*-H.E.S.S. analysis was fixed to 125 μG because of its high degeneracy with the amplitude it is left free here since the degeneracy is broken by including the synchrotron data. The dashed spectra in figure 38 show the result of this fit. While the synchrotron spectrum matches the data really well, the Inverse Compton part of the spectrum is not fitted that well. The magnetic field for the synchrotron radiation is fitted to 92.8±1.5 μG. One other possibility is to combine the χ^2-fit of the synchrotron component with the likelihood fit of the *Fermi* and H.E.S.S. data. This is implemented by adding the χ^2-value of the synchrotron component and the flux points to the likelihood value of the `Datasets` object calculated in the `stat_sum`

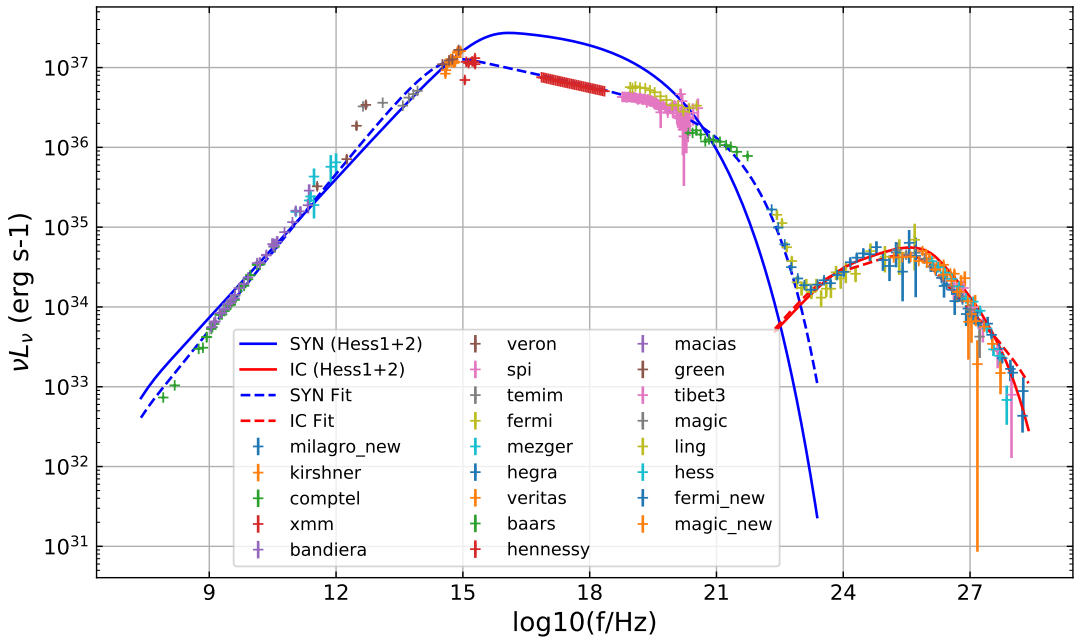

Figure 38: The solid blue and red lines show the synchrotron and IC flux at the source for the best-fit electron spectrum for the HESS-I+II case, respectively. The flux points (provided by Manuel Meyer, for details see figure 1 in [Meyer et al., 2010]) show the broad energy spectrum of the Crab measured by different instruments (see legend). The dashed blue and red lines show the result of a χ^2-fit directly to the flux points (for details see text).

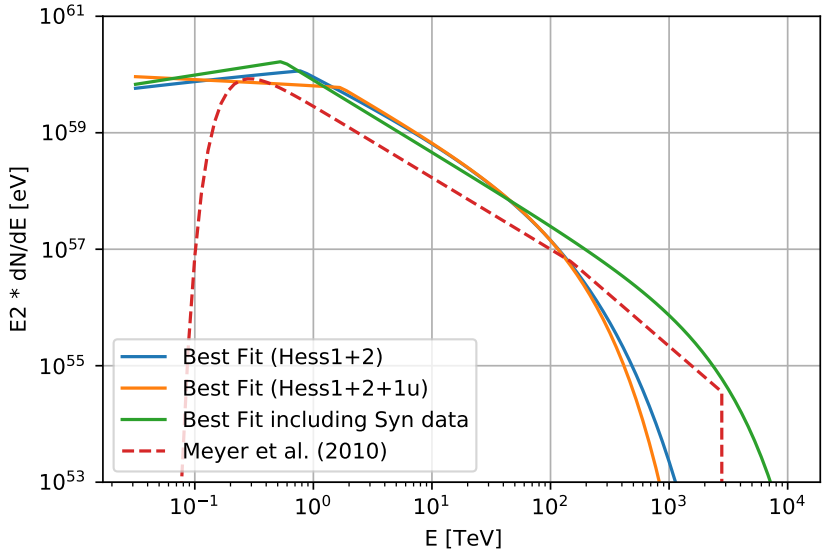

Figure 39: The best-fit electron spectra of the SSC model for the two fits, including HESS-IU data (orange) and only considering pre-HESS-IU data (blue). The electron spectrum of the fit with inclusion of the synchrotron data is shown in green. As comparison the best-fit high energy electron spectrum from Meyer et al. (2010) is also shown.

method in the following way

$$\mathrm{TS}_{\mathrm{tot}} = -2\ln\mathcal{L}_{\mathrm{tot}} = -2\ln\mathcal{L}_{\mathrm{IC}} + \chi^2_{\mathrm{SYN}} \tag{6.1}$$

In this method the χ^2_{SYN} term acts like a prior function which ensures that the synchrotron flux of the SSC model does not deviate significantly from the measured flux points. The result of this method can be seen in figure 40 where the synchrotron flux is nicely matching the observations. The magnetic field is fitted to 90.7±1.2 μG and the energy scale is fitted to 0.888±0.004 which

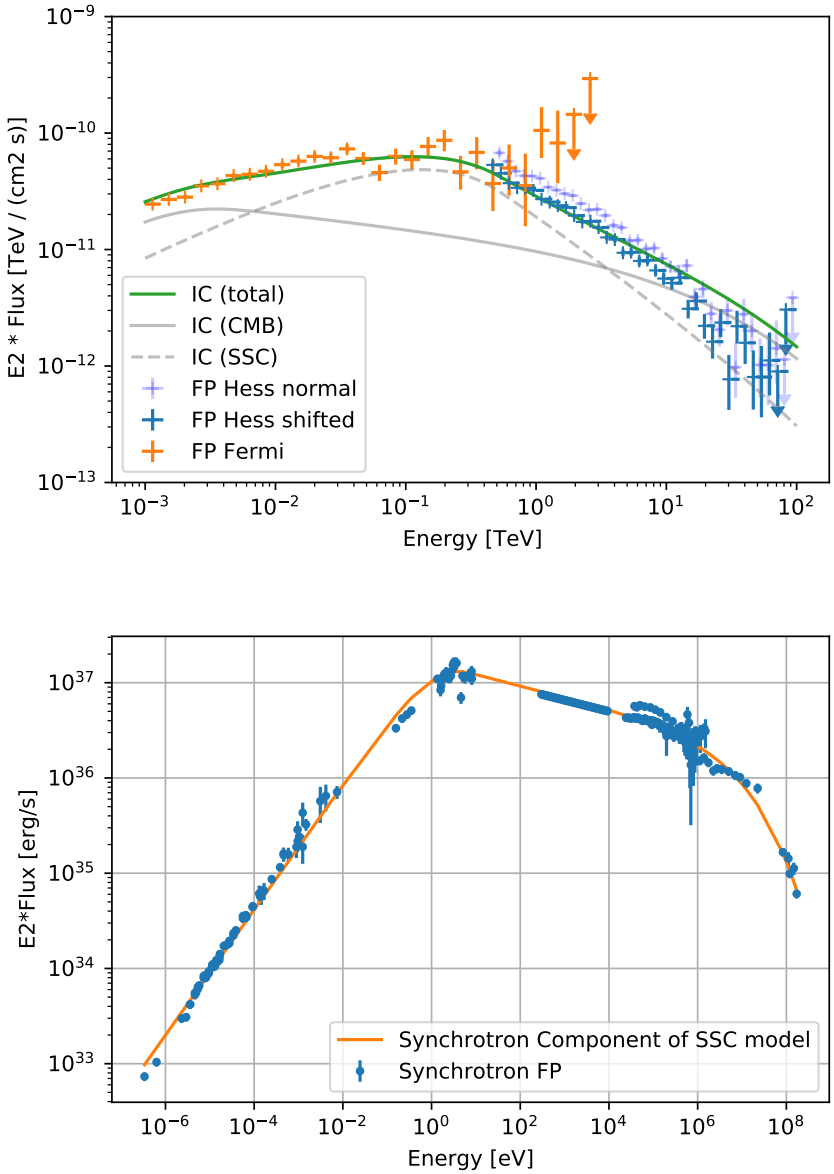

Figure 40: *Top:* SED of the Inverse Compton part of the spectrum when including the synchrotron data. For details see figure 37. *Bottom:* The synchrotron flux of the best-fit SSC model compared with the measured data (same as in figure 38).

is again closer to the best-fit energy scale when using the Log Parabola spectrum. Since the cutoff in the electron spectrum is strongly constrained by the synchrotron data (compare figure 39) the resulting IC spectrum is not able match the high energy HESS flux points anymore. In the future one could use a more sophisticated model similar to Meyer et al. (2010) where the electron distribution is modeled as radial Gaussian matching observations from the synchrotron

regime. The model could also include the dust emission component and allow for more freedom in the electron spectrum.
Moving away from the spectrum towards the morphology, now the sigma of the spatial Gaussian model is fitted in one energy bin per energy decade where additionally the amplitude of the electron spectrum is left free. The synchrotron data is not included here and the spectrum from figure 37 is used. While this 3D approach to determine the extension is also used in Fermipy [Wood et al., 2017], the Crab extension measured by H.E.S.S. was only determined by using a one dimensional θ^2-plot [Holler et al., 2017]. In Gammapy the extension of the Crab can be fitted consistently between the two instruments. The result can be seen in figure 41 compared with the reported extension from Yeung and Horns (2019). While the agreement is reasonable

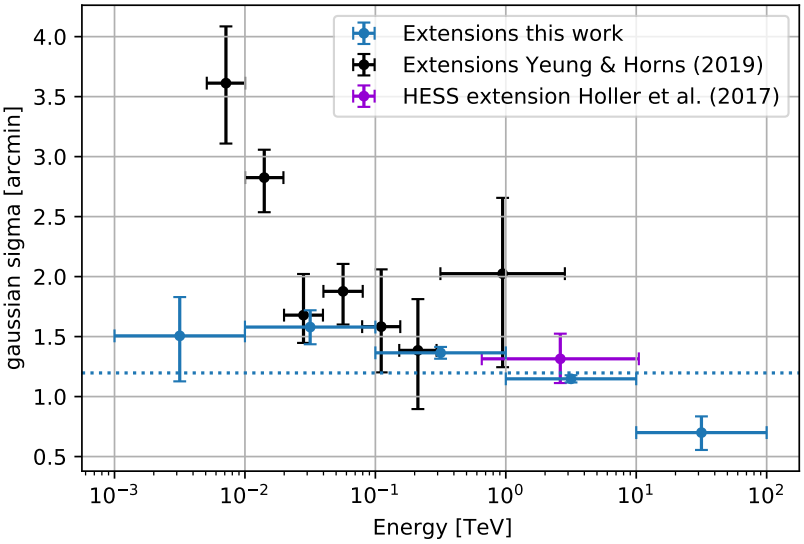

Figure 41: Extension of the Crab fitted in energy bins from this work (blue) and from Yeung and Horns (2019) (black). The errors from this work only include the statistical one which becomes very small once H.E.S.S. data contributes because of the very sharp PSF compared to *Fermi*. Yeung Horns used 9.1 years of *Fermi* LAT data in their analysis and fitted a uniform-disk model and reported its radius multiplied with $\sqrt{0.68}$. The purple point above 2 Tev is the extension measured with H.E.S.S. taken from Holler et al. (2017). The dashed horizontal line indicates the best-fit sigma over the whole energy range.

above 20 GeV there is a big discrepancy below. Even though the spatial models fitted to the data are different (Gaussian in this work, uniform-disk model in Yeung & Horns) and this work uses more *Fermi* data (11.5 yrs compared to 9.1 yrs), this can hardly explain this big difference. The extensions of the cross-check Fermipy analysis agree reasonable well with the Gammapy analysis when choosing only one energy bin per decade. Considering the very small statistical error of the extension once the H.E.S.S. data sets contribute one could think about increasing the binning to get even better resolution. Systematic uncertainties like the pointing uncertainty for H.E.S.S. are not shown in the plot.
In the future observations on the Crab nebula with CTA will give more insights regarding the cutoff in the γ-ray spectrum and the morphology. Based on the good spatial resolution of CTA a lot of open questions might be answered with only a medium amount of observation time [Mestre et al., 2019].

A lot of prizes have been awarded for showing the universe is not as simple as we might have thought.

(Stephen W. Hawking, "A Brief History of Time")

7. Discussion & Conclusion

This work shows that GAMMAPY is generally suited to perform combined 3D analyses combining low-level data of different instruments at the likelihood level. In the first part the IRFs of the KM3NeT/ARCA array were generated from MC simulations and stored in FITS files. Together with the CTA IRFs which already exist in this format a combined analysis of the two instruments was simulated. Such an analysis can be used to distinguish between hadronic and leptonic emission scenarios of astrophysical sources. Based on the calculated sensitivity of KM3NeT the results are reported for the the sources Vela X and RX J1713.7−3946. Many improvements to the analysis have been made from the *initial* results, which could be characterized as "combined analysis", towards the *updated* results where a "combined fit" is employed. While the analysis method of the initial results does not really allow for any physical interpretation, the updated results show that with CTA data alone it will not be possible to effectively differentiate between the emission scenarios. This is at least true for some sources like RX J1713.7−3946 and when neglecting the spatial component of the emission. For other sources like Vela X it is in principle possible to also get significant limits just based on CTA data because the Pion Decay model used in this work is not able to produce a cutoff in the γ-ray spectrum as hard as the one produced by the Inverse Compton model. However the inclusion of KM3NeT data further improves the limits and also further constrains the Pion Decay model for large hadronic contributions.
It could also be shown that the combined optimization of the data gives similar results compared to the combination of the separate optimizations in most of the cases. This is perfectly reasonable when the assumptions of the separate optimizations are consistent with the combined optimization. The main benefit of the combined optimization is that it ensures consistency even when e.g. also fitting spatial components of the source models by linking the physically connected parameters.
Further steps to improve the analysis are to optimize the quality cuts on the neutrino events with the goal of suppressing the background more effectively. Note that the results presented here with 10 years of KM3NeT data can be achieved in approximately 6.2/6.6 years for Vela X/ RX J1713.7−3946 with the published KM3NeT sensitivity. For the analysis itself it is necessary to investigate the influence of the prior function used for the scan on the resulting ΔTS curves. The prior function does not have any physically meaning and is just a tool to ensure that each hadronic contribution can be scanned. First tests showed that varying the prior function can prevent the fit from finding the best minimum in some of the cases. This means that for a set of observations one should perform the scan with multiple prior functions.
In conclusion, this is a promising approach to combine the measurements of γ-ray and neutrino telescopes and to put constraints on the hadronic contribution of the γ-ray flux. In the future this analysis can be performed on further sources with hard spectra extending to very high energies. Some examples could be the galactic center region, HESS J1809−193 / eHWC J1809−193, HESS J1908+063 / eHWC J1907+063 and HESS J1702−420.

In the second part of this thesis the combination of H.E.S.S. and *Fermi* LAT data was used to extend the energy range of the instruments and fit a SSC model to the γ-ray data of the Crab nebula. For the H.E.S.S. flux a discrepancy of 12 % was found for runs of the HESS-IU season compared to pre-HESS-IU runs. Also other analyses [Zorn, 2019] point towards systematics in the HESS-IU data which are not well understood at the moment. This is why the HESS-IU runs are not included for the results presented in this work. In contrast to the first Crab spectrum published by H.E.S.S. [Aharonian, F. et al., 2006] the spectrum obtained in this work agrees better with the spectra measured by other instruments, especially for the higher energies. The GAMMAPY analysis of the *Fermi* data is fully consistent with the FERMIPY analysis. For the combined analysis a relative energy scale factor was introduced between the *Fermi* and H.E.S.S. data accounting for possibly different energy calibrations. The Inverse Compton emission from the best-fit electron spectrum was able to describe the γ-ray data relatively well, while the synchrotron radiation from that electron spectrum did not match the lower energy spectrum measured by other instruments. This means that one also needs to include the synchrotron data in the fit e.g. by adding the χ^2-value of the synchrotron component and the flux points to the likelihood value of the data sets in the fit. This also allows the determination of the present magnetic field. However the cutoff in the electron spectrum is now strongly constrained by the synchrotron data and the high energy flux points of H.E.S.S. are below the prediction of the Inverse Compton model. For the data sets included in this fit the extension of the Crab nebula was determined for each of the five energy decades covered by H.E.S.S. and *Fermi*. This is the first time that the extension of the Crab is measured in a consistent way over such a large energy range. As discovered before there is strong evidence for a shrinking extension with increasing energy where the p-value for a constant extension is just 4.5×10^{-7}. The agreement with previously published extensions is good above 20 GeV, while there is a large discrepancy below 20 GeV where only the *Fermi* data contributes. The reason behind this is currently not understood. The observed energy dependent shrinking of the extension can be explained by the underlying electron distribution. Its radius r_e is also shrinking with energy ($r_e \propto \gamma^{-0.17}$ where γ is the Lorentz factor) when assuming a homogeneous magnetic field [Meyer et al., 2010]. The shrinking extension is then caused by the radiative cooling of the electrons when they expand into the nebula.

In the future one could use a more sophisticated model which would assume a radial Gaussian electron distribution matching observations from the synchrotron regime, also model the dust emission component and allow for more freedom in the electron spectrum. By also including the HESS-IU data in the fit once the discrepancies are eliminated one could improve the statistic for the highest energies but also in the first energy bin where the energy thresholds limit the statistic. Another way to additionally improve the statistic in the energy overlap with *Fermi* would be to include CT5 data once the background model is available.

Appendices

Appendix A H.E.S.S. run lists

For the run selection the following selection cuts have been applied [L. Mohrmann (private communication)]

- Zenith $\leq 55^{\circ}$
- Offset $\leq 1^{\circ}$
- No outliers in tracking and star pointing

For the HESS-I data set this additional cuts are applied

- Run ID $> 20\,000$
- Do not use runs taken during mirror replacement campaign
- Do not use runs that were rejected for the Crab extension measurement (unless they were rejected due to the stricter offset cut)

For the HESS-IU data set the runs 135270, 135271 and 142760 were rejected in addition because they show unstable trigger rates.
This gives the following run lists:

- HESS-I: [23309, 23310, 23523, 23526, 23544, 23545, 23546, 23547, 23556, 23558, 23577, 23579, 23593, 23608, 23641, 23642, 23662, 23663, 23739, 23740, 23741, 23753, 23756, 24139, 43039, 43424, 43447, 43489, 43490, 48399, 48476, 48682, 48683, 54390, 54391, 54653, 54707, 54734, 54748, 54749, 54771, 54772, 54789, 80124, 80129, 80132, 80134, 80158, 80161, 80163, 80165, 80167, 80170, 80190, 80191, 80997, 80998, 81086, 81089, 81133, 81134, 81135, 81136, 81666]

- HESS-II: [88952, 88973, 89354, 89409, 89828, 90203, 90237, 90238, 90277, 90278, 90317, 90318, 90319, 90320, 90321, 90348, 90349, 90350, 90351, 90352, 90376, 90377, 90378, 90379, 90380, 90381, 90382, 90408, 90410, 90414, 90415, 90437, 90439, 90440, 90441, 90478, 90564, 100426, 100452, 100453, 100454, 100573, 100574, 101166, 103053, 103055, 103698, 103804, 103849, 104226]

- HESS-IU: [135126, 135127, 135128, 135129, 135158, 135246, 135247, 135272, 135273, 135290, 135306, 135307, 135333, 135480, 135481, 135629, 135634, 135635, 135665, 135666, 135667, 141861, 141898, 142564, 142565, 142566, 142567, 142568, 142590, 142592, 142593, 142594, 142629, 142630, 142636, 142650, 142651, 142652, 142653, 142654, 142667, 142668, 142669, 142670, 142990, 143050, 143082, 143134, 143136, 143137, 143161, 143164, 143165, 143210, 143211, 144011, 144604, 144605, 145077, 154376, 154377, 154590]

Appendix B Parameters for H.E.S.S. seasons

Table 6: Best-fit model parameters for the LogParabola parameterised according to equation 4.3 with $E_0 = 1\,\mathrm{TeV}$ fitted to the data sets of the different H.E.S.S. seasons. The PSF of each data set has been convoluted with a 30" Gaussian to account for the pointing uncertainty similar to Abdalla et al. (2019).

Season	Φ_0 [10^{-11}·TeV^{-1}·cm^{-2}·s^{-1}]	α	β	sigma [mdeg]
H.E.S.S.-I	3.977 ± 0.043	2.583 ± 0.023	0.064 ± 0.012	18.1 ± 0.6
H.E.S.S.-II	4.148 ± 0.056	2.523 ± 0.030	0.086 ± 0.015	19.3 ± 0.7
H.E.S.S.-Iu	3.447 ± 0.034	2.408 ± 0.019	0.123 ± 0.011	12.0 ± 0.7
H.E.S.S.-I+II	4.070 ± 0.034	2.556 ± 0.018	0.072 ± 0.009	18.6 ± 0.6
All seasons	3.730 ± 0.023	2.446 ± 0.012	0.114 ± 0.007	15.6 ± 0.4

Appendix C Neutrino selection cuts

Here the distributions of the three reconstructed quantities used for the quality cuts are shown in dependence of true energy. For the distributions no pre-cuts have been applied so all of the events for which the reconstruction algorithm converged enter the histograms.

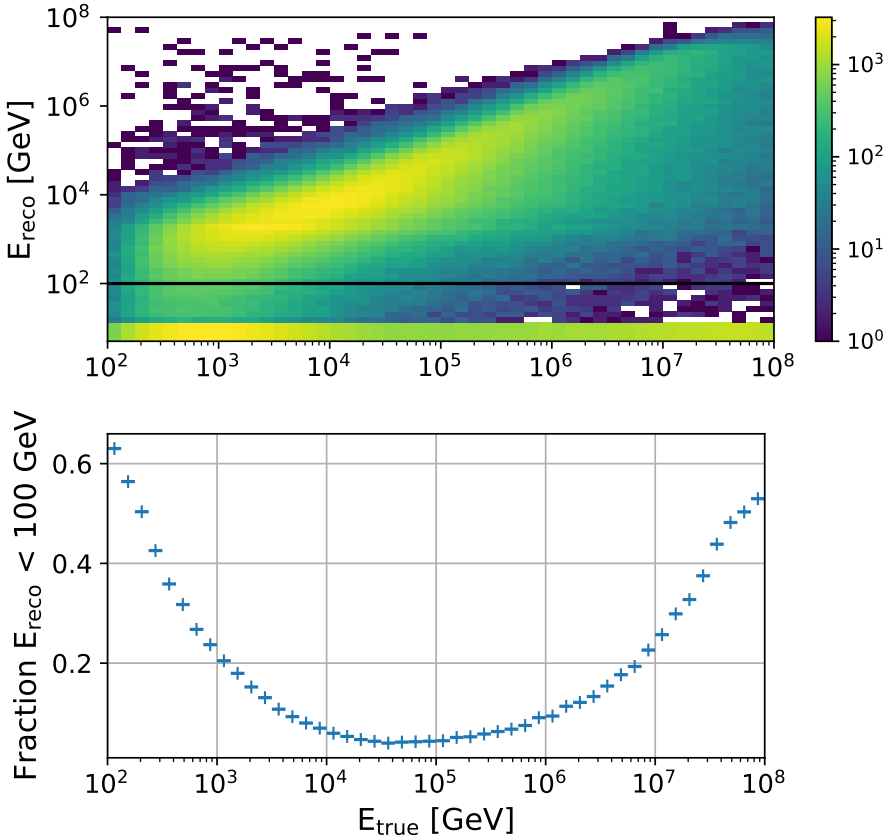

Figure 42: Top panel: 2D histogram of the reconstructed energy of the Monte Carlo events versus their true energy. The black line at 100 GeV is marking the reconstructed energy cut. The lowest E_{reco} bin contains many events where the reconstruction failed and the reconstructed energy is zero. Bottom panel: For each bin of true energy the number of events with a reconstructed energy below 100 GeV divided by the total number of events in that bin.

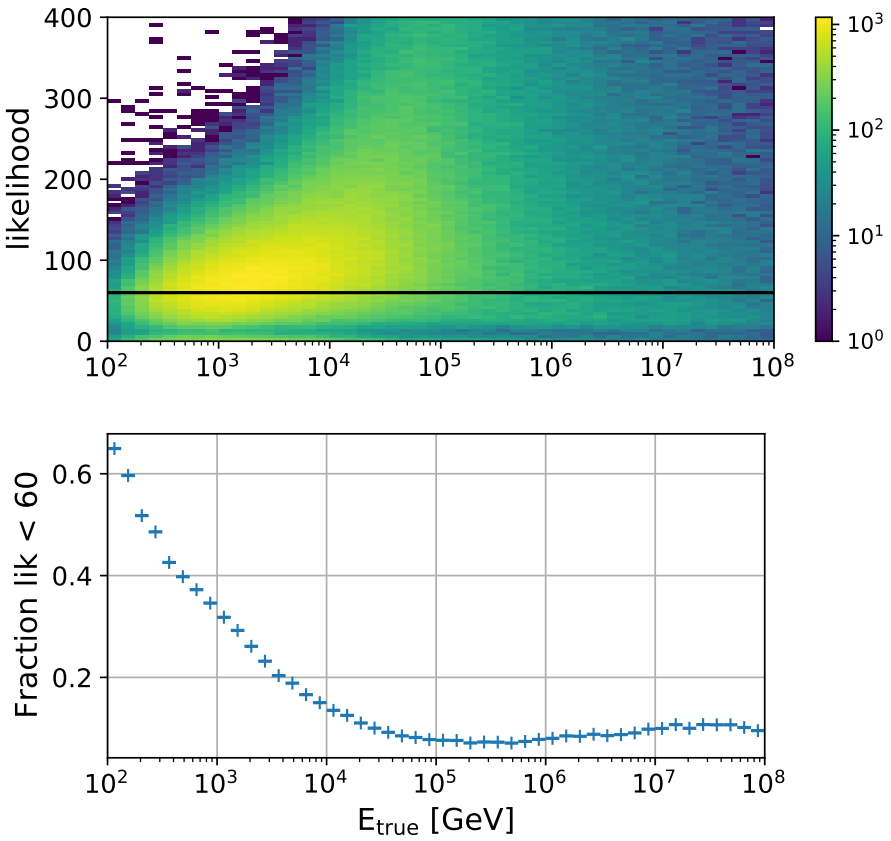

Figure 43: Top panel: 2D histogram of the reconstruction likelihood versus the true Monte–Carlo energy. The black line at $lik = 60$ indicates the likelihood cut. Bottom panel: Shows the fraction of events that do not pass that cut.

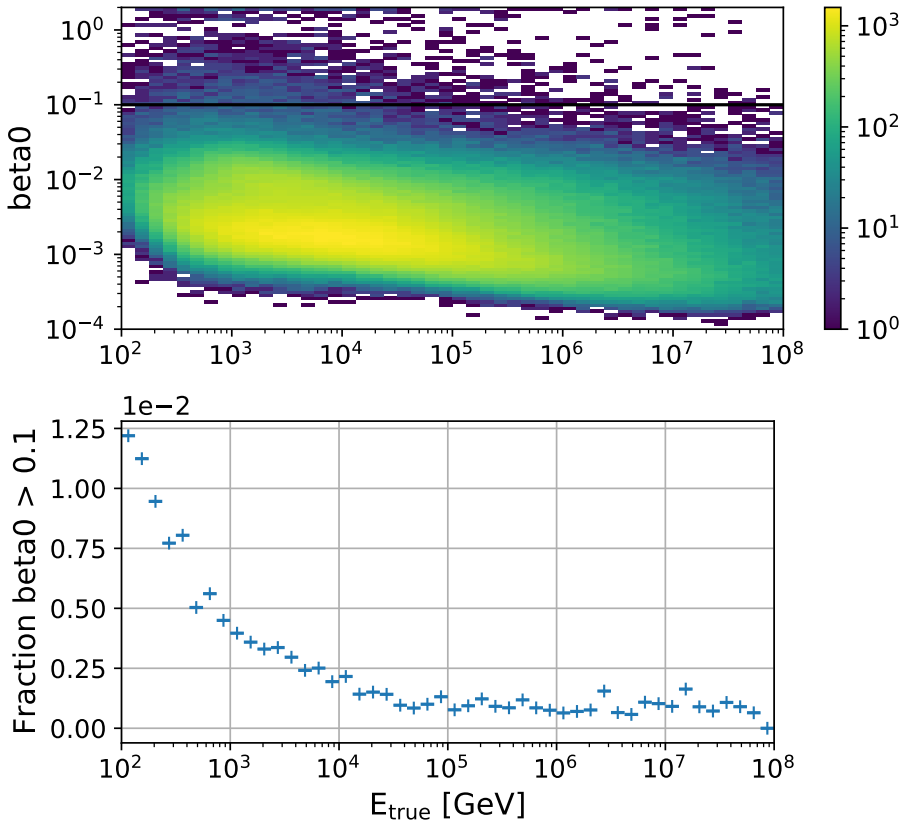

Figure 44: Top panel: Top panel: 2D histogram of Beta0 (curvature of the likelihood) versus the true Monte-Carlo energy. The black line at $Beta0 = 0.1$ indicates the cut. Bottom panel: Shows the fraction of events that do not pass that cut.

References

H. Abdalla, A. Abramowski, F. Aharonian, et al. H.E.S.S. observations of RX J1713.7−3946 with improved angular and spectral resolution: Evidence for gamma-ray emission extending beyond the X-ray emitting shell. *Astronomy & Astrophysics*, 612:A6, 2018. doi: 10.1051/0004-6361/201629790.

H. Abdalla et al. Resolving the Crab pulsar wind nebula at teraelectronvolt energies. *Nature Astron.*, 4(2):167–173, 2019. doi: 10.1038/s41550-019-0910-0. URL https://hal.archives-ouvertes.fr/hal-02483963.

S. Abdollahi, F. Acero, M. Ackermann, M. Ajello, W. B. Atwood, M. Axelsson, L. Baldini, J. Ballet, G. Barbiellini, D. Bastieri, and et al. Fermi Large Area Telescope Fourth Source Catalog. *The Astrophysical Journal Supplement Series*, 247(1):33, Mar 2020. doi: 10.3847/1538-4365/ab6bcb. URL http://dx.doi.org/10.3847/1538-4365/ab6bcb.

A. U. Abeysekara et al. Measurement of the Crab Nebula Spectrum Past 100 TeV with HAWC. *The Astrophysical Journal*, 881(2):134, aug 2019. doi: 10.3847/1538-4357/ab2f7d. URL https://doi.org/10.3847%2F1538-4357%2Fab2f7d.

A. Abramowski, F. Acero, F. Aharonian, et al. Probing the extent of the non-thermal emission from the Vela X region at TeV energies with H.E.S.S.. *Astronomy & Astrophysics*, 548:A38, 2012. doi: 10.1051/0004-6361/201219919.

S Adrián-Martínez, M Ageron, F Aharonian, S Aiello, A Albert, F Ameli, E Anassontzis, M Andre, G Androulakis, M Anghinolfi, and et al. Letter of intent for KM3NeT 2.0. *Journal of Physics G: Nuclear and Particle Physics*, 43(8):084001, Jun 2016. doi: 10.1088/0954-3899/43/8/084001. URL http://dx.doi.org/10.1088/0954-3899/43/8/084001.

F. Aharonian, A. Akhperjanian, M. Beilicke, K. Bernlohr, H.-G. Borst, H. Bojahr, O. Bolz, T. Coarasa, J. L. Contreras, J. Cortina, and et al. The Crab Nebula and Pulsar between 500 GeV and 80 TeV: Observations with the HEGRA Stereoscopic Air Cerenkov Telescopes. *The Astrophysical Journal*, 614(2):897–913, Oct 2004. doi: 10.1086/423931. URL http://dx.doi.org/10.1086/423931.

F. A. Aharonian, S. R. Kelner, and A. Yu. Prosekin. Angular, spectral, and time distributions of highest energy protons and associated secondary gamma rays and neutrinos propagating through extragalactic magnetic and radiation fields. *Physical Review D*, 82(4):043002, August 2010. doi: 10.1103/PhysRevD.82.043002.

Aharonian, F. et al. Observations of the Crab nebula with HESS. *A&A*, 457(3):899–915, 2006. doi: 10.1051/0004-6361:20065351. URL https://doi.org/10.1051/0004-6361:20065351.

S. Aiello et al. Sensitivity of the KM3NeT/ARCA neutrino telescope to point-like neutrino sources. *Astroparticle Physics*, 111:100 – 110, 2019. doi: https://doi.org/10.1016/j.astropartphys.2019.04.002. URL http://www.sciencedirect.com/science/article/pii/S0927650518302809.

M. Amenomori et al. First Detection of Photons with Energy beyond 100 TeV from an Astrophysical Source. *Phys. Rev. Lett.*, 123:051101, Jul 2019. doi: 10.1103/PhysRevLett.123.051101. URL https://link.aps.org/doi/10.1103/PhysRevLett.123.051101.

W. B. Atwood, A. A. Abdo, M. Ackermann, W. Althouse, B. Anderson, M. Axelsson, L. Baldini, J. Ballet, D. L. Band, G. Barbiellini, and et al. THE LARGE AREA TELESCOPE ON THEFERMI GAMMA-RAY SPACE TELESCOPEMISSION. *The Astrophysical Journal*, 697 (2):1071–1102, May 2009. doi: 10.1088/0004-637x/697/2/1071. URL http://dx.doi.org/10.1088/0004-637X/697/2/1071.

Julia K. Becker. High-energy neutrinos in the context of multimessenger astrophysics. *Physics Reports*, 458(4-5):173–246, Mar 2008. doi: 10.1016/j.physrep.2007.10.006. URL http://dx.doi.org/10.1016/j.physrep.2007.10.006.

Berge, D., Funk, S., and Hinton, J. Background modelling in very-high-energy γ-ray astronomy. *A&A*, 466(3):1219–1229, 2007. doi: 10.1051/0004-6361:20066674. URL https://doi.org/10.1051/0004-6361:20066674.

M Bustamante, G Carrillo Montoya, W de Paula, J A Duarte Chavez, A M Gago, H Hakobyan, P Jez, J A Monroy Montañez, A Ortiz Velasquez, F Padilla Cabal, M Pino Rozas, D J Rodriguez Patarroyo, G L Romeo, U J Saldaña-Salazar, M Velasquez, and M von Steinkirch. High-energy cosmic-ray acceleration. 2010. doi: 10.5170/CERN-2010-001.533. URL https://cds.cern.ch/record/1249755.

Glen Cowan, Kyle Cranmer, Eilam Gross, and Ofer Vitells. Asymptotic formulae for likelihood-based tests of new physics. *Eur. Phys. J. C*, 71:1554, 2011.

A. Einstein. Die Grundlage der allgemeinen Relativitätstheorie. *Annalen der Physik*, 354(7): 769–822, 1916. doi: 10.1002/andp.19163540702. URL https://onlinelibrary.wiley.com/doi/abs/10.1002/andp.19163540702.

Rikard Enberg, Mary Hall Reno, and Ina Sarcevic. Prompt neutrino fluxes from atmospheric charm. *Physical Review D*, 78(4), Aug 2008. doi: 10.1103/physrevd.78.043005. URL http://dx.doi.org/10.1103/PhysRevD.78.043005.

Carmelo Evoli. The Cosmic-Ray Energy Spectrum, October 2018. URL https://doi.org/10.5281/zenodo.2360277.

Stefan Funk. Ground- and Space-Based Gamma-Ray Astronomy. *Annual Review of Nuclear and Particle Science*, 65(1):245–277, Oct 2015. doi: 10.1146/annurev-nucl-102014-022036. URL http://dx.doi.org/10.1146/annurev-nucl-102014-022036.

Victor F. Hess. Über Beobachtungen der durchdringenden Strahlung bei sieben Freiballonfahrten. *Phys. Z.*, 13:1084–1091, 1912.

A. M. Hillas. Cerenkov Light Images of EAS Produced by Primary Gamma Rays and by Nuclei. In *19th International Cosmic Ray Conference (ICRC19), Volume 3*, volume 3 of *International Cosmic Ray Conference*, page 445, August 1985.

M. Holler, D. Berge, J. Hahn, D. Khangulyan, R. D. Parsons, and H. E. S. S. Collaboration. Advanced search for the extension of unresolved TeV sources with H.E.S.S. In *35th International Cosmic Ray Conference (ICRC2017)*, volume 301 of *International Cosmic Ray Conference*, page 676, January 2017.

M. Honda, T. Kajita, K. Kasahara, S. Midorikawa, and T. Sanuki. Calculation of atmospheric neutrino flux using the interaction model calibrated with atmospheric muon data. *Physical Review D*, 75(4), Feb 2007. doi: 10.1103/physrevd.75.043006. URL http://dx.doi.org/10.1103/PhysRevD.75.043006.

Ervin Kafexhiu, Felix Aharonian, Andrew M. Taylor, and Gabriela S. Vila. Parametrization of gamma-ray production cross sections for p p interactions in a broad proton energy range from the kinematic threshold to PeV energies. *Physical Review D*, 90(12):123014, December 2014. doi: 10.1103/PhysRevD.90.123014.

S. R. Kelner, F. A. Aharonian, and V. V. Bugayov. Energy spectra of gamma rays, electrons, and neutrinos produced at proton-proton interactions in the very high energy regime. *Physical Review D*, 74:034018, 2006.

D. Khangulyan, F. A. Aharonian, and S. R. Kelner. Simple Analytical Approximations for Treatment of Inverse Compton Scattering of Relativistic Electrons in the Blackbody Radiation Field. *The Astrophysical Journal*, 783(2):100, March 2014. doi: 10.1088/0004-637X/783/2/100.

Claudio Kopper. *Performance Studies for the KM3NeT Neutrino Telescope*. PhD thesis, Friedrich-Alexander-Universität Erlangen-Nürnberg, 2010.

MAGIC Collaboration, Acciari, V. A., et al. MAGIC very large zenith angle observations of the Crab Nebula up to 100 TeV. *A&A*, 635:A158, 2020. doi: 10.1051/0004-6361/201936899. URL https://doi.org/10.1051/0004-6361/201936899.

K. Meagher, VERITAS Collaboration, et al. Six years of VERITAS observations of the Crab Nebula. In *34th International Cosmic Ray Conference (ICRC2015)*, volume 34 of *International Cosmic Ray Conference*, page 792, July 2015.

E Mestre et al. Prospects for the characterization of the VHE emission from the Crab nebula and pulsar with the Cherenkov Telescope Array. *Monthly Notices of the Royal Astronomical Society*, 492(1):708–718, 12 2019. doi: 10.1093/mnras/stz3421. URL https://doi.org/10.1093/mnras/stz3421.

M. Meyer, D. Horns, and H. S. Zechlin. The Crab Nebula as a standard candle in very high-energy astrophysics. *Astronomy & Astrophysics*, 523:A2, November 2010. doi: 10.1051/0004-6361/201014108.

L. Mohrmann, A. Specovius, D. Tiziani, S. Funk, D. Malyshev, K. Nakashima, and C. van Eldik. Validation of open-source science tools and background model construction in γ-ray astronomy. *Astronomy Astrophysics*, 632:A72, Dec 2019. doi: 10.1051/0004-6361/201936452. URL http://dx.doi.org/10.1051/0004-6361/201936452.

Lars Mohrmann. *Characterizing cosmic neutrino sources*. PhD thesis, Humboldt-Universität zu Berlin, Mathematisch-Naturwissenschaftliche Fakultät, 2015.

Kohta Murase and Eli Waxman. Constraining high-energy cosmic neutrino sources: Implications and prospects. *Physical Review D*, 94(10), Nov 2016. doi: 10.1103/physrevd.94.103006. URL http://dx.doi.org/10.1103/PhysRevD.94.103006.

R.D. Parsons and J.A. Hinton. A Monte Carlo template based analysis for air-Cherenkov arrays. *Astroparticle Physics*, 56:26–34, Apr 2014. doi: 10.1016/j.astropartphys.2014.03.002. URL http://dx.doi.org/10.1016/j.astropartphys.2014.03.002.

Cecilia Helena Payne. *Stellar Atmospheres; a Contribution to the Observational Study of High Temperature in the Reversing Layers of Stars*. PhD thesis, RADCLIFFE COLLEGE., January 1925.

M. Tanabashi et al. Review of Particle Physics. *Phys. Rev. D*, 98:030001, Aug 2018. doi: 10.1103/PhysRevD.98.030001. URL https://link.aps.org/doi/10.1103/PhysRevD.98.030001.

S. S. Wilks. The Large-Sample Distribution of the Likelihood Ratio for Testing Composite Hypotheses. *The Annals of Mathematical Statistics*, 9(1):60–62, 1938. URL http://www.jstor.org/stable/2957648.

D. Williams. Results from IceCube. In *36th International Cosmic Ray Conference (ICRC2019)*, volume 36 of *International Cosmic Ray Conference*, page 16, July 2019.

M. Wood, R. Caputo, E. Charles, M. Di Mauro, J. Magill, J. S. Perkins, and Fermi-LAT Collaboration. Fermipy: An open-source Python package for analysis of Fermi-LAT Data. In *35th International Cosmic Ray Conference (ICRC2017)*, volume 301 of *International Cosmic Ray Conference*, page 824, January 2017.

Paul K. H. Yeung and Dieter Horns. The Energy-dependent γ-Ray Morphology of the Crab Nebula Observed with the Fermi Large Area Telescope. *The Astrophysical Journal*, 875(2):123, April 2019. doi: 10.3847/1538-4357/ab107a.

Qiang Yuan, Peng-Fei Yin, Xue-Feng Wu, Xiao-Jun Bi, Siming Liu, and Bing Zhang. A STATISTICAL MODEL FOR THE -RAY VARIABILITY OF THE CRAB NEBULA. *The Astrophysical Journal*, 730(2):L15, Mar 2011. doi: 10.1088/2041-8205/730/2/l15. URL http://dx.doi.org/10.1088/2041-8205/730/2/L15.

Justus Zorn. *Cherenkov Camera and Analysis Development for Highest-Energy Gamma-Ray Astronomy*. PhD thesis, Ruperto-Carola-University of Heidelberg, Combined Faculties of the Natural Sciences and Mathematics, 2019.

You must also have a sense of when to stop.

(Garry Kasparov, "How Life Imitates Chess")

Acknowledgements

Last but not least I would like to thank everyone who supported me during this thesis and the difficult COVID-19 times. A special thanks goes to:

- Prof. Dr. Stefan Funk for giving me the opportunity to work on this very interesting project and always finding the time for helpful discussions,
- Lars Mohrmann for his patience when helping me with technical issues, for his always important advice and for reviewing this thesis,
- Tamás Gál, Jannik Hofestädt and Kay Graf for helping me with the generation of the KM3NeT IRFs and for always being open for questions,
- Manuel Meyer for working on the Fermipy analysis and for sharing his vast knowledge on the Crab nebula
- my family for always being there and supporting me with everything I could ask for.

Without you this would not have been possible. Thank you all again!

Erklärung / Statement of Authorship

Hiermit bestätige ich, dass ich diese Arbeit selbstständig und nur unter Verwendung der angegebenen Hilfsmittel angefertigt habe.

I hereby certify that this thesis has been composed by me and is based on my own work, unless stated otherwise.

Erlangen, 03. December 2020

Tim Unbehaun